From the holdings of the Department of Special Collections , Princeton University Library, Princeton, NJ

These documents are either in the public domain, or can only be used for educational and research purposes (Fair use) as per U.S. Copyright law (text below). By accessing this file, all users agree that their use falls in the public domain or within fair use as defined by the copyrightlaw. We do not charge any permission or usage fees for the publication of images of material inour collections, including those provided by Princeton University Library, via our website, catalog, or directly from staff.For more information regarding copyright, credit, and citation please review the information onthe Copyright, Credit and Citation Guidelines page of our website.
https://library.princeton.edu/special-collections/policies/copyright-credit-and-citation-guidelines. If you have any questions, including how to order higher-quality images from the collection, contact Special Collections Public Services via our Ask Us! Form. https://library.princeton.edu/special-collections/ask-us

---

Doctoral Dissertations, 2011-2026 Astrophysical Sciences

2017

Simulating chemistry in star forming environments

Gong, Munan

Princeton, NJ : Princeton University

---

http://arks.princeton.edu/ark:/88435/dsp017s75dg02n

U.S. Copyright law: The copyright law of the United States (Title 17, §108, United States Code) governs the making of photocopies or other reproductions of copyrighted material. Under certain conditions specified in the law, libraries and archives are authorized to furnish a photocopy or other reproduction. One of these specified conditions is that the photocopy or reproduction is not to be used for any purpose other than private study, scholarship, or research. If a user makes a request for, or later uses, a photocopy or reproduction for purposes in excess of fair use that user may be liable for copyright infringement. This institution reserves the right to refuse to accept a copying order if, in its judgment, fulfillment of the order would involve a violation of copyright law. https://www.copyright.gov/title17/title17.pdf

Simulating chemistry in star forming environments

Munan Gong

A Dissertation
Presented to the Faculty
of Princeton University
in Candidacy for the Degree
of Doctor of Philosophy

Recommended for Acceptance
by the Department of
Astrophysical Sciences
Adviser: Professor Eve C. Ostriker

September 2017

© Copyright by Munan Gong, 2017.

All rights reserved.

Abstract

Chemistry plays an important role in the interstellar medium (ISM), regulating the heating and cooling of the gas and determining abundances of molecular species that trace gas properties in observations. One of the most abundant and important molecules in the ISM is CO. CO is a main coolant for the molecular ISM, and the CO($J = 1 - 0$) line emission is a widely used observational tracer for molecular clouds.

In Chapter 2, we propose a new simplified chemical network for hydrogen and carbon chemistry in the atomic and molecular ISM. We compare results from our chemical network in detail with results from a full photodissociation region (PDR) code, and also with the Nelson & Langer (1999) (NL99) network previously adopted in the simulation literature. We show that our chemical network gives similar results to the PDR code in the equilibrium abundances of all species over a wide range of densities, temperature, and metallicities, whereas the NL99 network shows significant disagreement. We also compare with observations of diffuse and translucent clouds. We find that the CO, CH_x and OH_x abundances are consistent with equilibrium predictions for densities $n = 100 - 1000$ cm^{-3}, but the predicted equilibrium C abundance is higher than observations, signaling the potential importance of non-equilibrium/dynamical effects.

In Chapter 3, we apply our new chemistry network to a study of the $X_{\rm CO}$ conversion factor, which is used to convert the CO luminosity to the total H_2 mass. We use numerical simulations to investigate how $X_{\rm CO}$ depends on numerical resolution, non-equilibrium chemistry, physical environment, and observational beam size. Our study employs 3D magnetohydrodynamics (MHD) simulations of galactic disks with solar neighborhood conditions, where star formation and the three-phase interstellar medium (ISM) is self-consistently generated by the interaction between gravity and stellar feedback. Synthetic CO maps are obtained by post-processing the MHD simulations with chemistry and radiation transfer. We find that CO is only an approximate tracer of H_2. Nevertheless, $\langle X_{\rm CO}\rangle = 0.7 - 1.0 \times 10^{20}$ cm^{-2}K^{-1}km^{-1}s consistent with observations, insensitive to the evolutionary ISM state or the far-ultraviolet

(FUV) radiation field strength. Our numerical simulations successfully reproduce the observed variations of $X_{\rm CO}$ on parsec scales, as well as the dependence of $X_{\rm CO}$ on extinction and the CO excitation temperature.

Acknowledgements

First, I would like to thank my advisor, Eve Ostriker. She has provided constant guidance, support and inspiration through my journey in graduate school, from writing my first paper, to this thesis. She not only guided me through the process of learning to do research, but also helped me to develop my scientific career by encouraging me to attend scientific conferences and build collaborations. She taught me how to pick good research topics, how to clearly and effectively communicate in writing scientific papers and giving presentations, and the value to be thorough and careful in all details of research. I will always remember the encouragement and support she has given me during the difficult times of visa issues, job applications, two-body problems, and much more.

I would also like to thank my thesis committee. Jim Stone encouraged me to pursue this thesis back when I started, and gave many suggestions and help in developing the chemistry module in Athena++. His group meetings have been a wonderful source of new ideas and communications. Bruce Draine answered many detailed questions about chemistry, and his class introduced me to the beautiful world of the ISM. Jenny Green is the observer in this committee who keeps everything sensible and relevant to the real world. She has also been a very caring and helpful director of graduate studies. Mark Wolfire taught me a lot of astrochemistry and made crucial contributions to the chemistry paper. I am very grateful that he agreed to travel all the way from Maryland to attend my final public oral exam.

Many others in the scientific community also gave helpful advice and suggestions to this thesis. I would like to especially thank Simon Glover. As he works on similar subjects, he could have been a fierce competitor, but instead, he offered many kind and useful suggestions to me both on my science and postdoc applications. Many thanks to Edward Jenkins for his discussions in observations of the ISM, Kengo Tomida and Christopher White for their help in developing Athena++, Mark Heyer for providing the observational data of Orion molecular clouds, Adam Leroy for making the preprint of Lee et al. (in prep) available and helpful discussions of comparisons with observations. This work is also part of the TCAN

project, and I learned a lot from communicating with other TCAN members: Chalence Safranek-Shrader, Aaron Skinner, Christopher McKee, Mark Krumholz and Richard Klein. I would like to especially thank Chang-Goo Kim, who is also a TCAN member as well as a postdoc in Peyton. He has been my go-to person for technical questions.

A big thank you to those who guided me into the world of astronomy, my undergraduate advisors Douglas (Doug) Lin, Pascale Garaud, Greg Herczeg, and the advisor for my first semester project in Princeton, Gaspar Bakos. I want to especially thank Doug Lin, my first scientific advisor ever, who inspired me to venture into the world of scientific research, and invited me to all of his Christmas parties as part of the family.

A special thanks to Kedron Silsbee, who made this journey not just a meaningful one, but also an enjoyable one. He helped me to settle down in the challenging life of graduate school. He is the shoulder that I can find in all good and bad days, and he has contagious enthusiasm towards science and outdoors. He also offered everyday help in my English writing and speaking, including in the writing of this thesis.

Many graduate students and postdocs in Peyton have offered their help when I have a question about science or life, or even when I just need a friend to talk to or a ride home. I feel very fortunate to be in this Peyton family. Some of them as already been mentioned above, but there are many more: Xu (Chelsea) Huang, Simone Ferraro, Emmanuel Schaan, Wenhua (Wendy) Ju, Ailei Sun, Petchara (Pete) Pattarakijwanich, Brandon Hensley, Timothy Brandt, Xuening Bai, Robin Dong, Yanfei Jiang, Zhaohuan Zhu, Jiming Shi...

Outside of academia, I have met many friends in Princeton through the Mountaineering Club and the Chinese Student Association. They have made Princeton home for me in the past five years, and thank you, Kevin Miller, Ping Lu, Andras Gyenis, Gabriel Man, Jack Hare, Dainan Mao, Aishan Zhao, Mu Shang, Elisabeth Krause, Leenoy Meshulam, Alan Marmelstein, Mallika Randeria, Ryan Ly, Stephanie Chan, Alex Washburne, Jonathan (Jono) Squire, Bert Harris, Seth Davidovits, Hannah Waight, Corwin Shiu, Justin Proffitt, KatieAnna Wolf, Katja Luxem, Mircea Davidescu, Peter Schauss, Lauren Peritz, John Wil-

son, and many more. I would also like to thank Robert Lupton, who provided guidance for many of my life and academia problems. I drew much courage from conversations with him when driving up to the Gunks.

Last but not least, I want to thank my parents, who made everything possible. They have been very supportive for me to pursue my PhD., although this means that I will be far away from home and seldom see them. I am very thankful that they are traveling across the Earth to attend my thesis defense. I dedicate this thesis to them.

To my parents.

Relation to Published Work

Chapter 2 in this thesis is based on work done in collaboration with Eve Ostriker and Mark Wolfire, and published as Gong, Ostriker, & Wolfire, *A Simple and Accurate Network for Hydrogen and Carbon Chemistry in the Interstellar Medium* in the Astrophysical Journal, Volume 843, Issue 1, article id. 38, 35 pp. (2017). Part of this work has been presented in the Star Formation 2016 Conference in Exeter, England (08/2016), and the Conference of Molecules and Dust as Fuel to Star Formation, at the Kavli Institute for Theoretical Physics, Santa Barbara, California (06/2016).

Chapter 3 is based on work done in collaboration with Eve Ostriker and Chang-Goo Kim, and it is forthcoming as a separate paper.

Contents

Abstract iii

Acknowledgements v

Relation to Published Work ix

List of Tables xiii

List of Figures xiv

1 Introduction **1**

1.1 Chemistry in the Star Forming Interstellar Medium 1

1.2 The $X_{\rm CO}$ Conversion Factor 4

2 A simple and accurate network for hydrogen and carbon chemistry in the interstellar medium **7**

2.1 The Chemical Model 7

2.1.1 Chemical Reaction Network 7

2.1.2 Heating and Cooling Processes 11

2.1.3 Numerical Method 13

2.2 Code Test and Comparison 14

2.3 Sample applications 21

2.3.1 CO as a Tracer of H_2 and Cold Gas 23

2.3.2 Dependence on χ, $\xi_{\rm H}$, and Z 27

2.3.3 Are Molecules Necessary for Low Temperatures? 30

2.3.4 Molecular Gas and Star Formation? 32
2.3.5 Comparison with Observations of Diffuse and Translucent Clouds . . 33
2.4 Summary 39

3 The $X_{\rm CO}$ conversion factor from galactic disk ISM simulations 41
3.1 Method 41
3.1.1 MHD Simulation 41
3.1.2 Post-processing chemistry 44
3.1.3 Synthetic Observation of CO Line Emission 46
3.1.4 The beam size in synthetic observations 48
3.1.5 Model parameters 50
3.2 Results 51
3.2.1 Convergence study: effects of numerical resolution 51
3.2.2 Non-equilibrium Chemistry 69
3.2.3 Variations in Galactic Environments 72
3.2.4 Dependence of $X_{\rm CO}$ on the Observational Beam Size 79
3.3 Summary 81

4 Conclusions 83

A Description of the Chemical Network 85
A.1 Extension of the NL99 Network 85
A.2 CH_x Pseudo-reactions 89
A.3 OH_x Pseudo-reactions 90

B Heating and Cooling Processes 100
B.1 Heating 100
B.1.1 Cosmic-Ray Ionization 100
B.1.2 Photoelectric Effect on Dust Grains 101

B.1.3 H_2 Formation on Dust Grains, and UV Pumping of H_2 101
B.1.4 H_2 Photodissociation 102
B.2 Cooling 102
B.2.1 Atomic lines: C^+, C, and O Fine Structure lines, and the Lyα line . . 102
B.2.2 CO Rotational Lines 102
B.2.3 H_2 Rotational and Vibrational Lines 104
B.2.4 Dust Thermal Emission 105
B.2.5 Recombination of e on PAHs 106
B.2.6 Collisional Dissociation of H_2 and Collisional Ionization of H 106

C Additional Plots and Discussions for Code Test and Comparison 109
C.1 Chemistry with Constant Temperature 109
C.2 Chemistry and Temperature 109
C.3 Comparison at Low Metallicity 114
C.4 Grain-assisted Recombination Rates 115
C.5 Grain Surface Reactions 119
C.6 Comparison with the *PyPDR* code 121

D Characteristic Density in Slab and Spherical Turbulent Clouds 124

E Additional Plots for Comparison with Observations of Diffuse and Translucent Clouds 127

List of Tables

3.1 Observational parameters in selected $X_{\rm CO}$ literature 49

3.2 Parameters for synthetic observations 50

3.3 Model parameters 51

3.4 Overall properties of models for comparisons in numerical resolution and non-equilibrium chemistry 54

3.5 Overall properties of models: variations in galactic environment 75

A.1 List of Collisional Chemical Reactions 93

A.2 List of Grain-assisted Reactions, Cosmic-ray Reactions, and Photodissociation Reactions 97

B.1 List of Heating and Cooling Processes 107

List of Figures

2.1 Contours showing locations of H to H_2, C^+ to C, and C to CO transitions in the N–n plane. The magenta, yellow, and black lines are contours where $x_{CO}/x_{C_{tot}}$, $x_{C^+}/x_{C_{tot}}$, and $2x_{H_2}$ are respectively equal to 0.5. The solid, dashed and dotted lines are the results of the chemistry network in this work, the PDR code, and the NL99 network, respectively. The black dashed-dotted line plots the analytic formula in Bialy & Sternberg (2016) for the H to H_2 transition. The left panel (a) is using cosmic-ray ionization rate $\xi_H = 2 \times 10^{-16} s^{-1} H^{-1}$ (Indriolo et al., 2007), and the right panel (b) is using the old low cosmic-ray ionization rate $\xi_H = 10^{-17} s^{-1} H^{-1}$. The gas temperature is fixed at $T = 20K$. The regions where the H_2 formation timescale is comparable to or shorter than the typical turbulence crossing timescale are shaded dark gray for $t_{H_2}/t_{dyn} < 1$ and light gray for $t_{H_2}/t_{dyn} < 10$ (see Equation (2.17)). 17

2.2 Abundances of different species as a function of A_V and N at densities $n = 100\text{cm}^{-3}$ in panel (a) and $n = 1000\text{cm}^{-3}$ in panel (b). The cosmic-ray ionization rate here is $\xi_{\text{H}} = 2 \times 10^{-16}\text{s}^{-1}\text{H}^{-1}$, corresponding to panel (a) of Figure 2.1. Gas temperature is fixed at $T = 20$ K. See also Figures C.1 and C.3 in Appendix C for abundances of all species at densities between $n = 50-1000\text{cm}^{-3}$. The abundances of different species $x_i = n_i/n$ are plotted in different colors: CO (magenta), C (red), C^+ (yellow), H_3^+ (green), OH_x (blue), CH_x (cyan), and He^+ (black). As in Figure 2.1, the solid, dashed and dotted lines respectively represent results of the chemistry network in this work, the PDR code, and the NL99 network. Note that the NL99 network substantially underestimates the CO abundance at $n = 100\text{cm}^{-3}$, and overestimates the C^+ abundance (estimates of other species also fail in parts of parameter space). Overall, our network shows good agreement with the PDR code results. 19

2.3 Similar to Figure 2.2, except with the low cosmic-ray ionization rate $\xi_{\text{H}} = 10^{-17}\text{s}^{-1}\text{H}^{-1}$, as in panel (b) of Figure 2.1. At a low cosmic-ray rate, the NL99 network results are more similar to ours, although in certain parts of parameter space there are still large discrepancies. 20

2.4 Integrated column density of different species N_i as a function of N_H and A_V, for our network, the PDR code, and the NL99 network. The colors and symbols are the same as in Figures 2.2. The cosmic-ray ionization rate here is $\xi_{\text{H}} = 2 \times 10^{-16}\text{s}^{-1}\text{H}^{-1}$. See also Figures C.2 and C.4 in Appendix C for all species at densities $n = 50 - 1000\text{cm}^{-3}$. 22

2.5 Equilibrium temperature of the gas as a function of A_V (or N) and density n. The black, yellow, and magenta lines are contours of the equilibrium values for $2x(H_2)$, $x(C^+)/x_{C,tot}$ and $x(CO)/x_{C,tot}$ equal to 0.1 (dotted), 0.5 (dashed), and 0.9 (solid). The white dashed line shows the fit for the $x(CO)/x_{C,tot} = 0.5$ contour (magenta dashed line) in Equation (2.24). From left to right, the gas metallicities and dust abundances are set to be $Z = 0.2$, 0.5, and 1.0. The incident normalized radiation field $\chi = 1$, and cosmic-ray ionization rate $\xi_H = 2 \times 10^{-16} s^{-1} H^{-1}$. 26

2.6 Gas temperature as a function of A_V (or N) and n with solar metallicity $Z = 1$. Panel (a) varies the incident FUV radiation field strength $\chi = 1$, 10, and 100 while keeping the cosmic-ray ionization rate $\xi_H = 2 \times 10^{-16}$ $s^{-1} H^{-1}$. Panel (b) varies the cosmic-ray ionization rate $\xi_H = 10^{-17}$, 2×10^{-16}, and 10^{-15} $s^{-1} H^{-1}$, while keeping $\chi = 1$. The contours of the H_2, CO, and C^+ abundances, and the fit of the $x(CO)/x_{C,tot}$=0.5 contour, are also plotted, similar to Figure 2.5. 28

2.7 Temperature of the gas as a function of A_V (or N) and density n, similar to Figure 2.5. The incident radiation field and cosmic-ray ionization rate are set by Equations (2.22) and (2.23). The contours represent the abundances of H_2 (black), CO (magenta), and C^+ (yellow), and the fit of the $x(CO)/x_{C,tot}$=0.5 contour (white dashed), similar to Figures 2.5 and 2.6. 31

2.8 Comparison of equilibrium gas temperature with different chemical compositions. The leftmost panel is the same as the $Z = 1$ case in Figure 2.5, showing the fiducial model with our chemistry network. The other panels show cases where the formation rates of some species (CO, C, and/or H_2) are artificially set to zero, so the gas is forced to be in a state free of these molecules or atoms. The contours show the transition of H to H_2 (black), C^+ to C (yellow), and C to CO (magenta), similar to Figure 2.5. 32

2.9 Similar to Figure 2.5, but for Bonnor–Ebert mass of the gas as a function of A_V (or N) and density n. 33

2.10 Comparison between observations and our one-sided slab model. The *left* panel plots the column density N_i of chemical species at a given cloud A_V (or N). The lines show the results from our slab model with $n = 10$ cm^{-3} (dotted), $n = 100$ cm^{-3} (dashed), and $n = 1000$ cm^{-3} (solid). Different markers plot the observed abundances from the literature. Different colors represent different species, as shown in the legends. The *right* panel is similar to the left panel, but with the H_2 column density on the x-axis instead. . . 34

2.11 *Left panel:* abundances of CO/C vs. CO/H_2. The observational data are taken from BFJ2010, and lines of different colors show the results from different slab models (see legend), with $n = 100$ cm^{-3} (dashed), and $n = 1000$ cm^{-3} (solid). *Right panel*: similar to the left panel, but for CO/CH_x on the y-axis. The observed abundance is taken from Sheffer et al. (2008) and CF2004. See also Figure E.1 for a more detailed comparison between observations and our model with no grain-assisted recombination, and the depletion of carbon abundance. 35

3.1 The column density of all gas (N, *first row*), molecular gas (N_{H_2}, *second row*), CO (N_{CO}, *third row*), and the intensity of CO($J = 1 - 0$) line (W_{CO}, *last row*) in models RES-4pc, (*left*), RES-2pc (*middle*) and RES-1pc (*right*). The young (age < 40 Myr) star clusters/sink particles formed in the simulations are shown as filled circles in the first row with N. The area of the circles are proportional to the square root of the cluster masses, ranging from 10^3 $M_\odot$ to 10^5 $M_\odot$ (see legends in the top left panel), and the color of the circles indicates the cluster age, from 0 (magenta) to 40 Myr (blue). 53

3.2 Histograms of volume-weighted (*left*) and mass-weighted (*right*) density n in models RES-1pc (solid black), RES-2pc (dashed blue) and RES-4pc (dotted red). The y-axes is normalized to show the fraction of volume f_V or mass f_M in each density bin. The vertical lines indicate the density threshold for sink particle creation at the corresponding resolution in each model (Section 3.1.1). 55

3.3 Histograms of density, similar to Figure 3.2, but weighed by H_2 mass (*left*) and CO mass (*right*) in each cell. 56

3.4 Scatter plot of the H_2 abundance f_{H_2} versus the gas density n (*left*) and the effective extinction $A_{V,\rm eff}$ (*right*), for models RES-1pc (black), RES-2pc (blue) and RES-4pc (red). Each point is one grid cell in the simulations, and the area of each point is proportional to the volume of the grid cell for the corresponding resolutions. The yellow contours show the surface densities of the points above which 10%, 50% and 90% of points lie, for models RES-1pc (solid), RES-2pc (dashed) and RES-4pc (dotted). The black dashed line shows the equilibrium H_2 abundance assuming the FUV radiation is completely shielded (Equation (3.17)). 58

3.5 Similar to Figure 3.4, but for the CO abundance $f_{\rm CO}$. The black solid lines show where all carbon is in CO, i.e., $f_{\rm CO} = 1.6 \times 10^{-4}$. 59

3.6 Scatter plot of density n versus effective extinction $A_{V,\rm eff}$ in the models RES-1pc (black), RES-2pc (blue) and RES-4pc (red). The area of each point is proportional to the volume of the grid cell for corresponding resolutions. The contours show the surface densities of the points above which 10%, 50% and 90% points lie, for RES-1pc (solid), RES-2pc (dashed) and RES-4pc (dotted). The dashed lines roughly denote the regions where H, H_2, and CO form (see text in Section 3.2.1). 60

3.7 Scatter plot of CO column density $N_{\rm CO}$ versus $A_V(N_{\rm H_2})$ in the models RES-1pc (black), RES-2pc (blue) and RES-3pc (red). The area of each point is proportional to the area of the pixel for the corresponding resolution. The black solid line shows where all carbon is in CO, i.e., $f_{\rm CO} = 1.6 \times 10^{-4}$. The yellow symbols are UV absorption observations in Rachford et al. (2002) (triangles), Sheffer et al. (2008) (squares), Crenny & Federman (2004) (stars) and Burgh et al. (2010) (pentagons), compiled by Gong et al. (2017). The yellow solid line shows the result from the one-sided slab model with constant density $n = 100$ cm^{-3} in Gong et al. (2017). 61

3.8 *Left*: scatter plot of $W_{\rm CO}$ vs. $T_{\rm line}$ the excitation temperature of the CO($J = 1 - 0$) at line center (see Equation (3.22)); and *right*: $W_{\rm CO}$ vs. the velocity dispersion of the line σ_v. Both show models RES-1pc (black), RES-2pc (blue) and RES-4pc (red), with the area of points proportional to the area of the pixel at the corresponding resolution. The vertical dashed lines show the sub-grid micro-turbulence parameter (see Equation (3.8)). 63

3.9 Scatter plot of the gas temperature (triangles, upper branch) and excitation temperature of CO($J = 1-0$) line (circles, lower branch) versus gas density n in each cell for models RES-1pc (black), RES-2pc (blue) and RES-4pc (red). The area of each point is proportional to the volume of the grid cell at the corresponding resolution. The yellow dashed line is the estimation of $T_{\rm exc}$ in a two-level system model (see Section 3.2.1). 64

3.10 Scatter plot of the optical depth from the LVG approximation $\tau_{\rm LVG}$ vs. density n in each grid cell in model RES-1pc. The magenta circles are the binned average of $\tau_{\rm LVG}$, and the line is a broken power-law fit to the circles (Equation (3.27)). 66

3.11 Histograms of $W_{\rm CO}$ versus mass-weighted mean density $\langle n \rangle_M$ (*left*) and $A_V(N_{\rm H_2})$ (*right*). The color scale in the 2D histograms is proportional to the total CO luminosity $L_{\rm CO}$ in from each bin in model RES-1pc. The black solid contour of the color scale indicates the regions where 50% of the total CO emission comes from in model RES-1pc. The blue dashed and red dotted contours indicate 50% of the emission, but for models RES-2pc and RES-4pc. The 1D histograms show $L_{\rm CO}$ in each bin for models RES-1pc (black solid), RES-2pc (blue dashed) and RES-4pc (red dotted). 67

3.12 Histograms of $X_{\rm CO,20}$ weighted by $W_{\rm CO}$, in models RES-1pc (black solid), RES-2pc (blue dashed) and RES-4pc (red dotted). 68

3.13 *Left*: 2D histogram of $W_{\rm CO}$ versus $A_V(N_{\rm H_2})$ in model RES-1pc. The magenta filled circles and error bars show the average value and standard deviation of $W_{\rm CO}$ in each $A_V(N_{\rm H_2})$ bin. The black solid line shows the standard Milky Way value of $X_{\rm CO,MW,20} = 2$. The black dashed line shows the average $X_{\rm CO}$ in model RES-1pc, $\langle X_{\rm CO} \rangle_{20} = 1.02$. *Right*: similar to the left panel, but for the observations of Orion A and B molecular clouds by Ripple et al. (2013). The average $X_{\rm CO}$ for the Orion A and B clouds is $\langle X_{\rm CO} \rangle_{20} = 1.42$. 69

3.14 The abundance of H_2 (*left*) and CO (*right*) as a function of $t_{\rm chem}$ in TCHEM models. The y-axis is normalized by the final H_2 or CO abundance at $t_{\rm chem} =$ 50 Myr. 70

3.15 Scatter plot of $f_{\rm H_2}$ (*left*) and $f_{\rm CO}$ (*right*) versus density n for model TCHEM-5Myr. $f_{\rm H_2}$ and $f_{\rm CO}$ in each grid cell is normalized to the equilibrium abundance $f_{\rm H_2,final}$ and $f_{\rm CO,final}$ in that grid cell at $t_{\rm chem} = 50$ Myr (in model TCHEM-50Myr). 71

3.16 Similar to the left panel of Figure 3.13, but for model TCHEM-5Myr. 72

3.17 Total gas surface density N in models T-356Myr – T-416Myr. The star clusters are shown in circles, similar to Figure 3.1 top panels. 73

3.18 $\langle X_{\rm CO}\rangle$ vs. $\langle W_{\rm CO}\rangle$ (*left*), and $f_{\rm dark}$ vs. $\langle A_V\rangle_{\rm CO}$ (*right*) in models T-356Myr – T-416Myr. The dashed lines are the linear fits to the simulation data, and the solid lines are observations from Remy et al. (2017) (their Figure 12, note the line only shows the slope, not the absolute value) in the left panel, and the theoretical model of spherical molecular clouds in Wolfire et al. (2010) (their Figure 11) in the right panel. 76

3.19 Scatter plot of $X_{\rm CO}$ vs. $T_{\rm line}$ in models T-356Myr – T-416Myr. Each point is one pixel in the simulations. The red filled circles with error bars are the binned mean values and standard deviations of $X_{\rm CO}$. The blue solid line shows the observed relation in Kong et al. (2015). 77

3.20 The average $X_{\rm CO}$ binned in $A_V(N_{\rm H_2})$. The black lines are the simulation models of RES-1pc (solid), RES-2pc (thin dashed), TCHEM-5Myr (dash dotted), and T-356Myr – T-416Myr (thick dashed). The filled circles show the observations of molecular clouds in Lee et al. (in prep) for California (yellow), Orion A (red), and Orion B (magenta). The blue stars show the average of all Milky Way clouds in Lee et al. (in prep). The magenta triangles show the observations of Orion A by Ripple et al. (2013). The green solid line plots the γ-ray observations averaged over individual molecular clouds in Remy et al. (2017). 79

3.21 $\langle X_{\rm CO}\rangle_{20}$ as a function of beam size in different models (see label). The black circles (with error bars) are observations from Table 3.1. 80

3.22 $\langle X_{\rm CO}\rangle_{20}$ vs. $f_{\rm dark}$ in models RES-1pc and RES-2pc. Each point is for a different beam size in Figure 3.21. 81

C.1 Abundances of all independent species at densities $n = 50 - 200$ cm^{-3} in our network (solid), the PDR code (dashed), and the NL99 network (dotted), as a function of A_V/N. These figures are similar to Figure 2.2. Different species are represented by different colors as indicated in the legends. The abundance of H_2 is multiplied by a factor of 2×10^{-3}, i.e., if all hydrogen is in H_2, the black line will be at 10^{-3}. We have also plotted the abundances of CH and OH species from PDR code (cyan and blue dash-dotted lines), in addition to the sum of all CH_x and OH_x species. The cosmic-ray ionization rate $\xi_H = 2 \times 10^{-16}$ s^{-1}H^{-1}, and gas temperature is fixed at $T = 20$ K. . . . 110

C.2 Integrated column densities of all independent species at densities $n = 50 - 200$ cm^{-3} as a function of A_V/N, similar to Figure 2.4. Line colors and styles are the same as in Figure C.1. 111

C.3 Abundances of all independent species at densities $n = 500 - 1000$ cm^{-3}, similar to Figure C.1. 112

C.4 Integrated column densities of all independent species at densities $n = 500 - 1000$ cm^{-3}, similar to Figure C.2. 113

C.5 Abundances of species, similar to Figure C.1 and C.3, but for temperature in thermal equilibrium. 114

C.6 Integrated column densities of species in Figure C.5. 115

C.7 Abundances of species, similar to Figures C.1 and C.3, but for $Z = 0.1$. Note that the NL99 network is not shown here. 116

C.8 Integrated column densities of species in Figure C.7. 117

C.9 Comparison of the grain-assisted recombination rate of C^+ between Wolfire et al. (2008) (blue) and Weingartner & Draine (2001a) (black). The solid and dashed lines are results with $T = 20$ K and $T = 100$ K. The temperature T is in Kelvin, and the electron density n_e is in cm^{-3} in ψ. 118

C.10 Comparison of chemical abundances in our network with 0.6 times the grain-assisted recombination rates in Weingartner & Draine (2001a) (solid), the original Weingartner & Draine (2001a) rates (dotted), and the PDR code (dashed). The temperature is in thermal equilibrium. 119

C.11 Integrated column densities of species in Figure C.10. 120

C.12 Comparison of chemical abundances in our network (solid), the PDR code (dashed), and the PDR code with grain surface reactions in Hollenbach et al. (2009) (dotted). The temperature is in thermal equilibrium. 121

C.13 Integrated column densities of species in Figure C.12. 122

C.14 Abundances and column densities of species at density $n = 100$ cm^{-3} in our network (solid), and the *PyPDR* code (dashed), as a function of A_V/N. This is similar to Figures C.1 and C.2, but with the dashed lines showing the *PyPDR* code instead of the Wolfire PDR code. We have also plotted the abundances of CH and OH species from the *PyPDR* code (cyan and blue dash-dotted lines), in addition to the sum of all CH_x and OH_x species. The cosmic-ray ionization rate $\xi_H = 2 \times 10^{-16}$ s^{-1}H^{-1}, and gas temperature is fixed at $T = 20$ K. The reactions of grain-assisted recombination of ions are excluded in our network to be consistent with *PyPDR*. 123

E.1 Similar to the right panel of Figure 2.10, but with no grain-assisted recombination of ions (*left*), or depletion of gas-phase carbon abundance by a factor of 10 (*right*). 128

Chapter 1

Introduction

1.1 Chemistry in the Star Forming Interstellar Medium

Chemistry plays a key role in the interstellar medium (ISM) and star formation. In the ISM, a range of chemical species acts as agents for heating and cooling of the gas, regulating the gas temperature. Specific atomic and molecular species provide observational tracers for the gas physical properties, such as density and temperature. One of the most important molecules in the ISM is carbon monoxide (CO). CO is a main coolant for most of the molecular ISM via its rotational transitions (Goldsmith & Langer, 1978; Neufeld & Kaufman, 1993; Neufeld et al., 1995; Omukai et al., 2010), and also widely used as an observational tracer for molecular hydrogen (H_2) and star forming regions in both our Milky Way and other galaxies (e.g., Bolatto et al., 2008; Leroy et al., 2008; Roman-Duval et al., 2010; Saintonge et al., 2011a; Kennicutt & Evans, 2012; Tacconi et al., 2013; Bolatto et al., 2013a; Dobbs et al., 2014; Heyer & Dame, 2015, see also Section 1.2). Cooling by CO enables gas to reach low temperatures at which it collapses gravitationally to form stars. In return, feedback from star formation affects the chemical state of the ISM, as far-ultraviolet (FUV) radiation from massive stars dissociates and ionizes the gas. In particular, photodissociation of CO produces C, and ionization of C produces C^+, with their fine structure lines among the most

important coolants of atomic gas (Wolfire et al., 1995, 2003). The turbulence generated by supernova explosions leads to mixing of the gas composition and also changes the gas density distribution.

Traditionally, steady-state 1D photodissociation region (PDR) models with complex chemical networks have been used intensively to understand the detailed chemical structure of the ISM (e.g., Kaufman et al., 1999; Le Petit et al., 2006; Röllig et al., 2007; Wolfire et al., 2008, 2010; Hollenbach et al., 2012). Although much progress has been made using PDR models, solving the time-dependent equations is necessary for accurate abundances and temperature in the dynamic ISM. Typical star forming giant molecular clouds (GMCs) are not in chemical equilibrium (Leung et al., 1984; Papadopoulos et al., 2004), and are pervaded by supersonic turbulence that creates complex internal structure on dynamical timescales comparable to chemical timescales (Mac Low & Klessen, 2004; Glover et al., 2010). In recent years, efforts have therefore been increasing to incorporate time-dependent chemistry within both local (Walch et al., 2015; Girichidis et al., 2016) and global (Richings & Schaye, 2016a,b) galactic hydrodynamic and magnetohydrodynamic numerical simulations of the ISM. However, the full chemical network used in PDR models is too computationally expensive to incorporate in large numerical simulations. Modeling the chemical evolution of a group of $N_{\rm spec}$ species requires solving coupled ordinary differential equations (ODEs) of $N_{\rm spec}$ dimensions. Because the chemical timescales in the reaction set have extreme variation, the set of ODEs is usually very stiff and has to be solved implicitly, which results in a computational cost scaling as $N_{\rm spec}^3$.

For this reason, various authors have proposed approximations to simplify the chemical network for gas in star-forming regions (Nelson & Langer, 1997, 1999; Keto & Caselli, 2008; Glover et al., 2010; Richings et al., 2014). The general approach is to reduce the number of species, retaining only hydrogen and the most important species for cooling and observation, such as C^+, C, and CO. The number of reactions can also be reduced by capturing just the most important formation and destruction pathways for these species. Glover & Clark

(2012a) compared a number of simplified networks by looking at the C^+, C, CO, and temperature distributions in 3D simulations of turbulent molecular clouds. They found that all of the models they explored give similar results for density and temperature distributions, suggesting the gas thermodynamics is not very sensitive to the detailed chemistry. The CO distribution, however, is very different in various networks. They concluded that the simplified network of Nelson & Langer (1999, hereafter NL99) reproduces the CO abundance in more complicated models of Glover et al. (2010), and therefore recommend the NL99 network for simulating CO formation.

However, there are several limitations to the work of Glover & Clark (2012a). They did not carry out a detailed comparison between the different networks and more complex PDR models. Moreover, the comparisons they made are only under limited physical conditions. Notably, they used a cosmic-ray ionization rate $\xi_{\rm H} = 10^{-17}$ $\rm s^{-1}H^{-1}$, which is an order of magnitude lower than the recent estimates from observations of Milky Way molecular clouds, $\xi_{\rm H} \approx 2 \times 10^{-16}$ $\rm s^{-1}H^{-1}$ (Indriolo et al., 2007; Hollenbach et al., 2012). We show that when using the realistic cosmic-ray ionization rate, the NL99 network significantly underproduces CO compared to observations (see Section 2.2).

In chapter 2, we propose a new lightweight and accurate chemical network for following carbon and hydrogen chemistry in simulations of the atomic and molecular ISM. In Section 2.1, we describe our chemical network (which is an extension of NL99), related heating and cooling processes, and numerical methods. Then we carry out detailed comparison with both a PDR code and the original NL99 network in Section 2.2. Finally, in Section 2.3, we apply our network to simple 1D cloud models, and show the results from these applications in comparison to observations.

1.2 The $X_{\rm CO}$ Conversion Factor

Molecular clouds are the birth places of stars. In addition, molecular gas is the dominant ISM component in dense and shielded environments. Measuring the properties of molecular clouds is therefore critical to understanding the ISM and star formation in the Milky Way and beyond. However, the most abundant molecule in the ISM, molecular hydrogen H_2, is not directly observable in emission at typical ISM temperatures due to its low mass and lack of dipole moment. As a result, the second most abundant molecule, CO, is often used as an observational tracer for H_2. The standard technique uses the conversion factor $X_{\rm CO}$ to relate the observed velocity-integrated intensity of CO($J = 1 - 0$) line emission $W_{\rm CO}$ to the H_2 column density $N_{\rm H_2}$,

$$N_{\rm H_2} = X_{\rm CO} W_{\rm CO}. \tag{1.1}$$

Although the CO($J = 1 - 0$) line emission is bright and easy to detect with ground based radio telescopes, it is often very optically thick. Many observational studies have measured $X_{\rm CO}$ by deriving the H_2 mass independently from dust emission or extinction, gamma-ray emission, or the virial theorem (e.g. Dame et al., 2001; Lombardi et al., 2006; Strong & Mattox, 1996; Solomon et al., 1987). Surprisingly, the value of $X_{\rm CO}$ only varies within a factor of ~ 2 for many molecular clouds in the Milky Way and local disk galaxies. This has motivated the adoption of a constant standard $X_{\rm CO}$ conversion factor in the literature, $X_{\rm CO,MW} = 2 \times 10^{20}$ cm^{-2}K^{-1}km^{-1}s (see review by Bolatto et al., 2013b).

It is important to note that this standard $X_{\rm CO}$ is an average value for nearby molecular clouds on scales of tens of parsecs. $X_{\rm CO}$ is empirically known to vary both on small scales, and for molecular clouds in different environments. One of the earliest studies of $X_{\rm CO}$, Solomon et al. (1987), suggested that $X_{\rm CO}$ varies by a factor of a few for molecular clouds in the Milky Way, decreasing with increasing CO luminosity. Recent high-resolution observations have found that $X_{\rm CO}$ can vary by more than an order of magnitude on parsec scales, although the averages of $X_{\rm CO}$ over individual molecular clouds are within a factor of ~ 2 of the standard

Milky Way value (Pineda et al., 2008; Ripple et al., 2013; Lee et al., 2014b; Kong et al., 2015; Imara, 2015). Beyond nearby molecular clouds, $X_{\rm CO}$ in the Galactic center is a factor of ~ 4 lower than the mean value in the disk (Blitz et al., 1985; Ackermann et al., 2012), and similar results are found for the central regions in nearby spiral galaxies (Sandstrom et al., 2013). High surface density starburst regions have $X_{\rm CO}$ significantly below $X_{\rm CO,MW}$ (e.g. Downes & Solomon, 1998; Bolatto et al., 2013b, and references therein). Observations also indicate $X_{\rm CO}$ can be much higher than the standard Milky Way value in low metallicity galaxies (Israel, 1997; Leroy et al., 2011).

Theoretical models and numerical simulations have provided insights into the $X_{\rm CO}$ conversion factor. Wolfire et al. (1993a) constructed spherical cloud models with a photodissociation region (PDR) code, and suggested that $X_{\rm CO}$ is only weakly dependent on the incident FUV radiation field strength, and insensitive to the small variations in metallicity up to a reduction of metallicity by a factor of 5 relative to the solar neighborhood. These models rely on simple assumptions about cloud structure and kinematics. To model molecular clouds with more realistic structure, Glover & Mac Low (2011) and Shetty et al. (2011a,b) carried out 3D turbulent box simulations with chemistry and radiation transfer, and found similar cloud-average $X_{\rm CO}$ to the standard observed value (with significant variations on smaller-than-cloud scales). Shetty et al. (2011b) concluded that $X_{\rm CO}$ has a weak dependence on gas density, temperature, and velocity, and the nearly constant $X_{\rm CO}$ is the result of the limited range of physical properties found in the nearby molecular clouds. However, these simulations consider molecular clouds to be isolated from the large scale galactic ISM, and their key physical properties such as the average density and velocity dispersion are set artificially as the initial conditions of the simulations and prescribed turbulent driving. In recently years, more efforts have been made to investigate $X_{\rm CO}$ in global galaxy simulations (Narayanan et al., 2011, 2012; Feldmann et al., 2012; Duarte-Cabral et al., 2015). With resolutions of tens of parsecs, however, global galaxy simulations cannot resolve substructures in molecular clouds, and sub-grid models are generally required to estimate the CO emission. There is

no systematic study of the dependence of $X_{\rm CO}$ on the numerical resolution in the literature. Moreover, the comparisons between simulations and observations are often focused on the cloud-average $X_{\rm CO}$. Despite the rich observational data, little comparison has been made regarding to the variation of $X_{\rm CO}$ within molecular clouds on parsec or smaller scales. Furthermore, as observations of galactic and extragalactic molecular gas probe a range of scales, it is important to understand how $X_{\rm CO}$ may vary with the effective area of a radio beam.

In chapter 3, we present a new study of the $X_{\rm CO}$ conversion factor in MHD galactic disk simulations with solar neighborhood conditions and $1-4$ pc resolution. The molecular clouds are formed self-consistently within the multiphase ISM by gravity and stellar feedback. We investigate the dependence of $X_{\rm CO}$ on numerical resolution, non-equilibrium chemistry, variation in large-scale ISM structure and star formation rates, and the observational beam size. Our analyses also identify the density and shielding conditions that are required for H_2 and CO formation (which differ significantly) in realistic clouds, and break down the dependence of $W_{\rm CO}$ on microphysical properties. Additionally, we perform detailed comparisons with observations of $X_{\rm CO}$ in nearby molecular clouds at parsec scales. In Section 3.1, we describe the method of our simulations and the parameters in the numerical models. In Section 3.2, we show our results and comparisons with observations. The main findings of this work are summarized in Section 3.3.

Chapter 2

A simple and accurate network for hydrogen and carbon chemistry in the interstellar medium

2.1 The Chemical Model

2.1.1 Chemical Reaction Network

General Framework

The chemical network in this chapter is listed in in Tables A.1 and A.2, and described in detail in Appendix A. Our chemical network is based on the NL99 network in Nelson & Langer (1999) and Glover & Clark (2012a), with significant modification and extension. Eighteen species are considered: H, H_2, H^+, H_2^+, H_3^+, He, He^+, O, O^+, C, C^+, CO, HCO^+, Si, Si^+, e, CH_x and OH_x. Following NL99, CH_x (including CH, CH_2, CH^+, CH_2^+, CH_3^+) and OH_x (including OH, H_2O, OH^+, H_2O^+ H_3O^+) are pseudo-species, and their treatment is described in Appendix A.2 and A.3. Among the 18 species in our network, 12 of them are independently calculated, and 6 of them, H, He, C, O, Si and e, are derived from conservation

of total hydrogen, helium, carbon, oxygen, and silicon nuclei, and the conservation of total charge. [1] The gas-phase abundances of total helium nuclei are $x_{\rm He,tot} = n_{\rm He,tot}/n = 0.1$. The gas-phase abundance of total carbon, oxygen, and silicon nuclei are assumed to be proportional to the gas metallicity relative to the solar neighborhood $Z_{\rm g}$, and we adopt the values $x_{\rm C,tot} = 1.6 \times 10^{-4} Z_{\rm g}$ (Sofia et al., 2004), $x_{\rm O,tot} = 3.2 \times 10^{-4} Z_{\rm g}$ (Savage & Sembach, 1996), and $x_{\rm Si,tot} = 1.7 \times 10^{-6} Z_{\rm g}$ (Cardelli et al., 1994). We do not explicitly follow the evolution of dust grains, but instead assume that the grain-assisted reaction rates scale with the dust abundance relative to the solar neighborhood Z_d. We assume the gas metallicity Z_g and dust abundance Z_d vary simultaneously, and use a single parameter for metallicity relative to the solar neighborhood,

$$Z = Z_{\rm g} = Z_{\rm d}. \tag{2.1}$$

We have updated all reaction rates in the original NL99 network, according to the most recent values in the UMIST (McElroy et al., 2013) and KIDA (Wakelam et al., 2010) catalogs, and other references in Tables A.1 and A.2. Notably, we have a higher rate of $C^+ + OH \rightarrow CO^+ + H$, and a higher rate of $C^+ + e \rightarrow C$ by including both radiative and dielectronic recombination. These higher rates lower the electron abundance and aid the formation of OH_x and HCO^+, resulting in more efficient CO formation.

We have also modified and extended the NL99 network, as described in detail in Appendix A.1. One important extension is the addition of grain-assisted recombination of C^+ and He^+. Although Glover & Clark (2012a) concluded these grain reactions do not affect CO formation at the low cosmic-ray ionization rate $\xi_{\rm H} = 10^{-17} {\rm s}^{-1} {\rm H}^{-1}$, we found that with the updated cosmic-ray ionization rate $\xi_{\rm H} = 2 \times 10^{-16} {\rm s}^{-1} {\rm H}^{-1}$ (Indriolo et al., 2007, 2015), these

[1] We have compared the approach of using conservation laws with directly calculating the abundance of all species from rate equations, and found the results are the same. When calculating the abundance of H, C, O, and e from conservation laws, we assume all CH_x and OH_x are in the form of CH and OH. Because the abundance of CH_x and OH_x is usually very small compared to the hydrogen in H or H_2, carbon in C, C^+ or CO, oxygen in O, and electrons provided by H^+ or C^+, this assumption has no significant effect on the chemical network.

reactions are critical for CO formation at moderate densities $n \lesssim 1000$ cm^{-3}. This is because electrons formed by cosmic-ray ionization inhibit CO formation, while He^+ ions formed by cosmic rays destroy CO (Bisbas et al., 2015). Grain-assisted recombination reduces the abundance of e and He^+. With these extensions, we have 50 reactions in total, including collisional reactions, grain-assisted recombination and H_2 formation, photodissociation by FUV radiation, and cosmic-ray ionization.

Photochemistry

The photodissociation reactions induced by FUV depend on the radiation field strength. We assume that the incident radiation field scales with the standard interstellar radiation field determined by Draine (1978), using the parameter χ as the field strength relative to $J_{\rm FUV} = 2.7 \times 10^{-3}$erg cm^{-2}s^{-1} ($G_0 = 1.7$ in Habing (1968) units). The photochemistry reaction rates appropriate for this radiation field are listed in Table A.2.

In optically thick regions, the radiation is attenuated by dust and by molecular line shielding. In a plane-parallel slab geometry with beamed incident radiation field from one direction, the photodissociation rates of optically thick regions $R_{\rm thick}$ can be related to the rates in optically thin regions $R_{\rm thin}$ by

$$R_{\rm thick} = \chi R_{\rm thin} f_{\rm shield} = \chi R_{\rm thin} f_{\rm dust} f_{\rm s}, \tag{2.2}$$

where $f_{\rm dust} = \exp(-\gamma A_V)$ is the dust-shielding factor and $f_{\rm s}$ is the self-shielding of C, CO and H_2 (see text below). The values of the parameter γ appropriate for the different reactions are listed in Table A.2. The visual extinction A_V is calculated as

$$A_V = \frac{N Z_{\rm d}}{1.87 \times 10^{21} {\rm cm}^{-2}} \ , \tag{2.3}$$

where $N = N_{\rm H} + 2N_{\rm H_2}$ is the total hydrogen column density along the line of sight. This corresponds to $R_V \equiv A_V / E(B-V) = 3.1$ and $N/E(B-V) = 5.8 \times 10^{21}$cm^{-2}, appropriate

for the diffuse ISM (Bohlin et al., 1978). In clouds with slab geometry and isotropic radiation field impinging from one side (Section 2.3), $f_{\rm shield}$ is an average value calculated from different incident angles. For more general, non-slab geometry, photo rates at a given location would be calculated by angle averages of Equation (2.2), as both χ and $f_{\rm shield}$ vary with direction.

For photoelectric heating on dust (see Section 2.1.2), the heating rate depend on the radiation field strength between $6 - 13.6$ eV which affects the charge states of grains. For radiation in the FUV important for the photoelectric effect, we use a constant dust cross-section $\sigma_{\rm d,PE} = 10^{-21} Z_{\rm d} {\rm cm^2 H^{-1}} = 1.87 A_V/N$ to calculate the attenuation by dust,

$$\chi_{\rm PE}(N) = \chi f_{\rm dust,PE} = \chi \exp(-\sigma_{\rm d,PE} N); \tag{2.4}$$

our adopted cross-section is close to the value $1.8 A_V/N$ used in previous PDR models.

In addition to dust shielding, we also include the H_2 self-shielding, CO self-shielding, C self-shielding, and shielding by H_2 of CO and C. The photodissociation rate of H_2 can be written as

$$R_{\rm thick,H_2} = \chi R_{\rm thin,H_2} f_{\rm dust} f_{\rm s,H_2}(N_{\rm H_2}). \tag{2.5}$$

We use the results in Draine & Bertoldi (1996) for H_2 self-shielding:

$$f_{s,{\rm H_2}}(N_{\rm H_2}) = \frac{0.965}{(1+x/b_5)^2} + \frac{0.035}{(1+x)^{0.5}} \exp[-8.5\times10^{-4}(1+x)^{0.5}], \tag{2.6}$$

where $x \equiv N_{\rm H_2}/(5\times10^{14}{\rm cm^{-2}})$ and $b_5 = b/({\rm km/s})$ for b the velocity dispersion. In regions where $2x({\rm H_2}) = 2n({\rm H_2})/n \gtrsim 0.1$, the self-shielding of H_2 is in the wings of the line profile, and the H_2 fraction is not sensitive to the choice of b_5. Here we use a constant value $b_5 = 3$.

Similarly, the photodissociation rate of CO can be written as

$$R_{\rm thick,CO} = \chi R_{\rm thin,CO} f_{\rm dust} f_{\rm s,CO}(N_{\rm CO}, N_{\rm H_2}). \tag{2.7}$$

The shielding factor $f_{\rm s,CO}(N_{\rm CO}, N_{\rm H_2})$ is interpolated from Table 5 in Visser et al. (2009) for a given column density of CO and H_2. This accounts for both the CO self-shielding and the shielding of CO by H_2. In Visser et al. (2009) Table 5, the velocity dispersion of CO is assumed to be $b({\rm CO}) = 0.3{\rm km/s}$ [2], the excitation temperature $T_{\rm ex}({\rm CO}) = 5{\rm K}$ and $N(^{12}{\rm CO})/N(^{13}{\rm CO}) = 69$.

Lastly, the photodissociation rate of C is

$$R_{\rm thick,C} = \chi R_{\rm thin,C} f_{\rm dust} f_{\rm s,C}(N_{\rm C}, N_{\rm H_2}). \tag{2.8}$$

We adopt the treatment in Tielens & Hollenbach (1985). The shielding factor $f_{\rm s,C}(N_{\rm C}, N_{\rm H_2}) = \exp(-\tau_{\rm C}) f_{\rm s,C}({\rm H_2})$, where $\tau_{\rm C} = 1.6 \times 10^{-17} N_{\rm C}/{\rm cm}^{-2}$, $f_{\rm s,C}({\rm H_2}) = \exp(-r_{\rm H_2})/(1 + r_{\rm H_2})$, and $r_{\rm H_2} = 2.8 \times 10^{-22} N_{\rm H_2}/{\rm cm}^{-2}$.

2.1.2 Heating and Cooling Processes

The heating and cooling processes included in our models are listed in Table B.1, and described in detail in Appendix B. Here we describe the general processes we considered. The time rate of change of the gas thermal energy per H nucleus $e_{\rm g,sp}$ is given by

$$\frac{{\rm d}e_{\rm g,sp}}{{\rm d}t} = \Gamma_{\rm tot} - \Lambda_{\rm tot}. \tag{2.9}$$

The total heating rate per H nucleus is

$$\Gamma_{\rm tot} = \Gamma_{\rm PE} + \Gamma_{\rm CR} + \Gamma_{\rm H2gr} + \Gamma_{\rm H2pump} + \Gamma_{\rm H2diss}, \tag{2.10}$$

where $\Gamma_{\rm PE}$ is the heating from the photoelectric effect on dust, $\Gamma_{\rm CR}$ the cosmic-ray heating, $\Gamma_{\rm H2gr}$ the heating from H_2 formation on dust grains, $\Gamma_{\rm H2pump}$ the heating from H_2 UV pumping, and $\Gamma_{\rm H2diss}$ the heating from H_2 photodissociation. For typical environments in

[2] We have also tried to use the $b({\rm CO}) = 3{\rm km/s}$ results in Visser et al. (2009), and found that $f_{\rm s,CO}$ changes within $\sim 50\%$, and the CO fraction is not sensitive to $b({\rm CO})$.

the cold atomic and molecular ISM, the photoelectric heating dominates at $A_V \lesssim 1$ and the cosmic-ray heating dominates at $A_V \gtrsim 1$.

The total cooling rate per H nucleus is

$$\Lambda_{\rm tot} = \Lambda_{\rm line} + \Lambda_{\rm dust} + \Lambda_{\rm rec} + \Lambda_{\rm H2coll} + \Lambda_{\rm Hion}, \tag{2.11}$$

where $\Lambda_{\rm line}$ is the line cooling by atomic and molecular species, $\Lambda_{\rm dust}$ the cooling from gas–grain collisions, $\Lambda_{\rm rec}$ the cooling by electron recombination on dust grain, $\Lambda_{\rm H2coll}$ the cooling by collisional dissociation of H_2, and $\Lambda_{\rm Hion}$ the cooling by collisional ionization of H. The line cooling dominates in typical atomic and diffuse molecular ISM where the gas densities are not high enough for dust cooling to be important ($n \lesssim 10^6$ cm^{-3}). We include line cooling of O, C, C^+ fine structure lines, the Lyα line of H, CO rotational lines, and the H_2 vibration and rotational lines.

The gas temperature is related to the gas energy by (Krumholz, 2014)

$$T = \frac{e_{\rm g,sp}}{c_{v,\rm H}}. \tag{2.12}$$

The specific heat at constant volume $c_{v,\rm H} = \frac{1}{2} k_B f$, where $k_B = 1.381 \times 10^{-16}$ erg K^{-1} is the Boltzmann constant and $f = \sum f_s x_s$ is the degree of freedom in all species per H nucleus. For H, He, He^+, H^+, and e, $f_s = 3$ from translational degrees of freedom. For H_2, the excitation temperature for rotational and vibrational levels are $\theta_{\rm rot} = 170.6$K and $\theta_{\rm vib} = 5984$K (Tomida et al., 2013). Assuming a fixed ortho-to-para ratio of H_2, the rotational and vibrational heat capacities of H_2 are very small at typical molecular cloud temperatures $T \lesssim 50$K. Therefore, we ignore the contribution of rotational and vibrational levels of H_2 to the specific heat, and

simply use

$$c_{v,\mathrm{H}} = \frac{3}{2}k_B(x_{\mathrm{H}} + x_{\mathrm{H}_2} + x_{\mathrm{H}^+} + x_{\mathrm{He}} + x_{\mathrm{He}^+} + x_{\mathrm{e}}) \tag{2.13}$$

$$= \frac{3}{2}k_B[(1 - x_{\mathrm{H}_2}) + x_{\mathrm{He,tot}} + x_{\mathrm{e}}]. \tag{2.14}$$

2.1.3 Numerical Method

We consider a simple one-dimensional slab model with uniform density n, and FUV radiation incident from one side of the slab, similar to typical 1D PDR (photodissociation region) models. The incident radiation field is expected to be relatively isotropic over 2π steradians. In Section 2.2, we use the approach of Wolfire et al. (2010) in order to compare with their PDR code: the isotropic radiation field is approximated by assuming a unidirectional flux incident at an angle of 60° to the normal of the slab surface. Thus, with the incident radiation field strength χ, the field strength at the perpendicular column density N from the slab surface will be $\chi_{\mathrm{eff}} = (\chi/2)f_{\mathrm{shield}}(2N)$, where the factor 1/2 in χ comes from the one-sided slab and the factor 2 in N comes from the angle of 60°. In Section 2.3, we directly calculate the isotropic radiation field strength by averaging over the incident angels.

In each model, we divide a slab into 10^3 logarithmically spaced grid zones in the range of $N = 10^{17}/Z - 10^{22}/Z$ cm^{-2}. In each zone, walking inward from the lowest N to the highest N in order, we calculate the equilibrium chemistry and temperature. This is because the chemical states of all exterior zones are needed to calculate the radiation field shielding factor for the next zone.

The evolution of abundances of chemical species $x_s = n_s/n$ is determined by a set of chemical reactions:

$$\begin{aligned}\frac{\mathrm{d}x_s}{\mathrm{d}t} =& \sum_{i,j}(\pm k^{ij}_{\mathrm{2body,s}} n x_i x_j) + \sum_i (\pm k^i_{\mathrm{gr,s}} n x_i) \\ &+ \sum_i (\pm k^i_{\mathrm{cr,s}} x_i) + \sum_i (\pm k^i_{\gamma,\mathrm{s}} x_i).\end{aligned} \tag{2.15}$$

Here $k^{ij}_{\rm 2body,s}$, $k^{i}_{\rm gr,s}$, $k^{i}_{\rm cr,s}$, and $k^{i}_{\gamma,\rm s}$ are the rates for the two-body, grain surface, cosmic-ray and photodissociation reactions listed in Tables A.1 and A.2 that have species s either as a reactant or product. x_i and x_j are the abundance of the corresponding reactant species, and the sign is negative if x_s is a reactant of the chemical reaction and positive if x_s is a product. The chemical reactions in Equation (2.15) and the energy evolution in Equation (2.9) give a coupled ODE (ordinary differential equation) system of 13 variables (12 independently calculated species and 1 energy equation). The derived species (H, He, C, O, Si, and e) are not directly calculated from Equation 2.15, but from the conservation of atomic nuclei and charge. To efficiently solve this set of stiff ODEs, we use the open-source CVODE package (Cohen et al., 1996), which adopts a method of implicit backward differentiation formulas.

2.2 Code Test and Comparison

In this section, we test the agreement between the greatly simplified chemical network in this work and a PDR code with much more sophisticated chemistry and radiation transfer. We also compare with the widely used original NL99 network and point out the importance of our modifications.

The PDR code used here is derived from the Tielens & Hollenbach (1985) PDR code, which has been in continuous use, and updated and maintained since its original inception. The model has been used extensively to analyze observations in a diverse set of environments including the diffuse ISM (e.g., Wolfire et al., 2003, 2008; Sonnentrucker et al., 2015), low-mass molecular clouds (Lee et al., 2014c; Burton et al., 2015), Galactic GMCs (Wolfire et al., 2010), intense Galactic PDRs (Sheffer et al., 2011), and extragalactic PDRs (e.g., Kaufman et al., 2006; Stacey et al., 2010). Recent updates to the chemistry, heating, and cooling rates are given in Wolfire et al. (2010), Hollenbach et al. (2012) and Neufeld & Wolfire (2016). The code calculates the thermal balance temperature and steady-state abundances of 74 species using 322 reactions. The dominant gas-phase species are H, He, C, O, H_2,

O_2, OH, CO, H_2O, e^-, H^+, He^+, C^+, O^+, OH^+, CO^+, H_2O^+, HCO^+, H_3O^+, H_2^+, H_3^+, CH^+, CH_2^+, CH_3^+, CH, CH_2, CH_3, CH_4, Mg, Mg^+, Si, Si^+, SiH_2^+, SiH, SiO, Fe, Fe^+, S, S^+, SiO^+, SO^+, $HOSi^+$,H_2^*, H^-, PAH^-, PAH, and PAH^+. Also included are fluorine and chlorine chemistry as in Neufeld & Wolfire (2009). Freeze-out of atoms and molecules on grains (such as CO and H_2O) and grain surface reactions such as OH and H_2O formation are included as in Hollenbach et al. (2009, 2012) but are turned off for most of the comparisons in this work. The effects of grain surface reactions on chemistry are discussed in Appendix C.5. For comparison to the results presented in this work, we use a modified version of the code in which the geometry is plane parallel and the density is constant. In addition, we use the photoionization, photodissociation, and cosmic-ray induced photo rates from Heays et al. (2017), consistent with Tables A.1 and A.2 in this work. We use the approximation in Wolfire et al. (2010) for an isotropically incident radiation field assuming a single ray incident at 60 degrees to the normal and use the H_2 self-shielding treatment as in Tielens & Hollenbach (1985).

The NL99 network we compare with is similar to that used in Glover & Clark (2012a). It is based on two main parts: the CO chemistry in NL99, and the hydrogen chemistry in Glover & Mac Low (2007). In order to make a meaningful comparison of the difference between the CO chemistry in this work and the NL99 network, we updated all the reaction rates in the NL99 network to the values in this work (see Tables A.1 and A.2), and adopted the same gas-phase atomic abundances of carbon and oxygen. We have also added the H_3^+ destruction channel $H_3^+ + e \rightarrow 3H$ in addition to the reaction $H_3^+ + e \rightarrow H_2 + H$ in Nelson & Langer (1999), to have the hydrogen chemistry consistent with that used in Glover et al. (2010) and this work. [3]

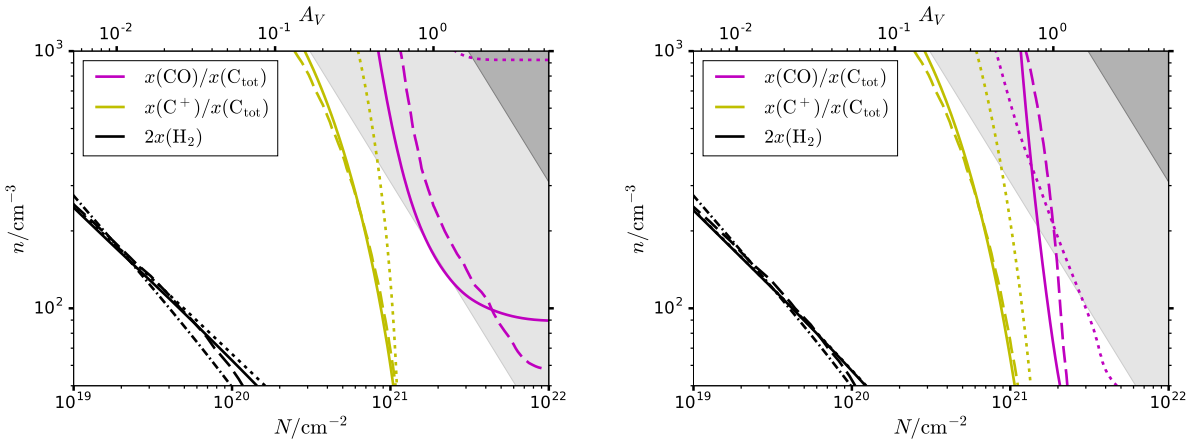
We run slab models described in Section 2.1.3 with densities $n = 50 - 1000$ cm^{-3}, and ambient radiation field $\chi = 1$. We compare the results based on the NL99 network (as described above) with those from our chemical network. We similarly run the PDR code, and

[3]Caution needs to be taken here: if the H_3^+ destruction channel $H_3^+ + e \rightarrow 3H$ is not included, the artificially elevated H_3^+ abundance would cause CO to form much more efficiently then it should.

compare results, using the same configurations of density and incident radiation field. Here we focus on the comparison of the chemistry network and fix the temperature at $T = 20$ K and metallicity $Z = 1$. We have also made comparisons with the PDR code at $Z = 0.1$, and by solving the chemistry and temperature simultaneously. The detailed results are shown in Appendix C.3 and C.2. The treatment of grain-assisted recombinations in the PDR code is based on the results in Wolfire et al. (2008), and is slightly different from the rate in Weingartner & Draine (2001a) that we adopted. Thus, for the purpose of comparison, we multiply the rates of reactions 2-5 in Table A.2 by a factor of 0.6 in our models to match the rates in the PDR code. For further discussions of the grain-assisted recombination rates, see Appendix C.4. We use the recent measurement of the primary cosmic-ray ionization rate per hydrogen $\xi_{\rm H} = 2 \times 10^{-16} {\rm s}^{-1} {\rm H}^{-1}$ (Indriolo et al., 2007) if not specified otherwise. We also run some fixed temperature models with the low cosmic-ray ionization rate $\xi_{\rm H} = 10^{-17} {\rm s}^{-1} {\rm H}^{-1}$, in order to compare with results from the previous literature that adopted this rate (e.g. Glover & Clark, 2012a).

In our models, from the edge of the slab to the inside, the FUV radiation field is attenuated by both dust and molecular lines. As N and A_V increases, the abundance of molecular hydrogen increases due to H_2 self-shielding, while the atomic hydrogen abundance decreases. The C^+ abundance decreases due to dust shielding, with most carbon in C at intermediate A_V. Above $A_V \sim 1$, cosmic-ray ionization of H_2 creates H_3^+, which reacts with C and O to form CH_x and OH_x molecules. CH_x and OH_x molecules further mediate the formation of CO.

Figure 2.1 illustrates the locations of the H to H_2, C^+ to C, and C to CO transitions in the N–n plane. In panel (a) of Figure 2.1, we show that there is a very good agreement on the location of the C^+ to C transition between our chemical network and the PDR code (yellow solid and dashed lines). There are some differences in the location of C to CO transitions (magenta solid and dashed lines), but the detailed abundance and column of CO agrees within a factor of ~ 2 at a given A_V (see Figures 2.2 and 2.4, and discussions below). The



(a) $\xi_{\mathrm{H}} = 2 \times 10^{-16}\mathrm{s}^{-1}\mathrm{H}^{-1}$

(b) $\xi_{\mathrm{H}} = 10^{-17}\mathrm{s}^{-1}\mathrm{H}^{-1}$

Figure 2.1: Contours showing locations of H to H_2, C^+ to C, and C to CO transitions in the N–n plane. The magenta, yellow, and black lines are contours where $x_{\mathrm{CO}}/x_{\mathrm{C_{tot}}}$, $x_{\mathrm{C}^+}/x_{\mathrm{C_{tot}}}$, and $2x_{\mathrm{H_2}}$ are respectively equal to 0.5. The solid, dashed and dotted lines are the results of the chemistry network in this work, the PDR code, and the NL99 network, respectively. The black dashed-dotted line plots the analytic formula in Bialy & Sternberg (2016) for the H to H_2 transition. The left panel (a) is using cosmic-ray ionization rate $\xi_{\mathrm{H}} = 2 \times 10^{-16}\mathrm{s}^{-1}\mathrm{H}^{-1}$ (Indriolo et al., 2007), and the right panel (b) is using the old low cosmic-ray ionization rate $\xi_{\mathrm{H}} = 10^{-17}\mathrm{s}^{-1}\mathrm{H}^{-1}$. The gas temperature is fixed at $T = 20\mathrm{K}$. The regions where the H_2 formation timescale is comparable to or shorter than the typical turbulence crossing timescale are shaded dark gray for $t_{\mathrm{H_2}}/t_{\mathrm{dyn}} < 1$ and light gray for $t_{\mathrm{H_2}}/t_{\mathrm{dyn}} < 10$ (see Equation (2.17)).

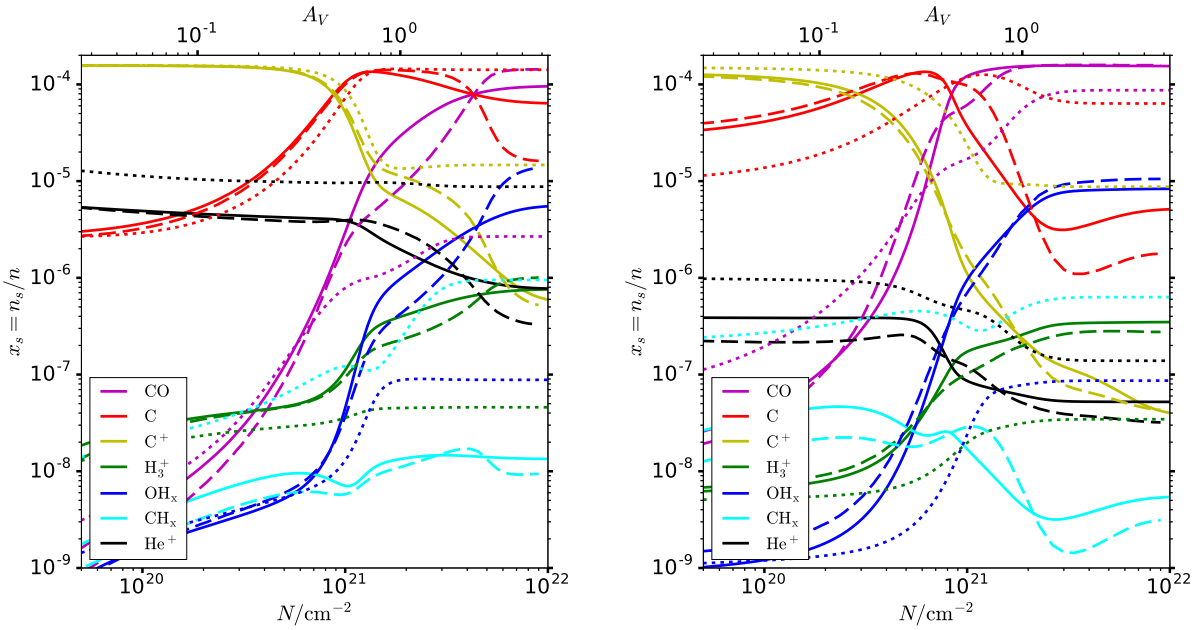
NL99 network, however, yields both C^+ to C and C to CO transitions at a significantly higher A_V (yellow and magenta dotted lines). Especially at $n \lesssim 500\mathrm{cm}^{-3}$, the CO abundance in the NL99 network remains very low up to $A_V = 5$. This is inconsistent with observations of CO in diffuse molecular clouds with $n \lesssim 200\mathrm{cm}^{-3}$, and $A_V \lesssim 1$ (Magnani et al., 1985; Burgh et al., 2007; Sheffer et al., 2008; Goldsmith, 2013). The failure of the NL99 network here is mainly due to two reasons. Firstly and most importantly, the NL99 network does not include C^+ recombination on dust grains. Because the rate of C^+ recombination on dust grains is higher than the direct recombination with free electrons, the C^+ to C transition is pushed to higher A_V, and the C^+ abundance at $A_V = 1 - 5$ regions is elevated. This impedes CO formation: the electrons from C^+ destroy H_3^+, which is an important reactant for the first step of CO

formation. Second, the NL99 network does not include He^+ recombination on dust grains, which is the main destruction channel for He^+ at solar metallicity. In well-shielded regions, the reaction $He^+ + CO \rightarrow C^+ + O + He$ is the main channel for CO destruction. Therefore, the elevated He^+ abundance also suppresses CO in the NL99 network (see also Figure 2.2 for H_3^+ and He^+ abundances). Without recombination of C^+ and He^+ on grains, the transition of C to CO in the NL99 network occurs at at a quite high density, $n > 500$ cm^{-3}.

The H to H_2 transition is the same in our network and the NL99 network, and shows very good agreement with the PDR code. The same H to H_2 transition in our network and the NL99 network is simply because the hydrogen chemistry in both networks are identical, and H_2 formation is largely unaffected by other species. Our results also show very good agreement with the analytic formula for the H to H_2 transition in Bialy & Sternberg (2016) (see their Equation (39)).

Panel (b) in Figure 2.1 shows an interesting comparison using the low cosmic-ray ionization rate $\xi_H = 10^{-17}s^{-1}H^{-1}$. With a low cosmic-ray rate, the location of the C to CO transition is similar in the NL99 network and our network. This is because with the low cosmic-ray rate, CO destruction by He^+ is less efficient due to the lower abundance of He^+ created by cosmic rays, and the CO abundance is now mainly limited by photodissociation. The dependence of the photodissociation rate on dust shielding determines the A_V at which CO forms. Although CO abundances are similar at $\xi_H = 10^{-17}s^{-1}H^{-1}$, there are significant differences in the abundances of other species such as C^+ between the NL99 network and our network (see Figure 2.3). Thus, the apparent similarity in the CO transition at the low cosmic-ray rate is deceptive. Using the low cosmic-ray ionization rate, Glover & Clark (2012a) compared the NL99 network with the larger Glover et al. (2010) network, considering the CO distribution in turbulent clouds. They reached the conclusion that the NL99 network is sufficiently accurate for simulating CO formation. However, here we show that with a more realistic cosmic-ray ionization rate, the NL99 network significantly underesti-

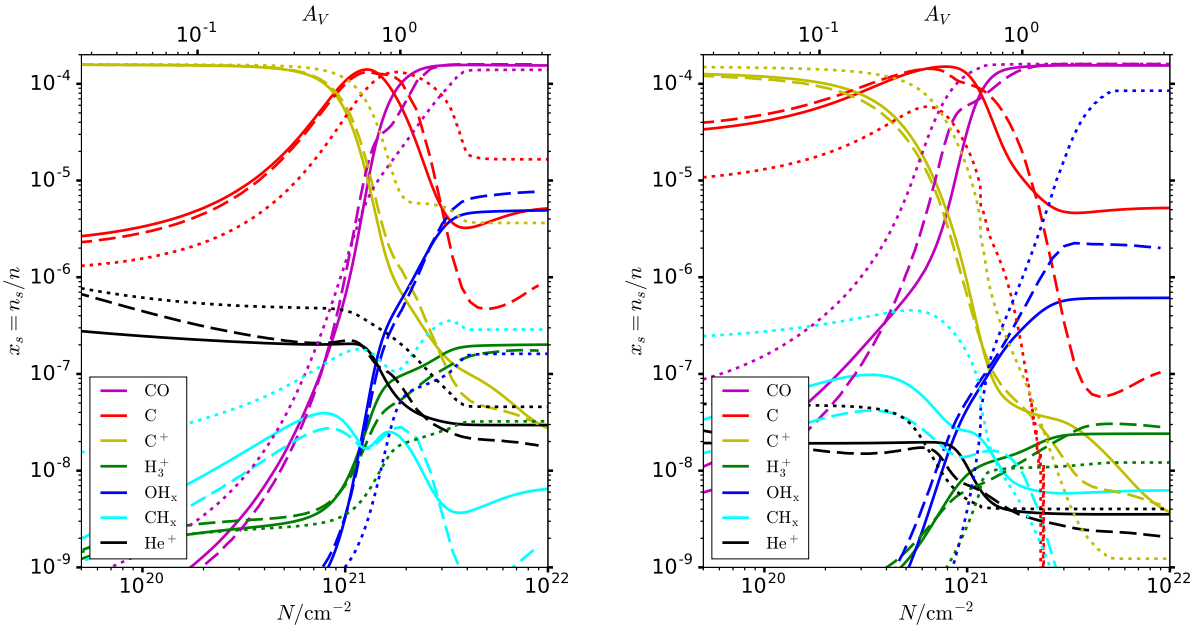
mates the CO abundance, and the grain assisted recombinations of C^+ and He^+ are very important for obtaining correct CO abundances.



(a) $n = 100$ cm^{-3} (b) $n = 1000$ cm^{-3}

Figure 2.2: Abundances of different species as a function of A_V and N at densities $n = 100\mathrm{cm}^{-3}$ in panel (a) and $n = 1000\mathrm{cm}^{-3}$ in panel (b). The cosmic-ray ionization rate here is $\xi_{\mathrm{H}} = 2 \times 10^{-16}\mathrm{s}^{-1}\mathrm{H}^{-1}$, corresponding to panel (a) of Figure 2.1. Gas temperature is fixed at $T = 20$ K. See also Figures C.1 and C.3 in Appendix C for abundances of all species at densities between $n = 50 - 1000\mathrm{cm}^{-3}$. The abundances of different species $x_i = n_i/n$ are plotted in different colors: CO (magenta), C (red), C^+ (yellow), H_3^+ (green), OH_x (blue), CH_x (cyan), and He^+ (black). As in Figure 2.1, the solid, dashed and dotted lines respectively represent results of the chemistry network in this work, the PDR code, and the NL99 network. Note that the NL99 network substantially underestimates the CO abundance at $n = 100\mathrm{cm}^{-3}$, and overestimates the C^+ abundance (estimates of other species also fail in parts of parameter space). Overall, our network shows good agreement with the PDR code results.

Figures 2.2 and 2.4 plot the abundances of different species as a function of A_V and N for the three networks at $\xi_{\mathrm{H}} = 2 \times 10^{-16}\mathrm{s}^{-1}\mathrm{H}^{-1}$. Figure 2 shows the abundance comparisons for $\xi_{\mathrm{H}} = 10^{-17}\mathrm{s}^{-1}\mathrm{H}^{-1}$. Overall, there is a very good agreement between our chemical network and the PDR code for C^+, C, CO, and H_3^+, which are the main observable species in our network. It is remarkable that our network also reproduces the column densities N_i at a



(a) $n = 100$ cm^{-3} (b) $n = 1000$ cm^{-3}

Figure 2.3: Similar to Figure 2.2, except with the low cosmic-ray ionization rate $\xi_{\mathrm{H}} = 10^{-17}\mathrm{s}^{-1}\mathrm{H}^{-1}$, as in panel (b) of Figure 2.1. At a low cosmic-ray rate, the NL99 network results are more similar to ours, although in certain parts of parameter space there are still large discrepancies.

given A_V of all other species with errors less than a factor of ~ 2, even for the largely simplified pseudo-species $\mathrm{OH_x}$ and $\mathrm{CH_x}$. This indicates that our simplified network successfully captures the main chemical pathways of these species. There are also some differences to be pointed out: Compared to the PDR code, the CO abundance is lower at $n = 100\mathrm{cm}^{-3}$ and $A_V \gtrsim 2$, and higher at $A_V \sim 1$ in our network. This is partly due to the difference in the grain-assisted recombination rates, as discussed in Appendix C.4, and partly due to the approximation of using pseudo-species $\mathrm{OH_x}$, which does not capture all the details of $\mathrm{OH_x}$ formation and destruction. For similar reasons that lead to the difference in the CO abundance, there are also discrepancies in the abundances of other species such as C, He^+, $\mathrm{OH_x}$, and $\mathrm{CH_x}$ at $n = 100\mathrm{cm}^{-3}$ and $A_V \gtrsim 2$. However, since the differences mainly occur in a limited range of A_V, the differences in column density in Figure 2.4 are small.

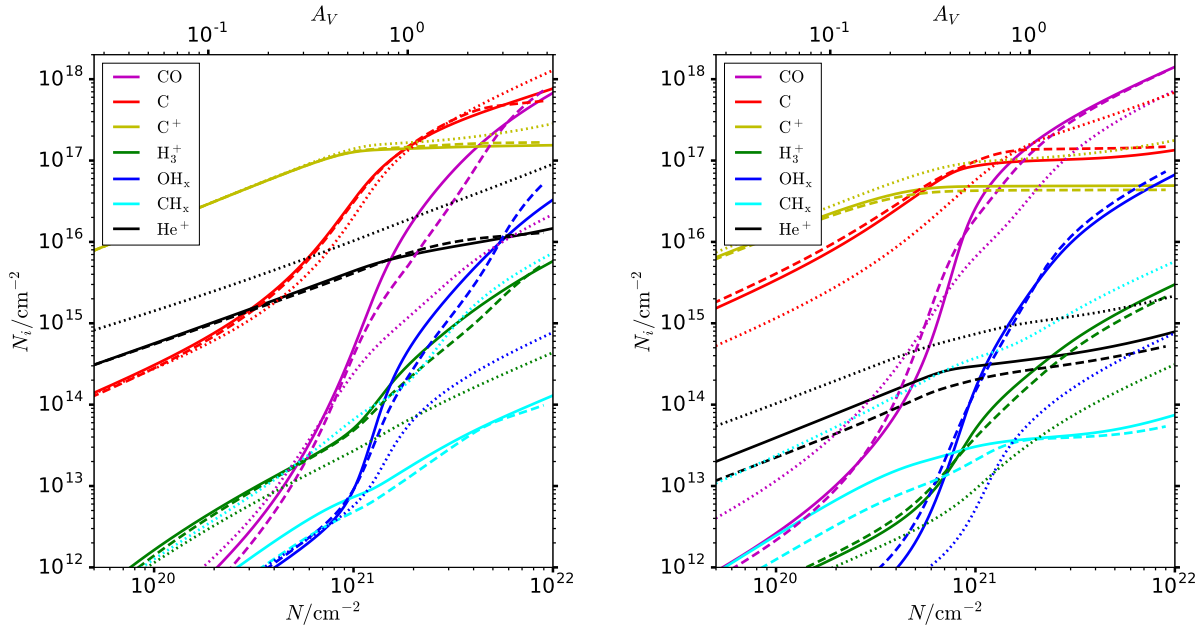
The NL99 network, however, fails to reproduce the equilibrium abundances in the PDR code. The CO abundance is too low as a result of the high C^+ and He^+ abundances, as discussed above. The NL99 network also leads to a much higher CH_x abundance, due to the absence of the important destruction channel of CH reacting with H. Therefore, we conclude that our new chemical network is preferred over the NL99 network. With one additional species (O^+) and nineteen additional reactions, we find that the increase in computational cost is about 50%.

To cross-check with other PDR codes, we have also run a comparison with the publicly available *PyPDR*[4] code provided by Simon Bruderer. *PyPDR* has been shown to agree well with the PDR bench mark in Röllig et al. (2007), and therefore is a good point of comparison with the existing model literature. However, *PyPDR* does not include grain-assisted recombination of ions, which is important for CO formation as discussed above. Appendix C.6 shows that our chemical network (without grain assisted recombinations) agrees very well with the *PyPDR* code, which further validates our results.

2.3 Sample applications

Observations of a wide range of galaxies show a correlation between the surface density of the star formation rate (SFR) and the surface density of molecular gas (e.g. Bigiel et al., 2008, 2011; Saintonge et al., 2011b; Genzel et al., 2010; Jameson et al., 2016). Although in some models it has been proposed that star formation is associated with gas that is shielded enough for H_2 to form (Krumholz et al., 2009), any relationship with H_2 would have to be coincidental rather than causal, because H_2 is not an active coolant in cold gas. In principle, H_2 might be important because it is a prerequisite for CO formation, and CO is the dominant coolant in the environment of star formation, at least when the metallicity is not extremely low (Glover & Clark, 2012c). However, the cooling provided by C^+ can also bring gas to quite low temperatures, so that it is able to collapse gravitationally at small scales (Glover &

[4] `http://www.mpe.mpg.de/~simonbr/research_pypdr/index.html`



(a) $n = 100$ cm^{-3} (b) $n = 1000$ cm^{-3}

Figure 2.4: Integrated column density of different species N_i as a function of N_H and A_V, for our network, the PDR code, and the NL99 network. The colors and symbols are the same as in Figures 2.2. The cosmic-ray ionization rate here is $\xi_{\mathrm{H}} = 2 \times 10^{-16}\mathrm{s}^{-1}\mathrm{H}^{-1}$. See also Figures C.2 and C.4 in Appendix C for all species at densities $n = 50 - 1000\mathrm{cm}^{-3}$.

Clark, 2012b). Thus, the association of star formation with the molecular phase may simply be because both chemical and dynamical timescales are shorter at higher density, and the shielding that limits photodissociation also limits photoheating (see also Krumholz et al., 2011).

Regardless of the reason for the correlation between molecular gas and star formation, quantifying the relationship between gas and star formation empirically requires tracers of all gas phases. Atomic gas is easily identified with the 21 cm transition, but H_2 is difficult to observe directly due to the high excitation temperature of its rotational levels. CO is often used as a tracer of H_2, but CO is known to be difficult to detect in metal-poor galaxies, and even when detected, the star formation rate per CO luminosity is much higher than that in the Milky Way-like galaxies (e.g. Taylor et al., 1998; Leroy et al., 2007; Schruba et al.,

2011, 2012; Hunt et al., 2015). Moreover, CO is not necessarily a linear tracer of H_2 (Bolatto et al., 2013a).

Here, we use simple slab models to explore the correlations between chemical state (especially $x(\mathrm{CO})$ and $x(H_2)$) and temperature, while also exploring the dependence of both properties on n, N, χ, ξ_{H} and Z. We also explore the mean abundances of various species on average cloud density and column, and compare with observations.

2.3.1 CO as a Tracer of H_2 and Cold Gas

Following Krumholz et al. (2011), we investigate how well CO and H_2 trace cold gas in the ISM with different metallicities. Krumholz et al. (2011) used semi-analytic models to estimate the H_2 and CO abundances and separately computed the equilibrium temperature for gas cooled either by C^+ or by CO. Here, we instead use our chemical network and self-consistent cooling to solve for the equilibrium chemical composition and temperature of the gas. We run one-dimensional slab models described in Section 2.1.3 at a range of densities $n = 10^1 - 10^4 \mathrm{cm}^{-3}$, and compute the chemical and temperature state of the gas in the A_V–n plane. We also run models with different metallicities, incident radiation field, and cosmic-ray ionization rate to study the dependence of gas properties on these parameters.

It should be noted that in the realistic ISM, the timescales of cooling and chemical reactions are different, and the dynamical timescales set by turbulence may be shorter than these. Thus, the equilibrium chemical and thermal state does not necessarily apply in the real ISM. This is particularly an issue for H_2, because the formation time is $t_{\mathrm{H_2}} \approx 10^7$ yr $Z_d^{-1} \left(\frac{n}{100\mathrm{cm}^{-3}}\right)^{-1}$ at $T = 100$K (see line 24 in Table A.1), whereas typical dynamical timescales in dense gas are (see Equation (B.8))

$$t_{\mathrm{dyn}} = L/v_{\mathrm{turb}}(L) \sim 1\mathrm{Myr}\ (L/\mathrm{pc})^{1/2}. \tag{2.16}$$

For transient clouds produced by turbulent compression, even if the mean shielding column is sufficient for the equilibrium H_2 abundance to be high, the H_2 formation timescale may be longer than the cloud lifetime. For example, the criterion $t_{H_2} < t_{dyn}$ is equivalent to

$$\begin{aligned} Z_d^2 \left(\frac{n}{100\ \mathrm{cm}^{-3}}\right)\left(\frac{N}{10^{21}\ \mathrm{cm}^{-2}}\right) > 31, \text{ or} \\ Z_d A_V \left(\frac{n}{100\ \mathrm{cm}^{-3}}\right) > 17 \end{aligned} \tag{2.17}$$

which is well above the equilibrium H/H_2 transition in Figure 2.1.

In high column density self-gravitating clouds with supersonic turbulence, the mass-weighed density $\langle n \rangle_M$ is proportional to N^2, $\langle n \rangle_M \propto N^2$ (See Equation (D.11), where the second term dominates over the first term). Combining this with Equation (2.17), gives

$$\begin{aligned} N &\gtrsim 4.3 \times 10^{21} Z_d^{-2/3}\ \mathrm{cm}^{-2}, \text{ or} \\ A_V &\gtrsim 2.3\ Z_d^{-2/3} \end{aligned} \tag{2.18}$$

for $t_{H_2} < t_{dyn}$. Equation (2.18) suggests that for a molecular cloud with $A_V \gtrsim 1$, although molecular hydrogen is difficult to form at an average density $n \sim 100\ \mathrm{cm}^{-3}$ (Equation (2.17)), turbulence can compress most of the gas to reach to a higher density regime and enable the cloud to become molecular in a shorter timescale.

For gravitationally bound clouds that live longer than several flow-crossing times, the dynamical cycling of gas to the unshielded surface may limit the molecular abundance. The timescale for a fluid element in the cloud to travel through the unshielded region is $t_{sh} = L_{shield}/v_{turb}(L_{cloud})$, where L_{shield} is the length scale for H_2 to be self-shielded against the FUV radiation. Using Equation (52) in Sternberg et al. (2014), and the H_2 formation

rate on dust (see line 1 in Table A.2), the shielding length[5]

$$L_{\rm shield} = \frac{N}{n} \approx 1 \text{ pc } \chi \left(\frac{n}{100 \text{ cm}^{-3}}\right)^{-2}, \tag{2.19}$$

where n is the average (volume-weighted) density of the cloud. Adopting $v_{\rm turb}(L) \sim 1$ km/s $(L/{\rm pc})^{1/2}$, this yields:

$$t_{\rm sh} = 0.2 \text{ Myr } \chi \left(\frac{n}{100 \text{ cm}^{-3}}\right)^{-2} \left(\frac{L_{\rm cloud}}{10{\rm pc}}\right)^{-1/2}. \tag{2.20}$$

The timescale for H_2 photodissociation is $t_{\rm diss,H_2} = 1/k_{\rm diss,H_2} = 6 \times 10^2$ yr (the photodissociation rate $k_{\rm diss,H_2} = 5.6 \times 10^{-11}$ s^{-1}, see line 19 in Table A.2). Setting $t_{\rm sh} < t_{\rm diss,H_2}$ gives

$$\frac{1}{\chi} \left(\frac{n}{100 \text{ cm}^{-3}}\right)^{2} \left(\frac{L_{\rm cloud}}{10{\rm pc}}\right)^{1/2} > 3 \times 10^2; \tag{2.21}$$

when this condition is satisfied, molecules can avoid being destroyed by photodissociation over the timescale to cross the unshielded surface of the cloud. For example, a cloud of size 10 pc will require its density $n > 1.7 \times 10^3$ cm^{-3} to be fully molecular. Equation (2.21) shows that even in gravitationally bound clouds, the cycling of gas from the cloud interior to the surface can also limit the H_2 abundance in low density regimes. If the H_2 abundance is reduced by exposure to UV, other chemical pathways will also be strongly affected. Therefore, to fully investigate how well CO traces molecular gas, numerical simulations with time-dependent chemistry are needed. Still, we show that our simple models can provide insight into this important but complicated problem.

Figure 2.5 shows the equilibrium gas temperature in color scale, in comparison to the contours of equilibrium H_2, CO, and C^+ abundances. Across a wide range of metallicities

[5]This uses the approximation of $\ln(\alpha G/2+1) \approx \alpha G/2$ (see Equation (40) in Sternberg et al. (2014)). For the CNM in pressure equilibrium (Equation (2.22)), $\alpha G/2 \approx 1.3$, which makes the approximation good up to a factor of ~ 3. At $\alpha G/2 \approx 1$, most of the H column is built up in atomic regions (see Figure 7 in Sternberg et al. (2014)), and therefore we calculate the shielding length by $L_{\rm shield} = N/n$. Note, however, in the limit of $\alpha G/2 \gg 1$, i.e., for low density gas or highly illuminated PDR such as observed in Bialy et al. (2015), the dependence changes to $N \sim 2/\sigma_g \sim 10^{21}{\rm cm}^{-2}$, independent of αG, giving $L_{\rm shield} \sim 3{\rm pc}\ [n/(100{\rm cm}^{-3})]^{-1}$.

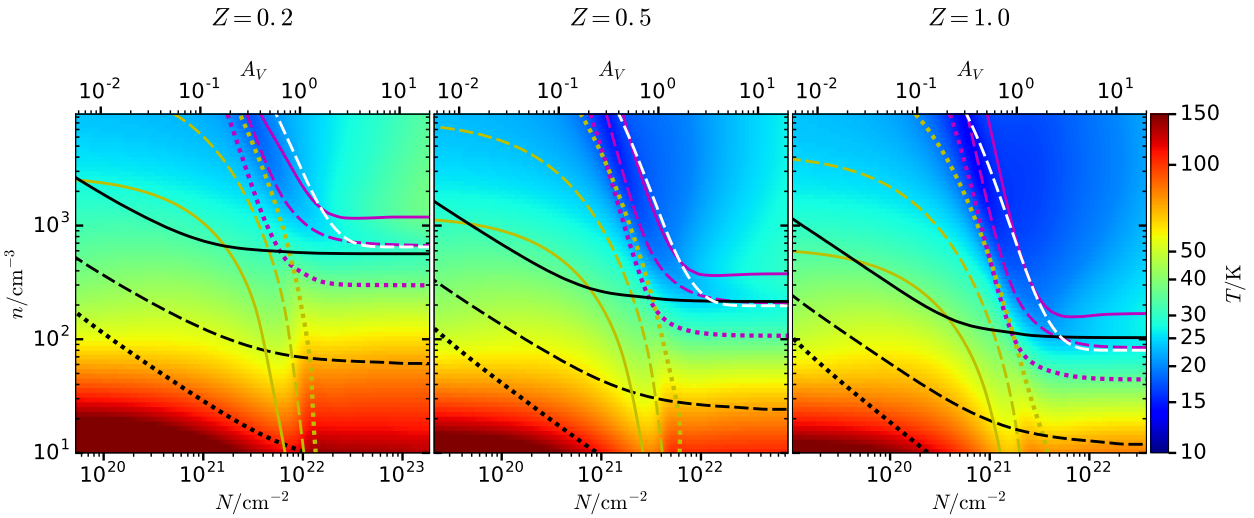


Figure 2.5: Equilibrium temperature of the gas as a function of A_V (or N) and density n. The black, yellow, and magenta lines are contours of the equilibrium values for $2x(\mathrm{H}_2)$, $x(\mathrm{C}^+)/x_{\mathrm{C,tot}}$ and $x(\mathrm{CO})/x_{\mathrm{C,tot}}$ equal to 0.1 (dotted), 0.5 (dashed), and 0.9 (solid). The white dashed line shows the fit for the $x(\mathrm{CO})/x_{\mathrm{C,tot}} = 0.5$ contour (magenta dashed line) in Equation (2.24). From left to right, the gas metallicities and dust abundances are set to be $Z = 0.2$, 0.5, and 1.0. The incident normalized radiation field $\chi = 1$, and cosmic-ray ionization rate $\xi_{\mathrm{H}} = 2 \times 10^{-16}\mathrm{s}^{-1}\mathrm{H}^{-1}$.

$Z = 0.2-1$, Figure 2.5 shows that gas that is mostly molecular is also at $T \lesssim 40$K. However, it is important to note that the coincidence of high H_2 abundance and low temperature is not causal. For gas in the range of Figure 2.5, most of the cooling is provided by C^+, C, and CO. Even if we artificially turn off the formation of H_2 and CO, the gas can still be cooled to $T \sim 20$K with C and C^+ cooling. We discuss this further in Section 2.3.3. At low metallicity, the minimum density required for gas to become molecular increases. This is because H_2 forms less efficiently when the dust abundance drops. At low enough n, the equilibrium $x(\mathrm{H}_2)$ is low even in very shielded regions. This is due to the destruction of H_2 by cosmic rays. The gas temperature is similar at $A_V \lesssim 1$ across $Z = 0.2 - 1$, because both the photoelectric heating and gas cooling are proportional to Z. At $A_V \gtrsim 1$, and also in low density and low metallicity regions, the cosmic-ray heating dominates, which is independent of metallicity. This leads to an increase of the gas temperature in these regions at low metallicity due to decreased gas cooling.

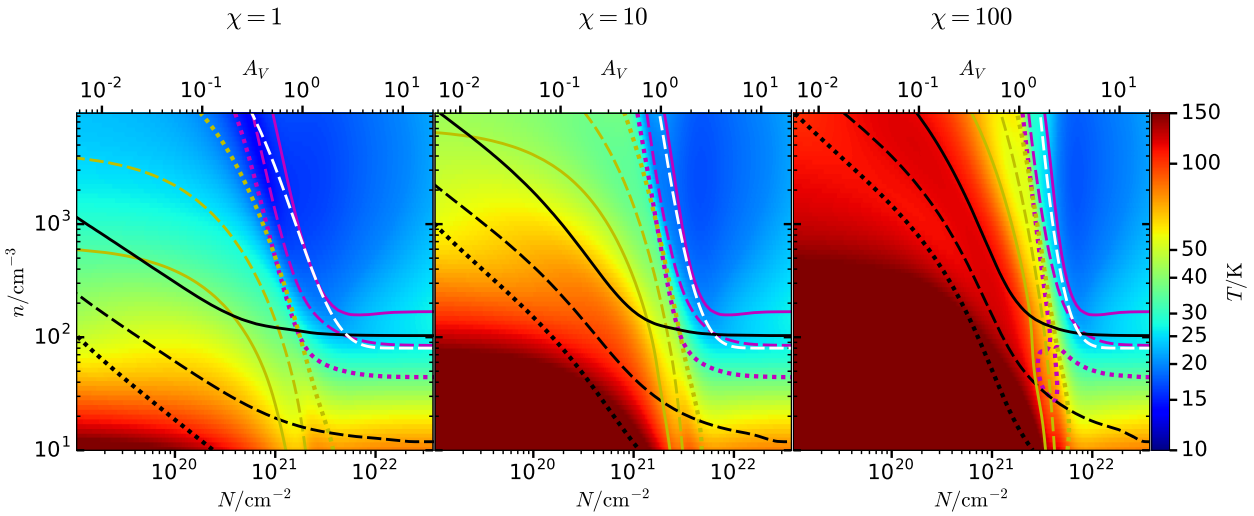
At solar metallicity ($Z = 1$), Figure 2.5 shows that the region of high CO abundance (where CO line cooling dominates) traces the lowest temperature $T \lesssim 20$K gas very well[6]. At very low metallicities, there is less dust shielding and collisional reactions between metal species occur at a reduced rate, leading to less efficient CO formation, and CO traces the temperature less well.

2.3.2 Dependence on χ, $\xi_{\rm H}$, and Z

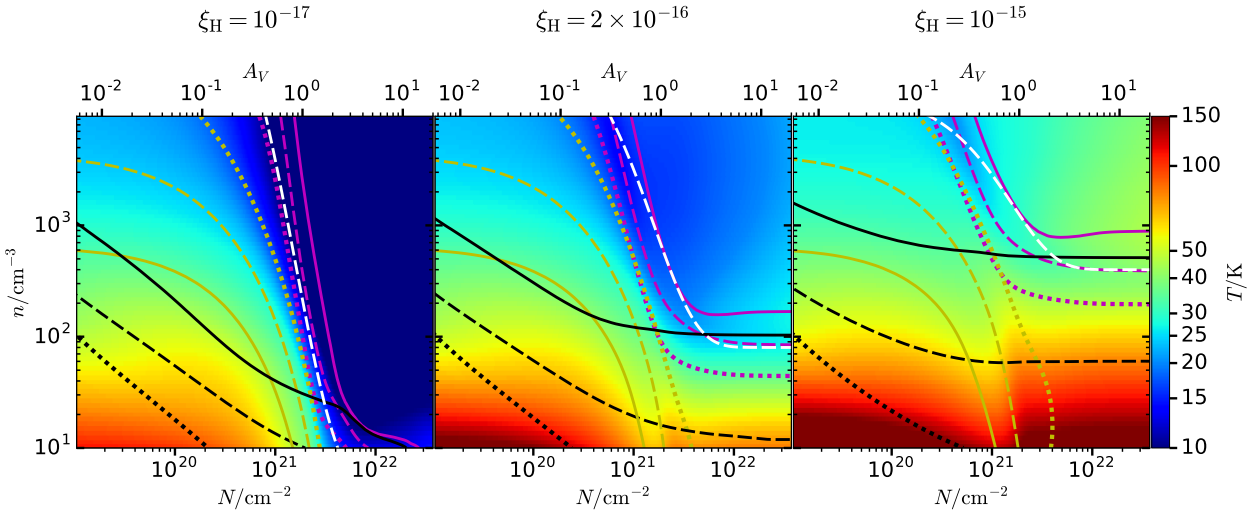
Figure 2.6 (a) shows that an increase of χ pushes the H_2-dominated region to higher A_V, and that even H_2 dominated gas can be at $T > 100$K if χ is large enough. Increasing the cosmic-ray rate requires higher density for the gas to become H_2-dominated, because cosmic rays can dissociate H_2 (Figure 2.6 (b)).

An increase (decrease) of χ moves the boundary of CO-dominated gas to higher (lower) A_V, because CO only forms in dust-shielded regions (Figure 2.6 (a)). Similarly, an increase (decrease) of $\xi_{\rm H}$ pushes the minimum density for CO up (down), because He^+ and C^+ formed in cosmic-ray reactions are harmful for CO formation (Figure 2.6 (b)). However, in both Figure 2.6 (a) and Figure 2.6 (b), the contours defining the CO-dominated region also clearly delimit the low temperature ($T \lesssim 20$K) gas, except at the highest levels of $\xi_{\rm H}$. The temperature of the bulk of the gas in the CO-dominated regime depends on $\xi_{\rm H}$ but not on χ. This is because when $x({\rm CO})/x_{\rm C,tot} \approx 1$, the heating and cooling are respectively dominated by cosmic-ray ionization and CO rotational transitions. The temperature is obtained by balancing Equation (B.1) (with Equation (B.3)) with Equation (B.5). We suggest that the temperature of CO, especially the optically thin isotopes, can be an indicator to probe the cosmic-ray ionization rate in dense molecular gas. Observations of star forming regions near the galactic center indicate that CO gas there is indeed warmer than that in the galactic disk (Güsten & Philipp, 2004; Ao et al., 2013; Bally & Hi-GAL Team, 2014). The higher cosmic ray production rate due to higher SFR in the galactic center may explain the elevated

[6]However, there is a subtlety in this: even if we artificially force CO not to form, C would have cooled the gas to similarly low temperatures (see Section 2.3.3).



(a) χ



(b) ξ_{H}

Figure 2.6: Gas temperature as a function of A_V (or N) and n with solar metallicity $Z = 1$. Panel (a) varies the incident FUV radiation field strength $\chi = 1$, 10, and 100 while keeping the cosmic-ray ionization rate $\xi_{\mathrm{H}} = 2 \times 10^{-16}$ $\mathrm{s}^{-1}\mathrm{H}^{-1}$. Panel (b) varies the cosmic-ray ionization rate $\xi_{\mathrm{H}} = 10^{-17}$, 2×10^{-16}, and 10^{-15} $\mathrm{s}^{-1}\mathrm{H}^{-1}$, while keeping $\chi = 1$. The contours of the H_2, CO, and C^+ abundances, and the fit of the $x(\mathrm{CO})/x_{\mathrm{C,tot}}$=0.5 contour, are also plotted, similar to Figure 2.5.

temperature of the CO gas there. However, if only the ^{12}CO ($J = 1 - 0$) line is observed, because it is usually optically thick, the luminosity of the line is determined mostly by the temperature at the cloud surface, where photoelectric heating can dominate over cosmic-ray heating. Therefore, as pointed out by Wolfire et al. (1993b), the luminosity of the CO ($J = 1 - 0$) line is mostly determined by the strength of UV radiation, instead of the cosmic-ray ionization rate.

In galactic disks where the warm and cold atomic gas are in pressure equilibrium, the typical density of the cold neutral medium (CNM) is related to the strength of the ambient radiation field approximately by $n_{\rm CNM} \propto \chi$ (Wolfire et al., 2003; Ostriker et al., 2010):

$$\frac{n_{\rm CNM}}{\chi} \approx 23. \tag{2.22}$$

Krumholz et al. (2009) adopted a similar relation for the density of cold atomic/molecular complexes. Assuming the ambient radiation field strength is proportional to the SFR, then $\chi \propto \Sigma_{\rm SFR}$, where $\Sigma_{\rm SFR}$ is the average rate of star formation per unit area in the galactic disk. In equilibrium, $\Sigma_{\rm SFR}$ is expected to be proportional to the weight of the ISM, which in general depends on both the gas surface density $\Sigma_{\rm gas}$ and the stellar density (Ostriker et al., 2010; Kim et al., 2011, 2013). In starburst regions where the gas dominates gravity, $\Sigma_{\rm SFR} \propto \Sigma_{\rm gas}^2$ (Ostriker & Shetty, 2011). Assuming that $\xi_{\rm H} \propto \Sigma_{\rm SFR}/\Sigma_{\rm gas}$ (Ostriker et al., 2010), and $\Sigma_{\rm SFR}/\Sigma_{\rm gas} \propto \Sigma_{\rm gas} \propto \sqrt{\chi}$, we consider the case in which

$$\xi_{\rm H} = 10^{-16}\sqrt{\chi}\ {\rm s}^{-1}{\rm H}^{-1}. \tag{2.23}$$

Using $\chi \propto n$ and $\xi_{\rm H} \propto \sqrt{\chi}$ based on Equations (2.22) and (2.23), Figure 2.7 plots the temperature of the gas in the n-N plane. Comparing to Figure 2.5, Figure 2.7 shows clearly that it is very difficult to form CO in metal-poor gas under typical diffuse-ISM conditions, implying gas densities must be enhanced by turbulence or gravity to be well above typical values in the CNM for CO to be present. However, at $Z = 1$, most of the carbon is in CO

at $A_V \gtrsim 2$ and $n \gtrsim 100$ cm^{-3}. Thus, in regions of galaxies where A_V and n are high enough, gas need not to be in gravitationally bound clouds to be molecular or to emit strongly in CO (see also Elmegreen, 1993). This implies that CO emission in the galactic center and starburst galaxies may arise largely from diffuse gas. Indeed, observations of CO lines in luminous infrared galaxies by Papadopoulos et al. (2012) found that most of the CO emission can come from warm and diffuse gas in these starburst environments. Figure 2.7 also shows that in metal-poor galaxies, C could be the most important tracer for shielded gas, as also noted by Glover & Clark (2016). However, the gas that is traced by C is not necessarily primarily molecular H_2.

We have also found a simple fit for the contour of $x(\mathrm{CO})/x_{\mathrm{C,tot}} = 0.5$ in the plane of n – A_V, given values of incident FUV radiation field, cosmic-ray ionization rate, and metallicity:

$$\frac{n_{\mathrm{crit,CO}}}{\mathrm{cm}^{-3}} = \left(4 \times 10^3 Z \xi_{\mathrm{H},16}^{-2}\right)^{\chi_{\mathrm{CO}}^{1/3}} \left(\frac{50\xi_{\mathrm{H},16}}{Z^{1.4}}\right), \tag{2.24}$$

where $n_{\mathrm{crit,CO}}$ is the critical value above which $x(\mathrm{CO})/x_{\mathrm{C,tot}} > 0.5$; $\xi_{\mathrm{H},16} = \xi_{\mathrm{H}}/(10^{-16}\mathrm{s}^{-1}\mathrm{H}^{-1})$; $\chi_{\mathrm{CO}} = \chi \exp(-\gamma_{\mathrm{CO}} A_V)$ is the effective radiation field for CO photodissociation accounting for dust attenuation, and $\gamma_{\mathrm{CO}} = 3.53$ is the dust-shielding factor of CO given in Table A.2. Figures 2.5-2.7 and 2.9 shows the fit in Equation (2.24) (white dashed line) against the true contour of $x(\mathrm{CO})/x_{\mathrm{C,tot}} = 0.5$ (magenta dashed line), demonstrating the good agreement between the two. We note that this fit is only tested here to be applicable in the range of $n \approx 10 - 10^4$ cm^{-3}, $\xi_{\mathrm{H}} \approx 10^{-17} - 10^{-15}$ s^{-1}H^{-1}, and $Z = 0.2 - 1$.

2.3.3 Are Molecules Necessary for Low Temperatures?

How sensitive is the gas temperature to the detailed chemistry? Glover & Clark (2012b) showed that in simulations of turbulent clouds, as long as the gas is shielded, atomic gas can reach similarly low temperatures as in molecular gas. Glover & Clark (2012a) also found that

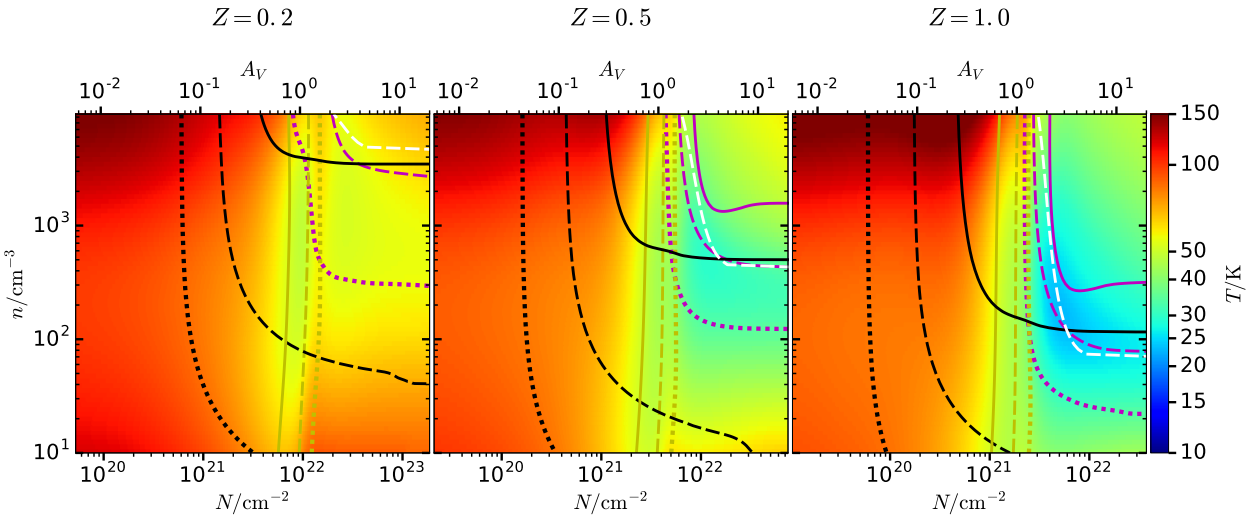


Figure 2.7: Temperature of the gas as a function of A_V (or N) and density n, similar to Figure 2.5. The incident radiation field and cosmic-ray ionization rate are set by Equations (2.22) and (2.23). The contours represent the abundances of H_2 (black), CO (magenta), and C^+ (yellow), and the fit of the $x(\mathrm{CO})/x_{\mathrm{C,tot}}$=0.5 contour (white dashed), similar to Figures 2.5 and 2.6.

the gas temperature in dense clouds can be very similar even if the CO and C abundances produced by different chemical networks vary by more than an order of magnitude.

To directly look into this question, we artificially force the gas into different chemical states by setting the formation rates of CO, C, and H_2 to zero (successively). Figure 2.8 shows that the equilibrium gas temperatures are very similar with completely different chemical states. C and C^+ can cool the gas just as well as CO.[7] H_2 only affects the temperature slightly by changing the specific heat of the gas. This confirms the conclusions in Glover & Clark (2012b): any correlation between molecular gas and low temperatures is likely to be coincidental instead of causal. Molecular gas traces low temperatures simply because molecules form in dense and shielded regions that are more efficient at cooling and less exposed to heating.

[7]Note that we assume the C and C^+ cooling is optically thin, whereas the optical depth effect is taken into account in CO cooling. This is why C and C^+ cool the dense gas to lower temperatures than CO in Figure 2.8. In reality, C and C^+ will also be optically thick at high columns.

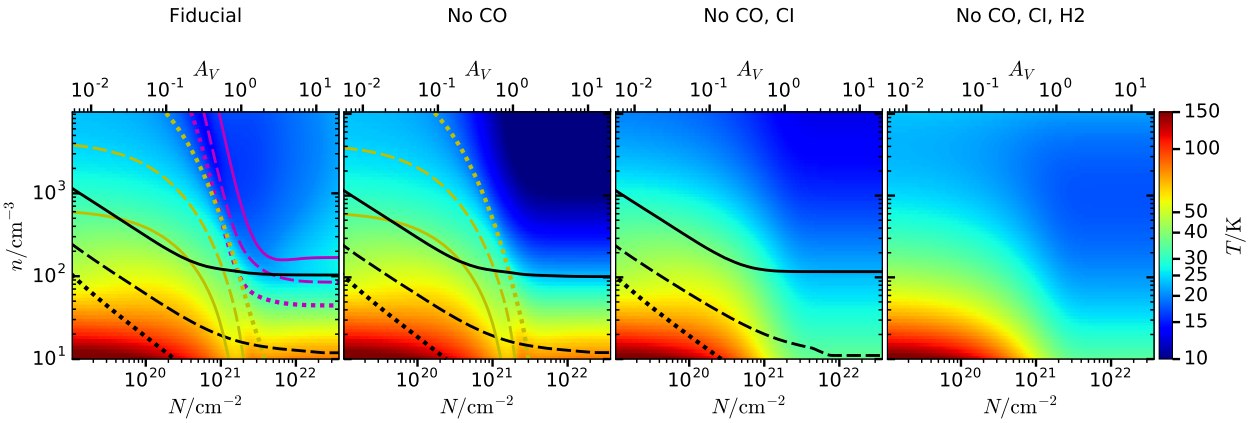


Figure 2.8: Comparison of equilibrium gas temperature with different chemical compositions. The leftmost panel is the same as the $Z = 1$ case in Figure 2.5, showing the fiducial model with our chemistry network. The other panels show cases where the formation rates of some species (CO, C, and/or H_2) are artificially set to zero, so the gas is forced to be in a state free of these molecules or atoms. The contours show the transition of H to H_2 (black), C^+ to C (yellow), and C to CO (magenta), similar to Figure 2.5.

2.3.4 Molecular Gas and Star Formation?

Krumholz et al. (2011) argued that H_2 traces star formation because H_2 forms in the same regions where the gas is more gravitationally unstable, or, quantitatively speaking, where the critical Bonnor–Ebert mass $M_{\rm BE} = 1.2 c_s^3 \left(\frac{\pi^3}{G^3\rho}\right)^{1/2} = 1.2 \left(\frac{\pi^3 k^3 T^3}{G^3 n \mu^4}\right)^{1/2}$ (Bonnor, 1956; Ebert, 1955) becomes low.

In Figure 2.9, we show the critical Bonnor–Ebert mass as a function of gas density and column similar to Krumholz et al. (2011), with the improvement that chemistry and temperature are calculated self-consistently. As noted by Krumholz et al. (2011), the contours of the 50% and 90% H_2 abundances are somewhat similar to those of the Bonnor–Ebert mass of the gas. However, we note that the Bonnor–Ebert mass near these contours is $M_{\rm BE} = 10^2 - 10^3\ M_\odot$, much larger than the mass of individual stars. In some regions, the Bonnor–Ebert mass is even larger than the available mass in the clouds: for example, at $n = 1000\mathrm{cm}^{-3}$ and $A_V = 1$, the total mass of the cloud $M \sim R^3 n m_{\rm H} \sim (N/n)^3 n m_{\rm H} \sim 5 M_\odot$, and is much smaller than the local Bonnor–Ebert mass $M_{\rm BE} \sim 100 M_\odot$. This suggests

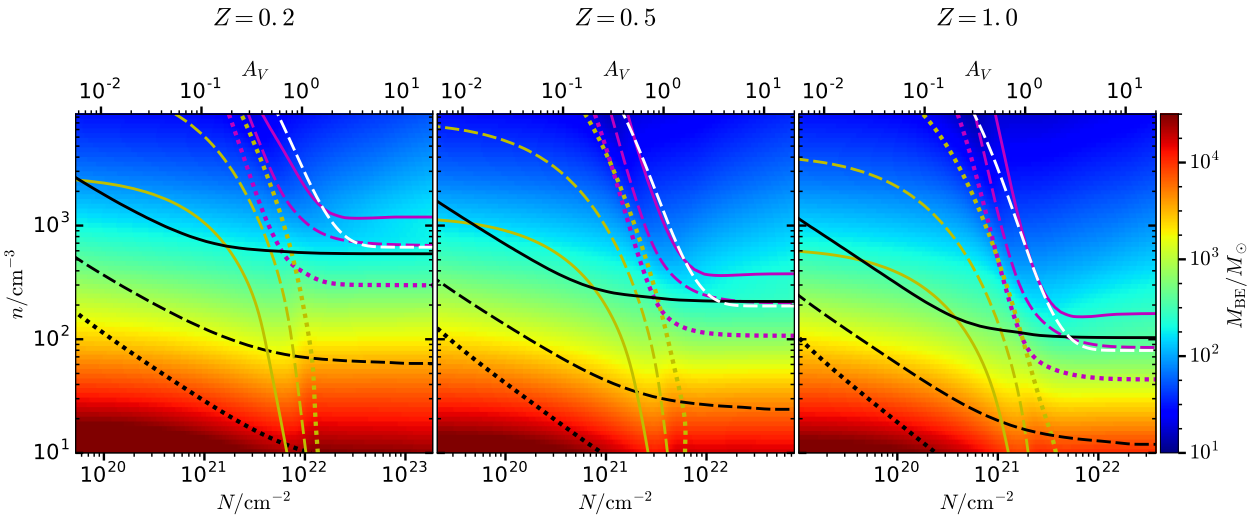


Figure 2.9: Similar to Figure 2.5, but for Bonnor–Ebert mass of the gas as a function of A_V (or N) and density n.

that the correlation of H_2 with star formation is not a sufficient pre-condition, but a fairly non-specific coincidence. To reach Bonnor–Ebert masses comparable to those of individual stars, much higher densities are needed than the densities required for high equilibrium H_2 abundance.[8]

2.3.5 Comparison with Observations of Diffuse and Translucent Clouds

The ultimate test for any chemistry model is the comparison with observations. The one-sided equilibrium slab models that we have used to test our network are extremely simple and cannot be expected to agree in detail with the chemical state in the real ISM, which is characterized by complex time-dependent dynamics and morphological structure, both the result of turbulence. Nevertheless, for illustrative purposes it is useful to compare the abundances obtained with our network (for idealized slab geometry) with the observed ISM abundances. To do so, we compiled observations of H_2, CO, C, C^+, CH_x, and OH_x abun-

[8]Also, as noted above, a small $t_{\mathrm{dyn}}/t_{\mathrm{H_2}}$ or $t_{\mathrm{diss}}/t_{\mathrm{sh}}$ may limit the H_2 abundance at low A_V and n. Non-equilibrium H_2 abundances may be high only in the upper-right corner of each panel, where $M_{\mathrm{BE}} < 100 M_\odot$.

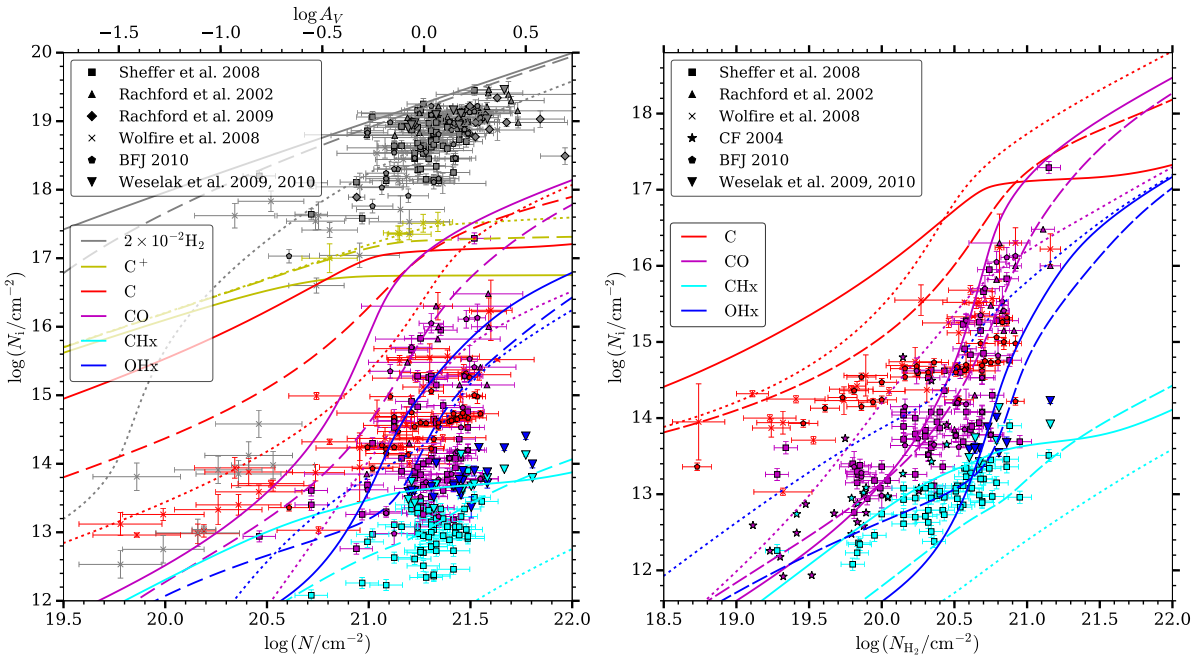


Figure 2.10: Comparison between observations and our one-sided slab model. The *left* panel plots the column density N_i of chemical species at a given cloud A_V (or N). The lines show the results from our slab model with $n = 10$ cm^{-3} (dotted), $n = 100$ cm^{-3} (dashed), and $n = 1000$ cm^{-3} (solid). Different markers plot the observed abundances from the literature. Different colors represent different species, as shown in the legends. The *right* panel is similar to the left panel, but with the H_2 column density on the x-axis instead.

dances in the literature derived from UV and optical absorption spectra along different sight lines: H_2, C, and C^+ observations compiled by Wolfire et al. (2008)[9]; H_2 and CO observations in Rachford et al. (2002) and Sheffer et al. (2008); H_2 observations in Rachford et al. (2009); H_2, C, and CO observations in Burgh et al. (2010) (hereafter BFJ2010); CH_x[10] abundance in Sheffer et al. (2008) and Crenny & Federman (2004) (hereafter CF2004); and OH_x[11] abundance in Weselak et al. (2009, 2010). The UV spectroscopy data in these observations mainly come from the *Far Ultraviolet Spectroscopic Explorer (FUSE)* , the Space Telescope Imaging Spectrograph (STIS) on board the *Hubble Space Telescope*, the *UVES* spectrograph at *European Southern Observatory (ESO)* and the *Copernicus* survey. The optical spectra

[9]In Wolfire et al. (2008), most of the C^+ values are upper limits. Here we only include the true measurements.

[10]$CH_x = CH + CH^+$ for Sheffer et al. (2008) and Crenny & Federman (2004).

[11]$OH_x = OH + OH^+$ for Weselak et al. (2009), and $OH_x = OH$ for Weselak et al. (2010).

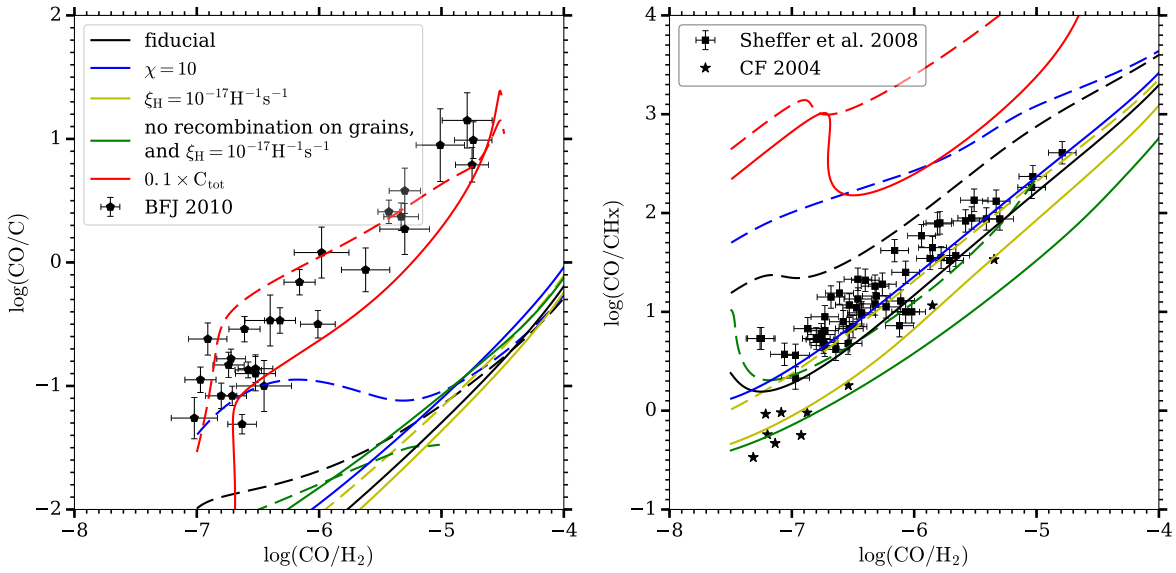


Figure 2.11: *Left panel:* abundances of CO/C vs. CO/H_2. The observational data are taken from BFJ2010, and lines of different colors show the results from different slab models (see legend), with $n = 100$ cm^{-3} (dashed), and $n = 1000$ cm^{-3} (solid). *Right panel*: similar to the left panel, but for CO/CH_x on the y-axis. The observed abundance is taken from Sheffer et al. (2008) and CF2004. See also Figure E.1 for a more detailed comparison between observations and our model with no grain-assisted recombination, and the depletion of carbon abundance.

data used to derive CH and CH^+ abundances in Sheffer et al. (2008) are obtained at the McDonald and European Southern Observatories. For most sightlines, the total column N is derived from reddening data using $N/E(B-V) = 5.8 \times 10^{21}$ H cm^{-2}mag^{-1} (Bohlin et al., 1978; Rachford et al., 2009), except for sight lines that have H abundances directly observed by Lyα absorption in Bohlin et al. (1978) (included in the compilation of observations by Wolfire et al. (2008)).

We construct a simple one-sided slab model with thermal and chemical equilibrium, as described in Section 2.3.1, to compare with the observational data. The fiducial model has $\chi = 1$, $\xi_H = 2 \times 10^{-16}$ s^{-1}H^{-1}, and constant densities of $n = 10$, 100, and 1000 cm^{-3}. We also explore the effects of varying different parameters such as χ, ξ_H, the efficiency of grain-assisted recombination, and gas-phase carbon abundance.

Figure 2.10 shows the comparison between the observations and our slab cloud model in column densities of H_2, CO, C, C^+ and CH_x and OH_x. For the H to H_2 transition in the left panel, low density $n \sim 10$ cm^{-2} is required to match equilibrium H_2 abundances with observations. This is consistent with the analysis by Bialy et al. (2015, 2017) on the H to H_2 transition layers in the Perseus molecular cloud and star forming region W43.[12]

Comparing the right panel with the left, there is much less dispersion in the observed C, CO, and CH_x abundances when plotted against the H_2 column density N_{H_2} instead of the total column N or A_V. This is likely due to foreground or background contaminations: low density atomic ISM is much more "diffuse" in spatial distribution than the relatively "clumpy" molecular ISM. Therefore, the low density atomic clouds may contribute a significant fraction of the total column/visual extinction in a given sight line, without contributing much to the total column of chemical species such as H_2, C, CO, CH_x and OH_x, which mainly form in higher density regions.

In spite of the extreme idealizations adopted, there is generally a good agreement between our model and the observations in Figure 2.10, especially in the right panel (when plotted against N_{H_2}): we can successfully reproduce the range of observed abundances of CO, CH_x and OH_x with densities between 100 cm^{-3} and 1000 cm^{-3}. It is especially remarkable that CO and CH_x abundances agree over one or two orders of magnitude of N_{H_2}.

However, there is one significant discrepancy between the simple model and observations: the predicted C abundance is too high at a given A_V or N_{H_2} by about an order of magnitude (see Figure 2.10). This is more clearly shown in the left panel of Figure 2.11 when plotted with the ratio of CO/C (see also Figure 4 in BFJ2010). To investigate the dependence of CO/C on model parameters, we vary the incident radiation field strength χ, cosmic-ray ionization rate ξ_H, the efficiency of grain-assisted recombination of ions, and the gas-phase carbon abundance. The summary of our results is shown in the left panel of Figure 2.11.

[12] $n \sim 10$ cm^{-2} is in fact lower than densities believed to be in the CNM ($n \sim 40$ cm^{-2} based on pressures from Jenkins & Tripp (2011) and temperatures from Heiles & Troland (2003)). If densities are indeed higher than $n \sim 10$ cm^{-2}, this means that the observed abundances are below equilibrium, potentially due to dynamical effects (as discussed previously in Section 2.3.1).

Variations in χ and $\xi_{\rm H}$ tend to change the C and CO abundances in the same direction, giving very a similar CO/C ratio to that of the fiducial model. Excluding the grain-assisted recombination of ions does not solve the problem either: it does lower the C abundance at a given A_V, but at the same time, the CO abundance is much lower as well, and the CO/C ratio is still too low (see also the left panel of Figure E.1).

Note that our conclusion is different from the conclusion in Liszt (2011), which stated that the absence of grain-assisted recombination can reproduce the high CO/C observed in BFJ2010. We believe this is because Liszt (2011) assumed a constant $x_{\rm HCO^+} \sim 3 \times 10^{-9}$ in their chemistry model. Without grain-assisted recombination, the HCO^+ abundance is much lower at $x_{\rm HCO^+} \lesssim 10^{-10}$, leading to much less efficient CO formation than calculated in Liszt (2011)[13].

The only variation of our models that can reproduce the observed CO/C ratio is the one with gas-phase carbon abundance depleted by an order of magnitude relative to the fiducial model, i.e. $\rm C_{tot}/H = 0.1(C_{tot}/H)_{fiducial} = 1.6 \times 10^{-5}$. This is also found in BFJ2010 (their Figure 4). However, although carbon depletion can be caused by formation of grains such as polycyclic aromatic hydrocarbons (PAHs), a depletion factor as extreme as 0.1 is unlikely. Even the most carbon-depleted sight lines observed in Sofia et al. (2011) and Parvathi et al. (2012) have $\rm C_{tot}/H > 6 \times 10^{-5}$ (derived from C^+ absorption measurements), and many of these sight lines are the same as in Burgh et al. (2010). Moreover, as shown in the right panel of Figure 2.11, the ratio of $\rm CO/CH_x$ in the model with carbon depletion is an order of magnitude higher than the observed values, whereas other models reproduce $\rm CO/CH_x$ consistent with observations. Therefore, we conclude that the depletion of gas-phase carbon is unlikely to be the solution for this problem.

Overpredicting C abundance is also an issue among other PDR models. For example, BFJ2010 compared their observations with the chemistry model by van Dishoeck & Black

[13]This is because without grain-assisted recombination, the electron abundance is higher. Electrons destroy H_3^+, which forms OH_x and subsequently HCO^+. CO is mainly formed by $\rm HCO^+ + e \rightarrow CO + H$. To be consistent with Liszt (2011), We also use a low cosmic-ray ionization rate $\xi_{\rm H} = 10^{-17}$ $\rm s^{-1}H^{-1}$, for the case without grain-assisted recombination.

(1988), and found very similar results. Glover et al. (2010) also predicted CO/C $\ll 1$ for $A_V < 2$ clouds with their extensive chemical network (see their Figures 1 and 2). Bensch et al. (2003) observed C and CO emission in the translucent cloud MCLD 123.5+24.9, and also found CO/C $\gtrsim 1$. They used the PDR code by Stoerzer et al. (1996) to model their observations, and found that their models also tend to produce a CO/C ratio that is too low, unless they assume a cloud structure of high density ($n \sim 10^4$ cm^{-3}) clumps embedded in a low density medium.

It is worth emphasizing that observations compiled here are all for $A_V \lesssim 1$ diffuse and translucent clouds, for which UV or optical absorption observations may be used. For these clouds, most carbon ($> 90\%$) is still in the form of C^+. The physical properties of these clouds are very different from GMCs and smaller dark molecular clouds, which typically has $A_V \gg 1$ and most carbon is in the form of CO.

There are some potential solutions to the mismatch of C abundance between equilibrium PDR models and observations. (1) Non-equilibrium chemistry. As previously noted, the photoionization and photodissociation timescales are generally short compared to collisional reactions or grain-assisted reactions (see Tables A.1 and A.2). Dynamical effects such as limited cloud lifetime and turbulent cycling of gas from a cloud's interior to its surface can lower the abundances of species formed in low-shielding regions such as C. Furthermore, C tends to form in less dense and shielded regions than CO, and can be more subject to these dynamical effects, which may bring its abundance far from equilibrium. (2) Improvement of chemical networks and reaction rates. It is possible that the chemical pathways to form C and CO in translucent clouds are not well understood, causing discrepancy between chemical models and observations. For example, the composition of dust grains and the rates for grain surface reactions are still uncertain. In addition, turbulent dissipation (Godard et al., 2014) might convert the dominant reservoir of carbon (in C^+) to CO without much production of C. In the future, 3D realistic ISM simulations with time-dependent chemistry will give us more insight into the role of non-equilibrium chemistry.

2.4 Summary

In this chapter, we propose a new lightweight and accurate chemical network for hydrogen and carbon chemistry in the atomic and molecular ISM. Our network is based on the NL99 network in Nelson & Langer (1999) and Glover & Clark (2012a), with significant modifications and extensions. We use 1D uniform slab models to compare our chemical network in detail with results from a full PDR code and also with the original NL99 network.

Our chemical network shows very good agreement with the much more sophisticated PDR code in the equilibrium abundances of all species. This agreement holds in a wide range of densities, visual extinctions, temperature, and metallicities, implying that our simplified network indeed captures the main chemical pathways. The NL99 network, however, performs poorly when comparing to the PDR code in detail. In particular, it significantly underproduces CO at $n \sim 100 - 500$ cm^{-3} when using the realistic cosmic-ray ionization rate $\xi_{\rm H} = 2 \times 10^{-16}$ s^{-1}H^{-1} (Indriolo et al., 2007; Hollenbach et al., 2012) in our galaxy. The NL99 network also fails to reproduce the abundances of other species such as C^+. With only one additional species and 19 additional reactions, our network has a comparable computational cost to the original NL99 network and proves to be much more accurate. Therefore, we conclude that our new network is preferred over the NL99 network for time-dependent numerical simulations of hydrogen and carbon chemistry, such as CO formation.

We apply our network to 1D models and obtain the equilibrium temperature and chemistry in a range of physical conditions, varying the density, incident radiation field strength, cosmic-ray ionization rate, and metallicity. We find that at metallicity $Z = 1$, the CO-dominated regime delimits the coldest gas and that the corresponding temperature tracks the cosmic-ray ionization rate in molecular clouds. We note, however, that it is primarily high density and high shielding that leads to low temperatures, rather than the CO abundance itself. In metal-poor gas with $Z \lesssim 0.2$, CO is difficult to form under typical diffuse-ISM conditions and may only be found in regions where gas density is significantly enhanced by

turbulence or gravity. We provide a simple fit for the locus of CO-dominated regions as a function of gas density, column, metallicity, and cosmic-ray ionization rate.

We also compiled observations of chemical species in diffuse and translucent clouds, and compared these with our chemistry model predictions, under the assumption of equilibrium. We are able to reproduce the observed CO, CH_x and OH_x abundances with density n between 100 cm^{-3} and 1000 cm^{-3}. However, the predicted C abundances are higher than the observed values by an order of magnitude. Previous equilibrium models have identified a similar difficulty matching C abundances, suggesting that time dependence or other more complex effects may be important. To fully understand the distribution of observed species in the ISM, detailed 3D simulations with realistic gas dynamics and non-equilibrium chemistry are required. We plan to pursue this in the future.

Chapter 3

The $X_{\rm CO}$ conversion factor from galactic disk ISM simulations

3.1 Method

To investigate the $X_{\rm CO}$ conversion factor in molecular clouds, we carry out MHD simulations of galactic disks, and post-process the results from MHD simulations with chemistry to obtain the distribution of molecular gas, including H_2 and CO. Then we use line radiation transfer code to model the CO emission from molecular clouds.

3.1.1 MHD Simulation

The MHD simulation is performed with the *TIGRESS* (Three-phase Interstellar medium in Galaxies Resolving Evolution with Star formation and Supernova feedback) framework introduced by Kim & Ostriker (2016, hereafter KO2016). Here we briefly describe the key physics in the simulations, and refer the readers to KO2016 for more extensive descriptions.

The *TIGRESS* simulations model a kpc-sized region of a galactic disk where the turbulent, multiphase, magnetized ISM is self-consistently modeled with resolved star formation and feedback. The physics are implemented within the *Athena* code (Stone et al., 2008). The

ideal MHD equations are solved in a vertically-stratified local shearing box (e.g. Stone & Gardiner, 2010). Self-gravity from gas and young stars are included by solving the Poisson's equation, as well as a fixed vertical gravitational potential representing the old stellar disk and the dark matter halo. Sink particles are implemented to represent star clusters, and feedback from massive stars are included based on a population synthesis model (STARBURST99 Leitherer et al., 1999). Both supernovae in star clusters and from runaway OB stars are included. The radiative heating and cooling of the gas are assumed to be optically thin. The heating comes from the photo-electric effect on dust grains, and the heating rate is time dependent and scales with the instantaneous FUV luminosity of the star cluster particles. The cooling rate is obtained from the local gas density and temperature using a simple cooling function appropriate for the ionized and atomic ISM (combination of Sutherland & Dopita (1993) and Koyama & Inutsuka (2002)).

The simulations self-consistently generate turbulent and magnetized three-phase ISM. In the fiducial model with solar neighborhood parameters, much of the volume is occupied by hot ionized gas, and most of the mass near the midplane is in the warm and cold neutral medium (WNM and CNM), similar to the observed ISM in the Milky Way and nearby galaxies. Although molecular gas is not explicitly modeled in the *TIGRESS* simulations, large structures of dense gas naturally develop, and in reality molecular gas would form within the regions of the CNM where the gas is dense and shielded. We model the formation of molecular gas by post-processing the *TIGRESS* simulations with chemistry and shielding, which is described in detail in Section 3.1.2.

We adopt the fiducial solar neighborhood model of KO2016. The simulation domain size is $L_x = L_y = 1024$ pc and $L_z = 4096$ pc. The initial gas surface density $\Sigma = 13\ M_\odot \mathrm{pc}^{-2}$. The simulation reaches a quasi-steady state after $t \approx 200$ Myr. The total mass of the gas in the simulation slowly declines as the gas turns into stars or leaves the simulation domain as galactic winds. In this work, we focus on the simulation during the time frame

$t = 350 - 420$ Myr when the surface density of the gas is in the range $9\ M_\odot \mathrm{pc}^{-2} < \Sigma < 10\ M_\odot \mathrm{pc}^{-2}$.

In order to study the effect of numerical resolution on $X_{\rm CO}$, we consider the simulation with three different resolutions: $\Delta x = 4$, 2, and 1 pc. The 4 pc simulation starts from $t = 0$ with the initial condition described in KO2016, and runs until $t = 700$ Myr. To save computational time, we use an "extraction" method to refine the resolution. We use the output of the 4 pc simulation at time $t = 350$ Myr as the initial condition of the 2 pc simulation, and run that for 70 Myr (until $t = 420$ Myr). Similarly, we use the output of the 2 pc simulation at $t = 378$ Myr as the initial condition of the 1 pc simulation, and run that for 4 Myr (until $t = 382$ Myr). We also reduce the domain size in the z-direction to $L_z = 2240$ pc for the 2 pc simulation and to $L_z = 896$ pc for the 1 pc simulation. Because the scale-hight $H \sim 100$ pc for the CNM and $H \sim 400$ pc for the WNM, the simulation domain in the z-direction is big enough to capture most of the mass in the neutral and molecular ISM. When refining from a coarser resolution, it takes some time for the turbulence to cascade down to smaller scales and create finer structures. The line-width size relation (Larson, 1981; Solomon et al., 1987; Heyer & Brunt, 2004; Heyer & Dame, 2015, e.g.),

$$v(l) \sim 0.7\ \mathrm{km/s}\ \left(\frac{l}{\mathrm{pc}}\right)^{1/2}, \tag{3.1}$$

gives the timescale for turbulent cascade:

$$t_{\rm turb}(l) = \frac{l}{v(l)} = 1.4\ \mathrm{Myr}\ (l/\mathrm{pc})^{1/2}. \tag{3.2}$$

We only use the outputs from the 2 pc and 1 pc simulations $4 - 6$ Myr after the extraction from coarser resolution, allowing sufficient time for the turbulence to develop at the refined resolution. The density threshold for sink particle creation, $n_{\rm thr}$, also depends on

the resolution of the simulation, and $n_{\rm thr}$ = 304, 927, and 2956 cm^{-3} for 1, 2 and 4 pc resolutions.[1]

3.1.2 Post-processing chemistry

To model the chemical composition of the gas, we have developed a post-processing module within the code *Athena++* (White et al., 2016). This module reads the output from *TIGRESS* simulations and performs chemistry calculations assuming the density and velocity in each grid cell is fixed. We use the simplified chemical network of Gong et al. (2017), which focuses on the hydrogen, carbon and oxygen chemistry, and gives accurate abundances of H_2 and CO. We assume an initial chemical composition of neutral atomic gas, with all hydrogen in the form of H, all carbon in C, all oxygen in O, and all silicon in Si. The initial temperature is the same as the output from MHD simulations. Then we evolve the chemistry, temperature, and radiation field (see below) for time $t_{\rm chem}$ = 50 Myr, so that the chemical state of the gas reaches equilibrium. In other words, we do not self-consistently calculate the gas dynamics and non-equilibrium chemistry, but instead consider the state in which the chemistry is in equilibrium and determined by the ISM structure from the MHD simulations. Because gas cooling is not sensitive to the chemical composition, chemistry has minimal effect on the gas dynamics (Glover & Clark, 2012b; Gong et al., 2017). However, dust shielding can reduce the gas heating, and lower the gas temperature by a factor of ~ 2 in shielded regions of the CNM where molecular gas forms. In return, gas dynamics can also influence the chemical composition. For example, the timescale for H_2 formation can be longer than the turbulent crossing time in the molecular clouds, which may lead to much lower H_2 abundance than the equilibrium values (Gong et al., 2017). Non-equilibrium chemistry and temporal dependences are considered in Section 3.2.2.

[1]This is assuming the heating rate of the CNM to be the solar neighborhood value $\Gamma = \Gamma_0 = 2 \times 10^{-26}$ erg s^{-1} (KO2016 Equation (8)). However, $n_{\rm thr}$ is insensitive to the change of Γ: $n_{\rm thr}$ increases by less then a factor of two when Γ increases by a factor of ten.

The heating and cooling of the gas is calculated simultaneously with chemistry, with the details described in Gong et al. (2017). We slightly modify the parameter $\tilde{N}(\mathrm{CO})$ for CO cooling in Gong et al. (2017) by setting

$$\tilde{N}(\mathrm{CO}) = \frac{n(\mathrm{CO})}{\max\left(\langle|\mathrm{d}v/\mathrm{d}r|\rangle, v_{\mathrm{th}}/l_{\mathrm{esc}}\right)}, \tag{3.3}$$

where $\langle|\mathrm{d}v/\mathrm{d}r|\rangle$ is the mean (absolute) velocity gradient across the six faces of each grid cell in the simulation, $v_{\mathrm{th}} = \sqrt{2kT/m(\mathrm{CO})}$ the thermal velocity of CO molecules, and $l_{\mathrm{esc}} = 100$ pc the maximum length scale for a photon to escape. Using the maximum of two terms in the denominator of Equation (3.3) ensures that there is a minimum probability for the photon to escape when the local velocity gradient is small, given a maximal molecular cloud size, $\lesssim 100$ pc. This formalism is consistent with the large velocity gradient (LVG) and escape probability approximation we adopted in carrying out the synthetic observations of CO line emission (Section 3.1.3).

In order to compute the photoionization and photodissociation rates in the chemistry network, a radiation transfer scheme is needed to calculate the reduction of FUV radiation by dust and molecule shielding. We use the six-ray approximation (Nelson & Langer, 1997, 1999; Glover & Mac Low, 2007): in each cell, the radiation field is calculated by ray-tracing and averaged over six directions along the Cartesian axes. The incident radiation field is assumed to come from the edge of the computational domain along each ray, and has the initial intensity the same as that in the MHD simulations (the MHD simulations do not include shielding itself). The main advantage of this approach is the low computational cost. When comparing to ray-tracing along many more different angles, six-ray approximation gives reasonably accurate results (Safranek-Shrader et al., 2017). Because chemistry and radiation depend on each other, we iterate to solve the chemistry equations and six-ray radiation transfer.

3.1.3 Synthetic Observation of CO Line Emission

To model the CO($J = 1-0$) line emission, we apply the publicly available radiation transfer code *RADMC-3D* (Dullemond et al., 2012) with chemistry and temperature obtained as described in Section 3.1.2.[2] We select the mid-plane region $|z| < 256$ pc, where almost all molecules are found. H_2 is assumed to be the only collisional partner with CO, and we use a fixed ortho-to-para ratio of 3:1.[3] The synthetic observations are performed along the z-axis, i.e., the observer is looking at the galaxy face-on. This avoids cloud blending, as all molecular clouds form near the mid-plane of the galactic disk.

The CO population levels are calculated by using the LVG and escape probability approximation, which is implemented in *RADMC-3D* by Shetty et al. (2011a). This approximation allows the population levels to be calculated locally in each cell. The escape probability is

$$\beta = \frac{1 - \mathrm{e}^{-\tau}}{\tau}, \tag{3.4}$$

and the optical depth $\tau = \min(\tau_{\rm LVG}, \tau_{\rm EscProb})$. The LVG approximation gives

$$\tau_{\rm LVG} = \frac{\lambda_{10}^3}{8\pi} \frac{A_{10} n_{\rm CO}}{\langle |\mathrm{d}v/\mathrm{d}r| \rangle} f_1 \left(\frac{f_0/g_0}{f_1/g_1} - 1 \right), \tag{3.5}$$

Where A_{10} is the Einstein A coefficient $A_{10} = 7.203 \times 10^{-8}$ s^{-1}, $n_{\rm CO}$ the number density of CO molecules, $g_0 = 1$ and $g_1 = 3$ the degeneracy for $J = 0$ and $J = 1$ levels, $f_0 = n_0/n_{\rm CO}$ and $f_1 = n_1/n_{\rm CO}$ the fraction of CO molecules in $J = 0$ and $J = 0$ levels, where n_0 and n_1 are the level populations, $\langle |\mathrm{d}v/\mathrm{d}r| \rangle$ the same as that in Equation (3.3). The optical depth

[2]We set a temperature ceiling of $T = 200$ K for the temperature input, because CO only forms within the CNM where $T \lesssim 100$ K, and a high temperature input from the WNM and hot gas introduces additional computational cost for calculating the CO population levels in regions where the CO abundance is essentially zero. We have tested using a higher temperature ceiling of 1000 K and confirmed that it gives the same result.

[3]The collisional coefficients for ortho- and para- H_2 are very similar, and we have tested that a ortho-to-para ratio of 1:1 gives very similar results.

from escape probability approximation (Draine, 2011),

$$\tau_{\rm EscProb} = \frac{h n_{\rm CO} L_{\rm EscProb}}{\sqrt{\pi} v_{\rm tot}} (f_0 B_{01} - f_1 B_{10}), \tag{3.6}$$

is set by a typical length-scale $L_{\rm EscProb}$, where B_{01} and B_{10} are the Einstein B coefficients, and $v_{\rm tot}$ is the total velocity dispersion (see below). We adopt $L_{\rm EscProb} = 100$ pc, consistent with the CO line cooling in Equation (3.3). In our simulation, the velocity gradient is usually relatively large, and in most cells $\tau = \tau_{\rm LVG}$.

Ray-tracing is performed after the CO level populations are obtained. In general, the emission line intensity is determined by radiative transfer (e.g. Draine, 2011):

$$\mathrm{d}I_\nu = -I_\nu \mathrm{d}\tau_\nu + S_\nu \mathrm{d}\tau_\nu, \tag{3.7}$$

where I_ν is the line intensity at frequency ν, S_ν the source function, and τ_ν the optical depth. τ_ν depends on the line profile, which is set by the velocity dispersion $v_{\rm tot} = \sqrt{v_{\rm th} + v_{\rm turb}}$. We include a sub-grid "micro-turbulent" velocity dispersion according to the line-width size relation (Equation (3.1)),

$$v_{\rm turb} = 0.7 \text{ km/s } \left(\frac{\Delta x}{\rm pc}\right)^{1/2}, \tag{3.8}$$

where Δx is the resolution of the simulation. We also include a background blackbody radiation field with temperature $T_{\rm CMB} = 2.73$ K from the cosmic microwave background (CMB).

We run *RADMC-3D* with a passband from -20 km/s to 20 km/s (wide enough to include all CO emission) and velocity resolution of 0.5 km/s. RADMC-3D produces spectral position-position-velocity (PPV) cubes of the CO($J = 1 - 0$) line. We then interpolate I_ν to a finer velocity resolution of 0.07 km/s, and calculate the total CO($J = 1 - 0$) line intensity in each observed pixel, $W_{\rm CO}$, by integrating I_ν over all velocity channels that have emission above the detection limit, $T_{\rm det} = 0.4$ K. This approach matches the typical velocity resolution

and sensitivity in observations of nearby molecular clouds (e.g. Ridge et al., 2006; Pineda et al., 2008, 2010; Ripple et al., 2013; Lee et al., 2014a, , see also Table 3.1). We define the "CO-bright" region as pixels with $W_{\rm CO} > 0.1$ km/s, and calculate $X_{\rm CO}$ for each pixel in the CO-bright region. The average $X_{\rm CO}$, $\langle X_{\rm CO} \rangle = \sum N_{\rm H_2} / \sum W_{\rm CO}$ is also calculated only within the CO-bright region, similar to the common approach in observations (e.g. Pineda et al., 2008; Ripple et al., 2013). We define the fraction of CO-dark H_2,

$$f_{\rm dark} \equiv \frac{M_{\rm H_2}(W_{\rm CO} < 0.1 \text{ K km s}^{-1})}{M_{\rm H_2,tot}}. \tag{3.9}$$

3.1.4 The beam size in synthetic observations

The default beam size in our synthetic observations is the same as the numerical resolution in the MHD simulations. In real observations, the beam size (in physical units) varies depending on the telescope and the distance of the object. The dust extinction or emission map used to derive H_2 column densities typically has coarser resolution than the CO map. To analyze the $X_{\rm CO}$ values, the dust map and CO map are smoothed to a common resolution (usually the resolution of the dust map), which we refer to as the "beam size".[4] The velocity resolution and sensitivity also vary in observations. We have compiled the observational parameters from the literature of $X_{\rm CO}$ observations in the Milky Way and nearby galaxies in Table 3.1. All the observations listed used H_2 mass estimation from dust extinction or emission. We also list $\langle X_{\rm CO} \rangle$ obtained by the observations when available.

[4]Note that this is often called "pixel size" in observations. We use "beam size" to distinguish from the "pixel size" determined by the numerical resolution of our simulation and synthetic radiative transfer grid.

Table 3.1: Observational parameters in selected $X_{\rm CO}$ literature

reference	beam size	CO map res.	distance[a]	object	velocity res. (km/s)	$T_{\rm det}$(K)[b]	$\langle X_{\rm CO}\rangle_{20}$
Ripple et al. (2013)	0.2 pc	0.1 pc	420 pc	Orion	0.2	2	1.4
Lee et al. (2014b)	0.36 pc	0.06 pc	280 pc	Perseus	0.064	0.8	0.3[c]
Pineda et al. (2008)	0.4 pc	0.06 pc	280 pc	Perseus	0.064	0.35	2 ± 1
Leroy et al. (2011)	60 pc	5.8 pc	50 kpc	LMC	0.1	0.35	3.0
Leroy et al. (2016)	60 pc	11-60 pc	0.05-21.5 Mpc	nearby galaxies[d]	1.6-5	0.03-0.2	–
Smith et al. (2012)	140 pc	90 pc	780 kpc	M31	2.6	0.03	1.9 ± 0.4
Sandstrom et al. (2013)[e]	0.6-4 kpc	0.2-1.2 kpc	3.6-21.4 Mpc	spiral galaxies	2.6	0.02-0.04	$1.4 - 1.8$[f]

[a] Distance of Perseus and Orion molecular clouds are taken from Schlafly et al. (2014).

[b] Detection limit for CO($J = 1 - 0$) line emission. Same as the mean RMS noise per velocity channel in observations.

[c] Note that the $\langle X_{\rm CO}\rangle$ in Lee et al. (2014b) is smaller than that determined by Pineda et al. (2008). Lee et al. (2014b) states that the discrepancy mainly results from different adopted dust-to-gas ratio and the consideration of HI gas.

[d] Antennae, LMC, M31, M33, M51, and M74.

[e] Observations used the CO($J = 2 - 1$) line and assumed a fixed line ratio (2-1)/(1-0)=0.7.

[f] This is the average $\langle X_{\rm CO}\rangle$ in low-inclination galaxies. The dispersion is about 0.3 dex.

We investigate the effect of beam size on $X_{\rm CO}$ in Section 3.2.4. The adopted parameters and beam sizes are listed in Table 3.2, which is designed to match the typical observational parameters listed in Table 3.1. The synthetic observations with default beam size are based on the original model data (the same as the numerical resolution). To create synthetic maps with larger effective beam, we first smooth out the PPV cubes produced by RADMC-3D to the desired CO map resolution. Then we match the corresponding velocity resolution from the default 0.5 km/s in the PPV cubes, by either interpolating to finer or integrating to coarser velocity resolution. We integrate over all velocity channels with emission above the detection limit $T_{\rm det}$ and obtain a 2D map of $W_{\rm CO}$ at the corresponding CO map resolution. Then both the map for $A_V(N_{\rm H_2})$ and the map for $W_{\rm CO}$ are smoothed to the common resolution of the beam size, for which $X_{\rm CO}$ is calculated. We note that the "beam" is square, not circular. The CO-bright region, for which $\langle X_{\rm CO}\rangle$ is calculated, is defined as pixels with $W_{\rm CO} > 3T_{\rm det}\Delta v$, where Δv is the width of the velocity channel.

Table 3.2: Parameters for synthetic observations

beam size(pc)	CO map res.(pc)	velocity res.(kms)	$T_{\rm det}$(K)
1	1	0.07	0.4
2	2	0.07	0.4
4	2	0.07	0.4
8	2	0.07	0.4
16	2	0.07	0.4
32	2	0.07	0.4
64	4	0.1	0.35
128	64	2.6	0.03
512	128	2.6	0.03
1024	256	2.6	0.03

3.1.5 Model parameters

We consider three sets of models designed to study different conditions that may affect $X_{\rm CO}$: the numerical resolution, non-equilibrium chemistry, and variation in the galactic environment (ISM structure and ambient radiation field). The parameters for our models are sum-

marized in Table 3.3. Model names denote changes in numerical resolution (RES-1pc, etc.), chemical evolution time (TCHEM-5Myr, etc.), and simulation snapshot time (T-356Myr, etc.). Note that t is the time for the MHD simulation, and $t_{\rm chem}$ is the time for the post-processing chemistry, as detailed in Section 3.1.2. RES-1pc and TCHEM-50Myr are two names for the same model, used for clarity in different sections discussing the numerical resolution or non-equilibrium chemistry. To do a controlled study, we set the incident radiation field strength $\chi = 1$ (in Draine (1978) units, corresponding to $J_{\rm FUV} = 2.7\times10^{-3}$erg cm^{-2}s^{-1}) for all models that intercompare numerical resolution and non-equilibrium chemistry (model IDs starting with RES or TCHEM). In the set of models for studying the variation in galactic environments (model IDs starting with T), χ is obtained from the star cluster particles as described in KO2016.

Table 3.3: Model parameters

ID	Resolution (pc)	t (Myr)	$t_{\rm chem}$ (Myr)
Convergence of numerical resolution:			
RES-1pc	1	382	50
RES-2pc	2	382	50
RES-4pc	4	382	50
Non-equilibrium chemistry:			
TCHEM-5Myr	1	382	5
⋮			
TCHEM-50Myr	1	382	50
Variation in galactic environments:			
T-356Myr	2	356	50
⋮			
T-416Myr	2	416	50

3.2 Results

3.2.1 Convergence study: effects of numerical resolution

In this section, we investigate the effect of numerical resolution on both chemistry and $X_{\rm CO}$. An overview of the models RES-4pc, RES-2pc and RES-1pc is shown in Figure 3.1, and the

overall properties of the models are listed in Table 3.4. As the resolution increases, more small structures and dense gas forms in the simulations. The locations of molecular clouds are similar in all three models, but the small scale filamentary structures within the molecular clouds can only be resolved in RES-2pc and RES-1pc. As we shall show (Section 3.2.1), at least 2 pc resolution is needed to accurately determine the average $X_{\rm CO}$ in molecular clouds.

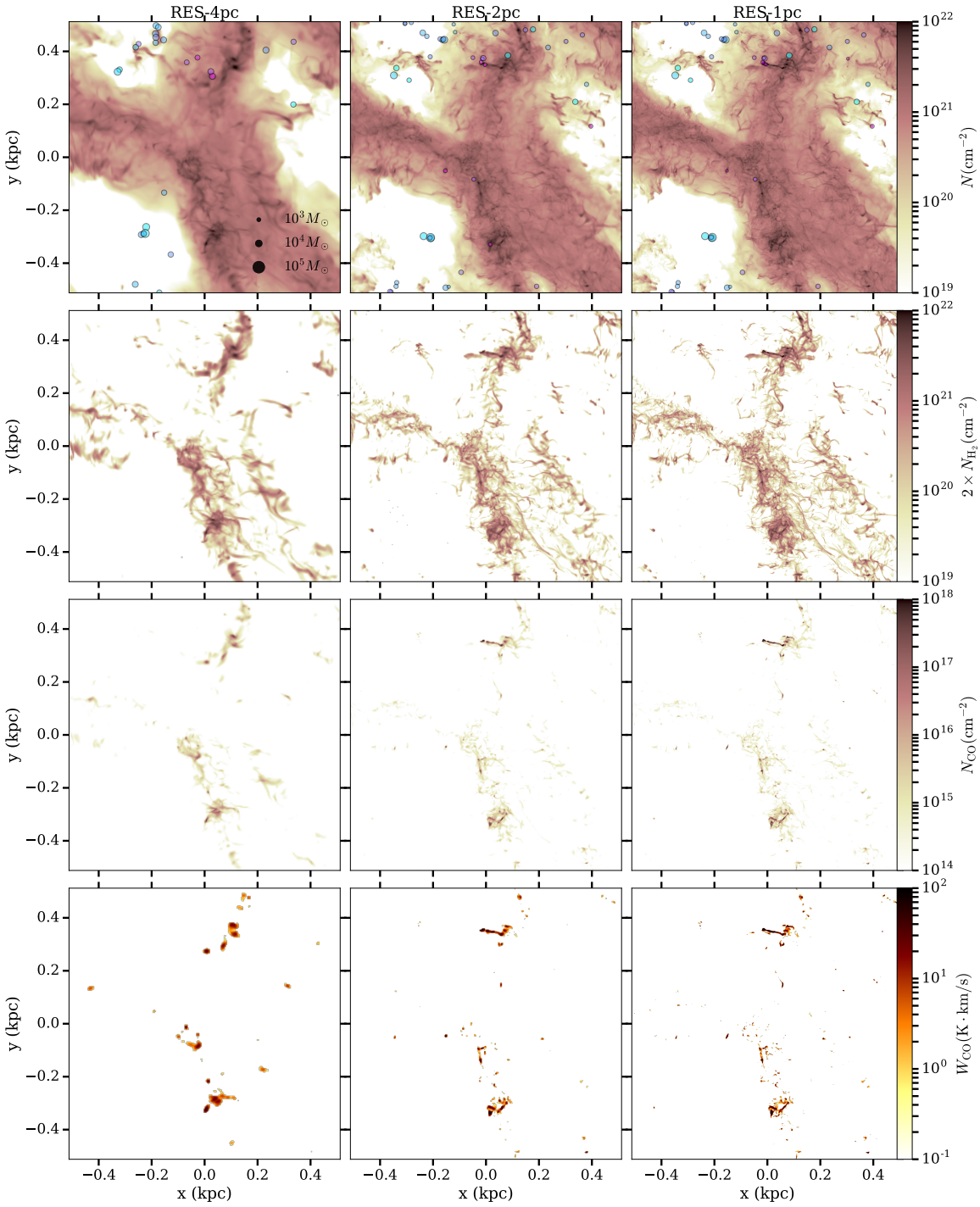


Figure 3.1: The column density of all gas (N, *first row*), molecular gas ($N_{\mathrm{H_2}}$, *second row*), CO (N_{CO}, *third row*), and the intensity of CO($J = 1 - 0$) line (W_{CO}, *last row*) in models RES-4pc, (*left*), RES-2pc (*middle*) and RES-1pc (*right*). The young (age < 40 Myr) star clusters/sink particles formed in the simulations are shown as filled circles in the first row with N. The area of the circles are proportional to the square root of the cluster masses, ranging from 10^3 $M_\odot$ to 10^5 $M_\odot$ (see legends in the top left panel), and the color of the circles indicates the cluster age, from 0 (magenta) to 40 Myr (blue).

Table 3.4: Overall properties of models for comparisons in numerical resolution and non-equilibrium chemistry

model ID	$M_{\rm tot}(M_\odot)$[a]	$M_{\rm H_2}(M_\odot)$	$M_{\rm CO}(M_\odot)$	$L_{\rm CO}$ (K km s^{-1}pc^2)[b]	$\langle X_{\rm CO}\rangle_{20}$[c]	$f_{\rm dark}$[d]	f_{100}[e]	$2\langle f_{\rm H_2}\rangle$[f]
RES-4pc	7.48×10^6	5.76×10^5	4.82×10^1	7.63×10^4	1.45	69%	0.4%	11%
RES-2pc	7.41×10^6	5.55×10^5	5.49×10^1	8.27×10^4	1.07	75%	0.9%	10%
RES-1pc (TCHEM-50Myr)	7.41×10^6	6.89×10^5	1.21×10^2	1.22×10^5	1.02	71%	2.3%	13%
TCHEM-5Myr	7.41×10^6	2.46×10^5	8.96×10^1	9.06×10^4	0.56	67%	2.3%	5%

[a] Total mass $M_{\rm tot} = 1.4 m_{\rm H}\int n{\rm d}V$. The factor 1.4 is from the helium abundance $f_{\rm He} = 0.1$.

[b] Total luminosity of CO($J = 1-0$) line.

[c] Average $X_{\rm CO}$ in CO-bright regions. $\langle X_{\rm CO}\rangle_{20} = \langle X_{\rm CO}\rangle/(10^{20}{\rm cm^{-2}K^{-1}km^{-1}s})$.

[d] CO-dark H_2 gas fraction (see Equation (3.9)).

[e] Fraction of mass with density $n > 100$ cm^{-3}.

[f] Fraction of hydrogen in H_2: $2\langle f_{\rm H_2}\rangle = M_{\rm H_2}/(M_{\rm H_2} + M_{\rm H})$.

Molecular Abundances and Dependence of Chemistry on numerical resolution

As the numerical resolution increases from 4 pc to 1 pc, a larger fraction of mass in the simulations is in the dense gas. This is quantified by the increase of f_{100} (the fraction of gas with density $n > 100$ cm^{-3}) with resolution in Table 3.4, and the density distributions in Figure 3.2. The density distributions are similar at low densities where the gas is well resolved. At high densities, the distribution cuts off near the density threshold for sink particle creation, where the unresolved dense gas is converted into sink particles in the simulations. As resolution increases, the density threshold for sink particle creation also increases, allowing denser gas to form.

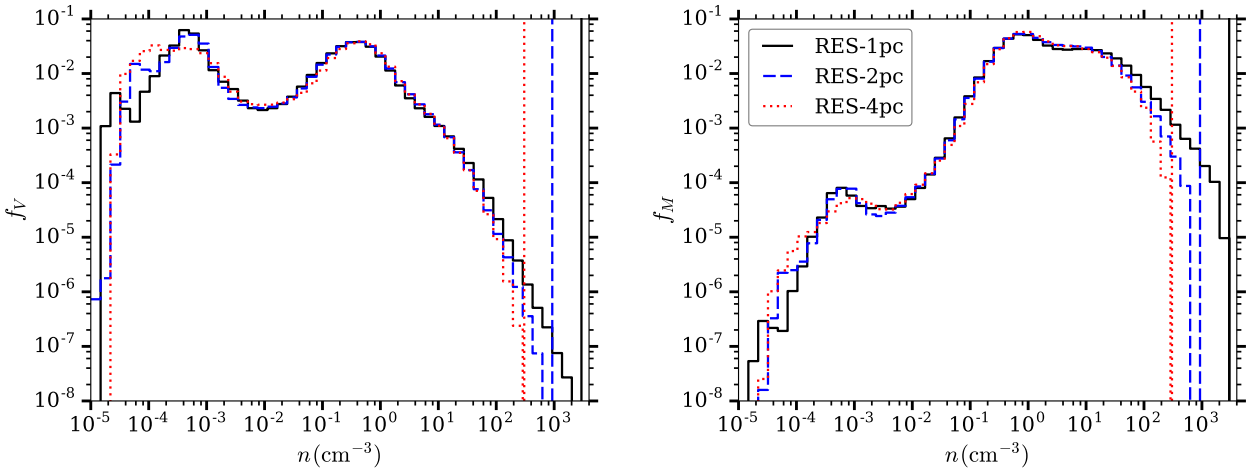


Figure 3.2: Histograms of volume-weighted (*left*) and mass-weighted (*right*) density n in models RES-1pc (solid black), RES-2pc (dashed blue) and RES-4pc (dotted red). The y-axes is normalized to show the fraction of volume f_V or mass f_M in each density bin. The vertical lines indicate the density threshold for sink particle creation at the corresponding resolution in each model (Section 3.1.1).

The change of density distribution with resolution affects the chemical compositions of the gas. As the resolution increases from 4 pc to 1 pc, the total H_2 mass stays nearly constant, but the total CO mass increases by a factor of nearly 3 (Table 3.4). The reason for this is evident in Figure 3.3: most H_2 forms in the density range of $n = 10 - 100$ cm^{-3}, which is already well resolved with 4 pc resolution. However, most CO forms at $n \gtrsim 200$ cm^{-3}, which is not well resolved with 2 pc, maybe even 1 pc resolution. Using adaptive mesh refinement

(AMR) models, Seifried et al. (2017) found a resolution of ~ 0.2 pc is needed for the CO abundance to converge.

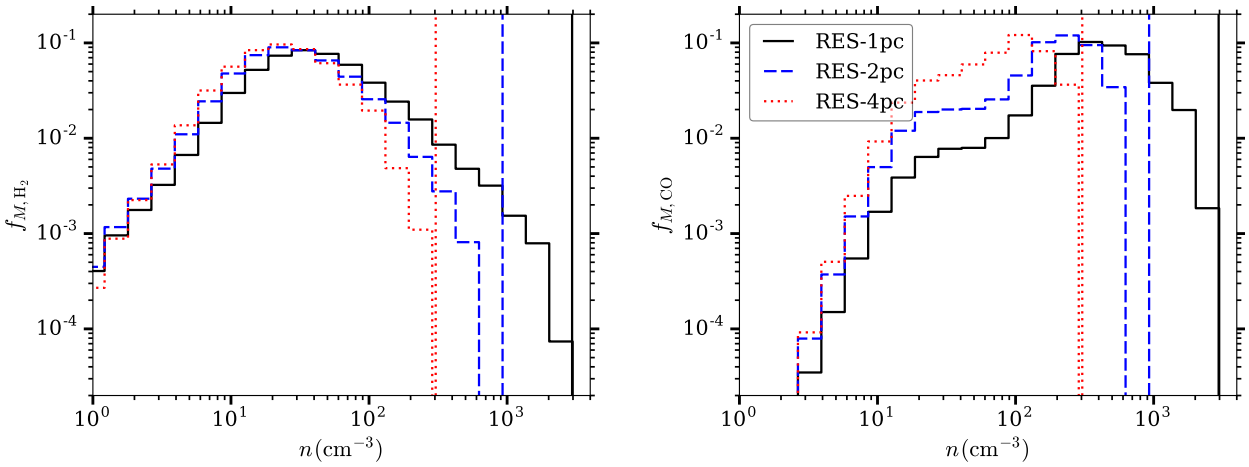


Figure 3.3: Histograms of density, similar to Figure 3.2, but weighed by H_2 mass (*left*) and CO mass (*right*) in each cell.

The chemical composition depends not only on density, which affects the rate of collisional reactions, but also on shielding, which determines the photodissociation rate by FUV photons. Which factor, density or shielding, is more important in determining the H_2 and CO abundances in realistic molecular clouds with complex structures? Figures 3.4 and 3.5 plot the H_2 and CO abundances versus density and shielding in each grid cell. We quantify the amount of shielding by calculating the effective extinction for the photo-electric heating (Gong et al., 2017),

$$\chi_{\rm PE} \equiv \chi \exp(-1.8 A_{V,\rm eff}), \tag{3.10}$$

where $\chi_{\rm PE}$ is the actual radiation field intensity obtained from the six-ray radiation transfer.

As shown in Figure 3.4, the H_2 abundance has a much tighter correlation with density than with shielding. This is because H_2 self-shielding is so efficient that the photodissociation rate of H_2 is very small in most regions that have a significant amount of H_2. The H_2 abundance is then determined by the balance between H_2 formation on dust grains,

$$\mathrm{H} + \mathrm{H} + \mathrm{gr} \rightarrow \mathrm{H_2} + \mathrm{gr}, \tag{3.11}$$

with a rate coefficient $k_{\rm gr} = 3.0 \times 10^{-17}$ cm^{3}s^{-1} (assuming solar neighborhood dust abundance), H_2 formation by H_3^+,

$$H_3^+ + e \rightarrow H_2 + H, \tag{3.12}$$

with a rate coefficient $k_{3.12}$, H_2 destruction by cosmic-rays,

$$CR + H_2 \rightarrow H_2^+ + e, \tag{3.13}$$

with a rate coefficient $k_{\rm CR} = 2\xi_{\rm H}(2.3f_{\rm H_2} + 1.5f_{\rm H})$, and H_2 destruction by H_2^+,

$$H_2^+ + H_2 \rightarrow H_3^+ + H, \tag{3.14}$$

with a rate coefficient $k_{3.14}$. Reactions (3.13) and (3.14) are also the main pathways for H_2^+ destruction and creation. Equilibrium of H_2^+ requires

$$f_{\rm H_2} k_{\rm CR} = f_{\rm H_2^+} f_{\rm H_2} n k_{3.14}. \tag{3.15}$$

H_3^+ is mainly created by reaction (3.14), and destroyed by reaction $H_3^+ + e$, which forms $H_2 + H$ (reaction (3.12)) or 3H with a branching ratio of 0.35:0.65. Equilibrium of H_3^+ requires

$$f_{\rm H_2^+} f_{\rm H_2} n k_{3.14} = \frac{1}{0.35} f_{\rm H_3^+} f_{\rm e} n k_{3.12}. \tag{3.16}$$

Finally, equilibrium of H_2 (Equations (3.11) - (3.16)) requires

$$\begin{aligned} f_{\rm H} n k_{\rm gr} + f_{\rm H_3^+} f_{\rm e} n k_{3.12} &= f_{\rm H_2} k_{\rm CR} + f_{\rm H_2^+} f_{\rm H_2} n k_{3.14} \\ f_{\rm H} n k_{\rm gr} + 0.35 f_{\rm H_2^+} f_{\rm H_2} n k_{3.14} &= f_{\rm H_2} k_{\rm CR} + f_{\rm H_2^+} f_{\rm H_2} n k_{3.14} \\ f_{\rm H} n k_{\rm gr} &= 1.65 f_{\rm H_2} k_{\rm CR}. \end{aligned} \tag{3.17}$$

In the above, each f is the abundance of a given species relative to hydrogen nuclei.

Equation (3.17) can be solved with the conservation of hydrogen nuclei $f_{\rm H} + 2f_{\rm H_2} = 1$, giving the equilibrium H_2 abundance as a function of n, plotted as the black dashed line in the left panel of Figure 3.4. This agrees very well with the upper limit of $f_{\rm H_2}$ in the simulations. The spread of $f_{\rm H_2}$ at a given density is due to the incomplete shielding of FUV radiation in some regions where destruction of H_2 from photodissociation brings its abundance lower than that in completely shielded regions. This can also be seen in the right panel of Figure 3.4: there is a large spread of $A_{V,\rm eff}$ at a given $f_{\rm H_2}$, and there are many grid cells with $A_{V,\rm eff} < 1$ and significant H_2 abundance.

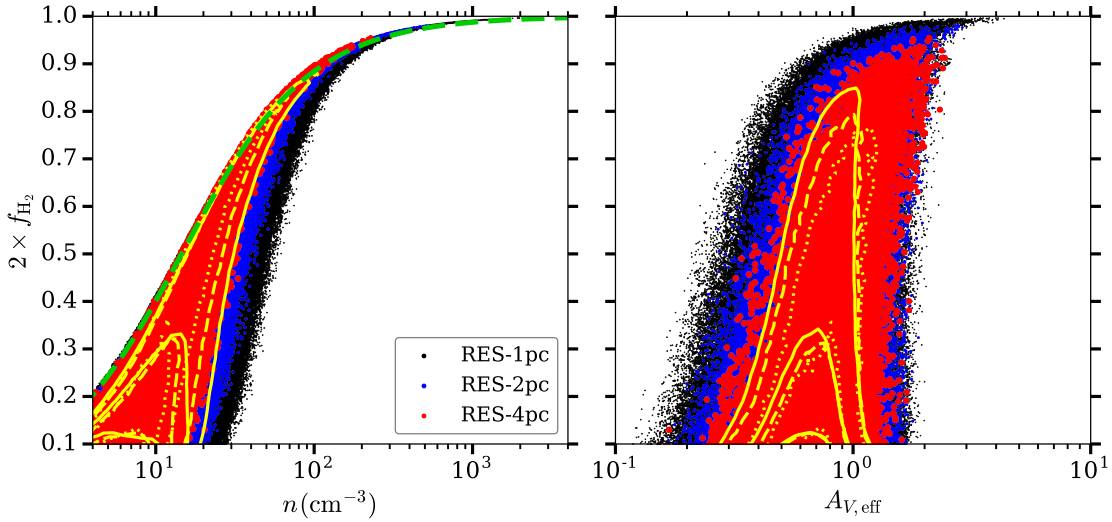


Figure 3.4: Scatter plot of the H_2 abundance $f_{\rm H_2}$ versus the gas density n (*left*) and the effective extinction $A_{V,\rm eff}$ (*right*), for models RES-1pc (black), RES-2pc (blue) and RES-4pc (red). Each point is one grid cell in the simulations, and the area of each point is proportional to the volume of the grid cell for the corresponding resolutions. The yellow contours show the surface densities of the points above which 10%, 50% and 90% of points lie, for models RES-1pc (solid), RES-2pc (dashed) and RES-4pc (dotted). The black dashed line shows the equilibrium H_2 abundance assuming the FUV radiation is completely shielded (Equation (3.17)).

Contrary to the case of H_2 abundance, which is determined mostly by density, the CO abundance is determined mostly by shielding, as shown in Figure 3.5. This is because the self-shielding of CO and cross-sheilding of CO by H_2 are much less efficient than the H_2 self-shielding. As a result, CO formation is limited by photodissociation, and CO can only form in regions with $A_{V,\rm eff} \gtrsim 1$ where the FUV radiation field is sufficiently shielded by dust.

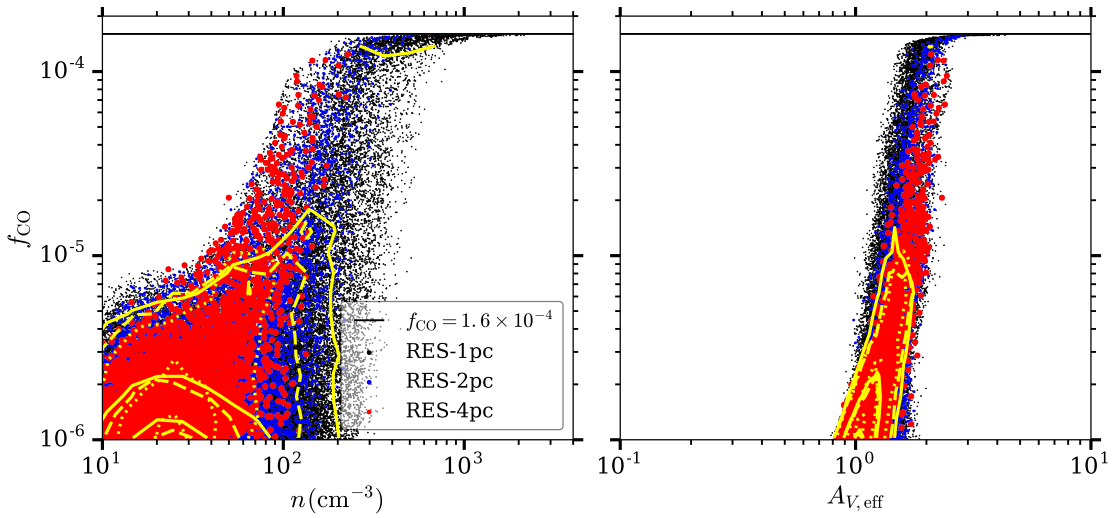


Figure 3.5: Similar to Figure 3.4, but for the CO abundance $f_{\rm CO}$. The black solid lines show where all carbon is in CO, i.e., $f_{\rm CO} = 1.6 \times 10^{-4}$.

Because H_2 and CO formation require different conditions, CO is only a very approximate tracer of H_2. Figure 3.6 shows the distribution of density n versus the effective extinction $A_{V,\rm eff}$ for each grid cell. At a given density, there is a large range of $A_{V,\rm eff}$. We roughly delineate loci where H, H_2, and CO form: H_2 exists in high density regions, and $f_{H_2} > 0.5$ corresponds roughly to densities $n \gtrsim 20$ cm^{-3}. CO forms in well shielded regions, and $f_{\rm CO} > 10^{-5}$ roughly corresponds to $A_{V,\rm eff} \gtrsim 1.4$. Because there are many grid cells with relatively high density but low effective extinction, a significant fraction of H_2 would not be traced by CO emission (see $f_{\rm dark}$ in Table 3.4).

To validate that we can accurately simulate chemistry in molecular clouds, we compare the CO column densities $N_{\rm CO}$ in our simulations to that in the UV absorption observations of diffuse molecular clouds. Figure 3.7 shows the comparison between the simulations and observations, as well as the result from the one-sided slab model in Gong et al. (2017). The x-axis of Figure 3.7 is the extinction from only H_2:

$$A_V(N_{H_2}) = \frac{2N_{H_2}}{1.87 \times 10^{21}\ \rm cm^{-2}}. \tag{3.18}$$

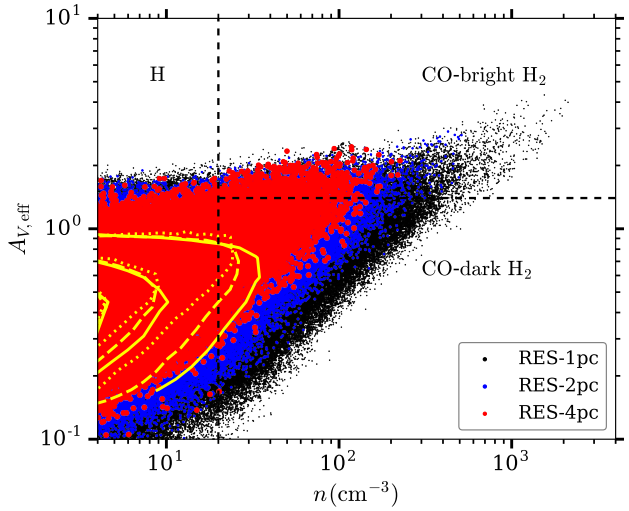


Figure 3.6: Scatter plot of density n versus effective extinction $A_{V,\mathrm{eff}}$ in the models RES-1pc (black), RES-2pc (blue) and RES-4pc (red). The area of each point is proportional to the volume of the grid cell for corresponding resolutions. The contours show the surface densities of the points above which 10%, 50% and 90% points lie, for RES-1pc (solid), RES-2pc (dashed) and RES-4pc (dotted). The dashed lines roughly denote the regions where H, H_2, and CO form (see text in Section 3.2.1).

To avoid foreground/background contamination, we compare N_{CO} to $N_{\mathrm{H_2}}$ instead of the total column N.[5] Comparing to the simulations, the one-sided slab model gives higher CO abundance at $A_V(N_{\mathrm{H_2}}) \sim 1$. This is because the six-ray radiation transfer in the 3D simulations considers extinction of FUV radiation from all directions along the Cartesian axes, which is generally lower than the extinction only along the z-axis, $A_V(N_{\mathrm{H_2}})$ (that is, $A_{\mathrm{V,eff}} \lesssim A_V(N_{\mathrm{H_2}})$). At $A_V(N_{\mathrm{H_2}}) \ll 1$ or $A_V(N_{\mathrm{H_2}}) \gg 1$, the CO abundance in the one-sided slab model and 3D simulations are more similar, because either the FUV radiation is only weakly shielded at low $A_V(N_{\mathrm{H_2}})$ so that the photodissociation rate is insensitive to $A_V(N_{\mathrm{H_2}})$, or else already completely shielded at high $A_V(N_{\mathrm{H_2}})$ so that the limiting factor for CO formation is no longer photodissociation. The UV absorption observations can only be conducted in diffuse molecular clouds with $A_V(N_{\mathrm{H_2}}) \lesssim 1$, and there is a lack of observations at higher extinctions. For the range of $A_V(N_{\mathrm{H_2}})$ where the observational data are available, our

[5]Gong et al. (2017) discussed that the dispersion in observations is much smaller when comparing N_{CO} to $N_{\mathrm{H_2}}$ instead of N.

simulations successfully reproduce the observed range of $N_{\rm CO}$, independent of the numerical resolution.

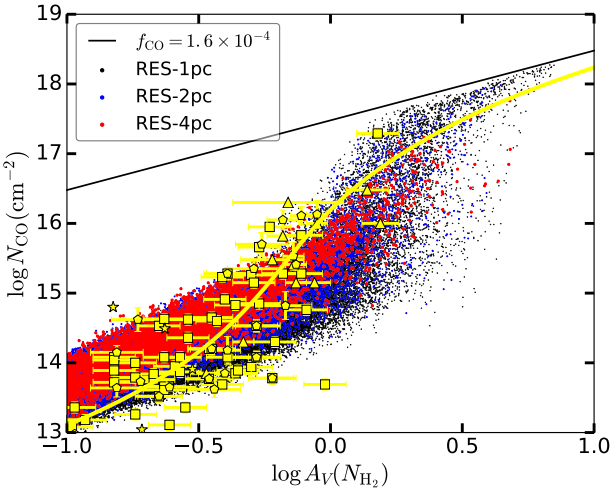


Figure 3.7: Scatter plot of CO column density $N_{\rm CO}$ versus $A_V(N_{\rm H_2})$ in the models RES-1pc (black), RES-2pc (blue) and RES-3pc (red). The area of each point is proportional to the area of the pixel for the corresponding resolution. The black solid line shows where all carbon is in CO, i.e., $f_{\rm CO} = 1.6\times10^{-4}$. The yellow symbols are UV absorption observations in Rachford et al. (2002) (triangles), Sheffer et al. (2008) (squares), Crenny & Federman (2004) (stars) and Burgh et al. (2010) (pentagons), compiled by Gong et al. (2017). The yellow solid line shows the result from the one-sided slab model with constant density $n = 100$ cm^{-3} in Gong et al. (2017).

Dependence of $X_{\rm CO}$ on Numerical Resolution

To understand the relation between physical properties of molecular clouds and CO emission, a helpful reference point is the simple uniform slab model for molecular clouds. In a uniform slab with constant CO excitation temperature $T_{\rm exc}$, Equation (3.7) can be integrated, giving

$$I_\nu = I_\nu(0){\rm e}^{-\tau_\nu} + B_\nu(T_{\rm exc})(1 - {\rm e}^{-\tau_\nu}), \tag{3.19}$$

where $S_\nu = B_\nu(T_{\rm exc})$, the blackbody radiation field intensity at temperature $T_{\rm exc}$, and $I_\nu(0)$ is the initial impinging radiation field intensity at $\tau_\nu = 0$. [6] The line intensity I_ν is usu-

[6] In observations, the intensity is often referred to as the value after background subtraction $I_{\rm obs} = I_\nu - I_\nu(0)$. Then Equation (3.19) is often written as $I_{\rm obs} = (B_\nu(T_{\rm exc}) - I_\nu(0))(1 - {\rm e}^{-\tau_\nu})$.

ally measured in terms of the antenna temperature (also often referred to as the radiation temperature) in radio astronomy:

$$T_A(\nu) = \frac{c^2}{2k\nu^2} I_\nu. \tag{3.20}$$

In the limit of $\tau_\nu \to \infty$, Equations (3.19) and (3.20) becomes

$$T_A = \frac{T_0}{\mathrm{e}^{T_0/T_{\rm exc}} - 1}, \tag{3.21}$$

where $T_0 = 5.5$ K $= h\nu_0/k$, with $\nu_0 = 115.3$ Hz, the frequency of the CO($J = 1 - 0$) line.

Typically, the CO($J = 1 - 0$) line profile (in terms of T_A and v) is not too far from a Gaussian profile, and to first order, the total CO line intensity $W_{\rm CO}$ is determined by two parameters: the peak of the line profile $T_{\rm peak}$ and the width/velocity dispersion of the line σ_v. Under the assumption that the line center is optically thick so that Equation (3.21) applies, the observed peak antenna temperature, $T_{\rm peak}$, would be directly related to the excitation temperature $T_{\rm line}$,

$$T_{\rm line} = \frac{5.5 \text{ K}}{\ln(5.5 \text{ K}/T_{\rm peak} + 1)}. \tag{3.22}$$

We use the notation $T_{\rm line}$ for the excitation temperature derived from the line profile ($T_{\rm peak}$) to distinguish from the true excitation temperature in the molecular clouds $T_{\rm exc}$. Although $T_{\rm line} = T_{\rm exc}$ in a uniform slab cloud as long as the CO line center is optically thick, in real molecular clouds and also in our numerical simulations, the excitation temperature along the line of sight is not constant, and $T_{\rm line}$ serves as an estimate of the excitation temperature where most CO emission comes from. For $T_{\rm peak} \gtrsim 5.5$ K, Equation (3.22) gives $T_{\rm line} \approx T_{\rm peak}$. Another important parameter for the CO line, the velocity dispersion, is calculated using $\sigma_v = \sqrt{\langle v^2 \rangle_{T_A} - \langle v \rangle_{T_A}^2}$, where $\langle v \rangle_{T_A} = \int v T_A \mathrm{d}v / \int T_A \mathrm{d}v$ is the intensity weighted average of velocity, and similarly $\langle v^2 \rangle_{T_A} = \int v^2 T_A \mathrm{d}v / \int T_A \mathrm{d}v$.

The relations between $W_{\rm CO}$ and $T_{\rm line}$ or σ_v in models RES-1pc, RES-2pc and RES-4pc are shown in Figure 3.8. $T_{\rm line}$ ranges from ~ 2 K (from the CMB background) to ~ 20 K (from the kinetic temperature of dense gas as discussed below), similar to the range of excitation temperature observed in Perseus and Taurus molecular clouds (Pineda et al., 2008, 2010). The velocity dispersion spans a relatively narrow range $\sigma_v \approx 1-2$ km/s, and the lower limit for σ_v is set by the sub-grid micro-turbulence velocity in Equation (3.8). The observations of nearby molecular clouds have higher resolutions of $\sim 0.2-0.4$ pc, and therefore a slightly lower but still limited range of velocity dispersions $\sigma_v \approx 0.8-1.5$ km/s (Pineda et al., 2010; Kong et al., 2015). $W_{\rm CO}$ increases with both $T_{\rm line}$ and σ_v. For a Gaussian profile with $T_{\rm peak} \gtrsim 5.5$ K, $W_{\rm CO} = \sqrt{2\pi} T_{\rm peak} \sigma_v \approx \sqrt{2\pi} T_{\rm line} \sigma_v$. Because the variation in σ_v is small, $W_{\rm CO}$ correlates very well with $T_{\rm line}$, except for regions where $T_{\rm line}$ saturates around 20 K. There is no saturation of $W_{\rm CO}$, and $W_{\rm CO}$ keeps increasing with increasing σ_v.

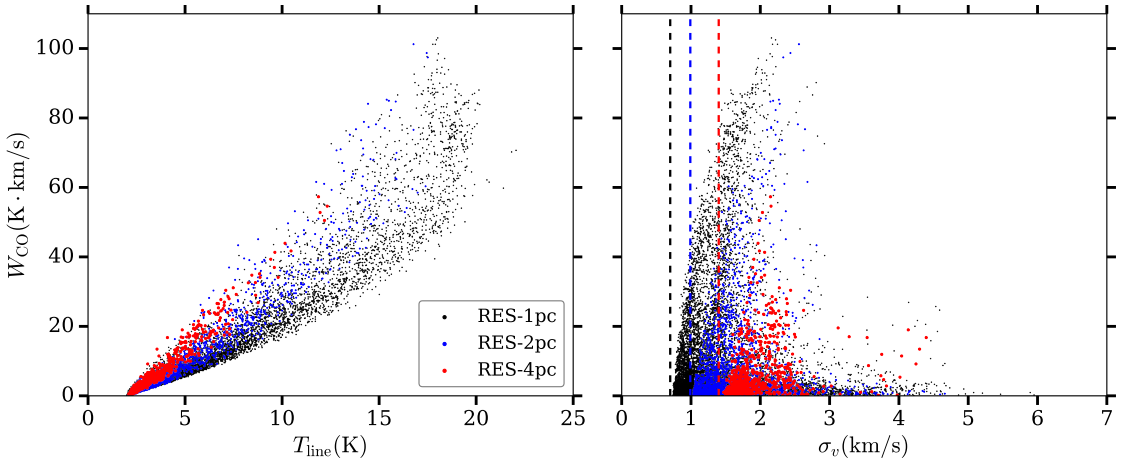


Figure 3.8: *Left*: scatter plot of $W_{\rm CO}$ vs. $T_{\rm line}$ the excitation temperature of the CO($J = 1-0$) at line center (see Equation (3.22)); and *right*: $W_{\rm CO}$ vs. the velocity dispersion of the line σ_v. Both show models RES-1pc (black), RES-2pc (blue) and RES-4pc (red), with the area of points proportional to the area of the pixel at the corresponding resolution. The vertical dashed lines show the sub-grid micro-turbulence parameter (see Equation (3.8)).

$W_{\rm CO}$ is largely determined by the excitation temperature, and the excitation temperature in turn depends on the gas density and temperature. Figure 3.9 shows the excitation temperature $T_{\rm exc}$ and gas temperature $T_{\rm gas}$ versus the gas density in each grid cell. $T_{\rm gas}$

decreases with increasing density, as the gas cooling becomes more efficient, and heating is also reduced by shielding of the FUV radiation field in dense regions. On the other hand, $T_{\rm exc}$ increases with increasing density, because the collisional excitation rate of CO is proportional to density. $T_{\rm exc}$ only reaches equilibrium with $T_{\rm gas}$ at $n \gtrsim 400$ cm^{-3}, showing the local thermal equilibrium (LTE) approximation would fail in most regions.

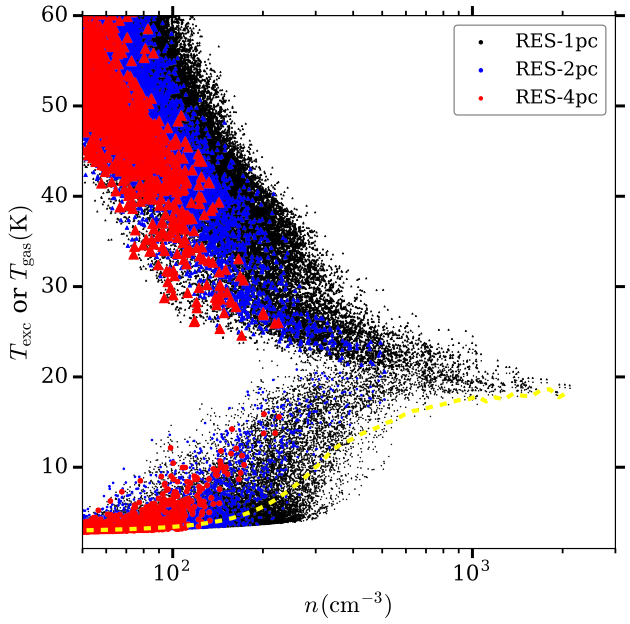


Figure 3.9: Scatter plot of the gas temperature (triangles, upper branch) and excitation temperature of CO($J = 1 - 0$) line (circles, lower branch) versus gas density n in each cell for models RES-1pc (black), RES-2pc (blue) and RES-4pc (red). The area of each point is proportional to the volume of the grid cell at the corresponding resolution. The yellow dashed line is the estimation of $T_{\rm exc}$ in a two-level system model (see Section 3.2.1).

The dependence of $T_{\rm exc}$ on n can be understood in a simplified 2-level system model. The excitation temperature is defined as

$$T_{\rm exc} \equiv \frac{T_0}{\ln\left(\frac{n_0/g_0}{n_1/g_1}\right)}. \tag{3.23}$$

With the escape probability approximation, the level populations are given by (Draine, 2011)

$$\frac{n_1}{n_0} = \frac{n_c k_{01} + \frac{g_1}{g_0}\beta A_{10} n_\gamma^{(0)}}{n_c k_{10} + \beta A_{10}(1 + n_\gamma^{(0)})}, \tag{3.24}$$

where

$$k_{01} = \frac{g_1}{g_0} k_{10} \mathrm{e}^{-T_0/T_{\rm gas}}, \tag{3.25}$$

n_c the number density for the collisional species, β the escape probability in Equation (3.4), and $n_\gamma^{(0)} = 1/(\mathrm{e}^{T_0/T_{\rm CMB}} - 1)$ the background incident radiation field from the CMB[7]. For CO collision with H_2,

$$k_{10} \approx 6 \times 10^{-11} \left(\frac{T_{\rm gas}}{100 \text{ K}} \right)^{0.2} \text{ cm}^3\text{s}^{-1}, \tag{3.26}$$

at 10 K $\lesssim T_{\rm gas} \lesssim$ 250 K (Flower & Launay, 1985; Flower, 2001; Draine, 2011). With increasing density, the optical depth $\tau_{\rm LVG}$ increases, leading to decreasing β (Figure 3.10). We fit the average $\tau_{\rm LVG}$ at a given density with a broken power-law (magenta line in Figure 3.10):

$$\begin{aligned} \tau_{\rm LVG} &= 2.4 \times 10^{-5} (n/\text{cm}^{-3})^{2.3}, \qquad n < 350 \text{ cm}^{-3} \\ \tau_{\rm LVG} &= 0.21 (n/\text{cm}^{-3})^{0.73}, \qquad n \geq 350 \text{ cm}^{-3}. \end{aligned} \tag{3.27}$$

The excitation temperature can be estimated as a function of density by Equations (3.4), (3.23), (3.24) and (3.27) (assuming $\tau = \tau_{\rm LVG}$ in Equation (3.4) and using the average value of $T_{\rm gas}$ at a given density), which is shown as the yellow dashed line in Figure 3.9, and agrees well with the numerical simulations. We can also estimate the critical density for spontaneous emission equals collisional deexcitation (ignoring the background radiation),

$$n_{\rm crit} = \frac{\beta A_{10}}{k_{10}}. \tag{3.28}$$

For $T_{\rm gas} = 20$ K, Equation (3.26) gives $n_{\rm crit} \approx 2.1 \times 10^3 \beta$ cm^{-3}. In density $n \gtrsim 400$ cm^{-3} regions, $\beta \lesssim 0.02$ (Equation (3.27)). Therefore the CO($J = 1$) level is expected to be thermalize at $n \gtrsim 400$ cm^{-3}. The agreement in the excitation temperature between the 2-level system model and the results from RADMC-3D calculations gives us confidence that the CO line radiation transfer has been performed correctly.

[7] If the CMB terms are negligible, Equation (3.23) becomes $T_{\rm exc}/T_0 = [T_0/T_{\rm gas} + \ln(1 + \frac{\beta A_{10}}{n_c k_{10}})]^{-1}$. For β/n_c small, $T_{\rm exc} \to T_{\rm gas}$.

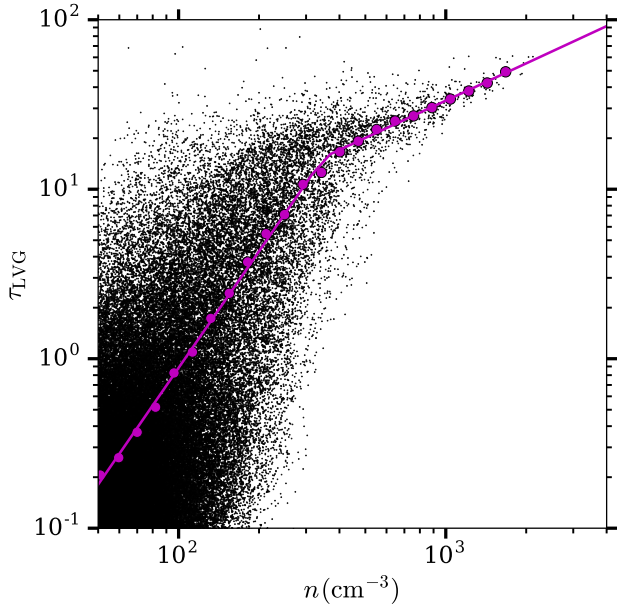


Figure 3.10: Scatter plot of the optical depth from the LVG approximation $\tau_{\rm LVG}$ vs. density n in each grid cell in model RES-1pc. The magenta circles are the binned average of $\tau_{\rm LVG}$, and the line is a broken power-law fit to the circles (Equation (3.27)).

The relation between $W_{\rm CO}$ and $T_{\rm line}$, as well as the relation between $T_{\rm exc}$ and density, give rise to the strong correlation between $W_{\rm CO}$ and the average (mass weighted) density $\langle n \rangle_M$ along the line of sight (Figure 3.11 left panel). Moreover, we found that in the simulations, $N_{\rm H_2}$ increases roughly linearly with $\langle n \rangle_M$ at $N_{\rm H_2} \gtrsim 10^{21}$ cm^{-2}. This results in a correlation between $W_{\rm CO}$ and $N_{\rm H_2}$ (Figure 3.11 right panel). Although $X_{\rm CO}$ is measured in terms of $W_{\rm CO}$ and $N_{\rm H_2}$, there is a smaller dispersion in the correlation between $W_{\rm CO}$ and $\langle n \rangle_M$. This suggests that the CO emission is more fundamentally a measure of H_2 density than column density. This is in contrast to the CO abundances, which depends more strongly on column density than volume density (Figure 3.5).

The effect of numerical resolution on $W_{\rm CO}$ is already evident in Figures 3.9 and 3.11. As the resolution increases, more high density gas forms in the simulation, and thus more pixels with high $W_{\rm CO}$. Numerical resolution also has an effect on $X_{\rm CO}$, as shown in Figure 3.12, the histogram of $X_{\rm CO,20} = X_{\rm CO}/(10^{20}\ {\rm cm}^{-2}{\rm K}^{-1}{\rm km}^{-1}{\rm s})$ weighted by $W_{\rm CO}$. The average $X_{\rm CO}$

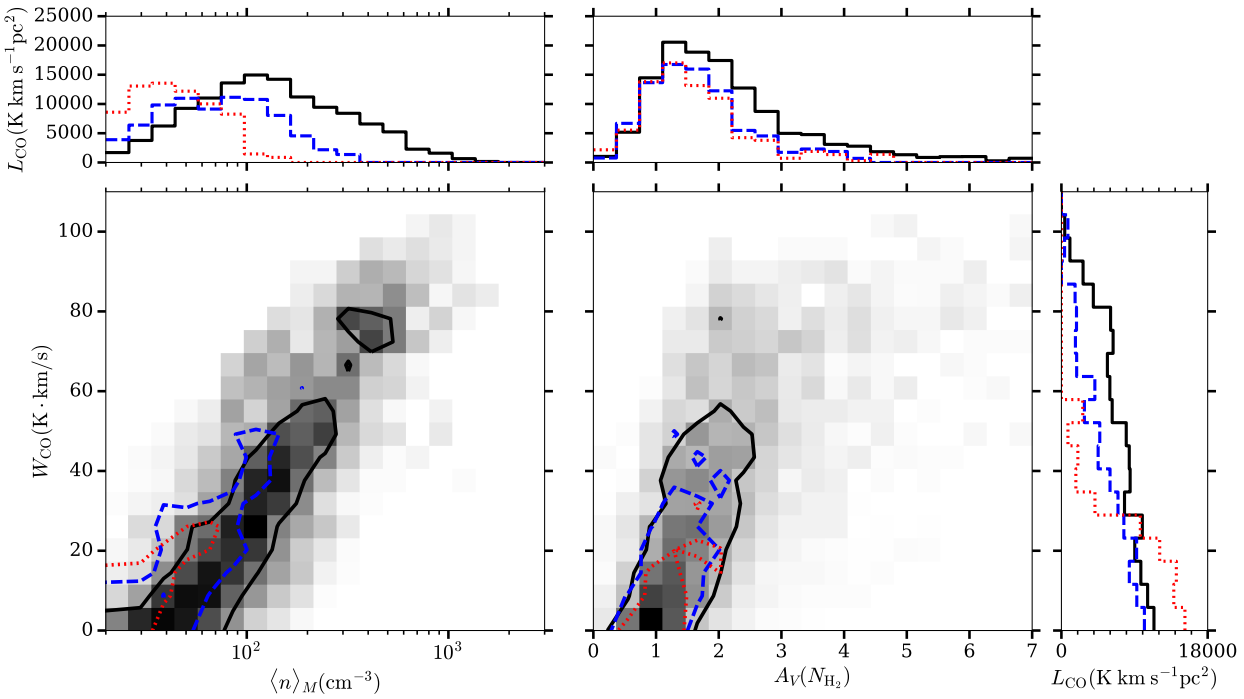


Figure 3.11: Histograms of W_{CO} versus mass-weighted mean density $\langle n \rangle_M$ (*left*) and $A_V(N_{H_2})$ (*right*). The color scale in the 2D histograms is proportional to the total CO luminosity L_{CO} in from each bin in model RES-1pc. The black solid contour of the color scale indicates the regions where 50% of the total CO emission comes from in model RES-1pc. The blue dashed and red dotted contours indicate 50% of the emission, but for models RES-2pc and RES-4pc. The 1D histograms show L_{CO} in each bin for models RES-1pc (black solid), RES-2pc (blue dashed) and RES-4pc (red dotted).

in a certain region can be written as:

$$\langle X_{CO} \rangle = \frac{\sum N_{H_2}}{\sum W_{CO}} = \frac{\sum \frac{N_{H_2}}{W_{CO}} W_{CO}}{\sum W_{CO}} = \frac{\sum X_{CO} W_{CO}}{\sum W_{CO}}. \tag{3.29}$$

In other words, $\langle X_{CO} \rangle$ is simply the W_{CO} weighted average of X_{CO} in each pixel. Therefore, the peak of the histogram in Figure 3.12 roughly indicates the average X_{CO} in the whole simulation domain. The distributions of X_{CO} in models RES-1pc and RES-2pc are very similar, with a slightly higher peak in RES-1pc. As a result, $\langle X_{CO} \rangle$ is almost the same in RES-1pc and RES-2pc (Table 3.4). The model RES-4pc, however, peaks at larger X_{CO} than the higher resolution models, and therefore has a higher $\langle X_{CO} \rangle$. This is because the peak of X_{CO} distribution, $X_{CO,20} \approx 0.5$, comes from regions with moderatly high density

$n \approx 100$ cm^{-3} and CO emission $W_{\rm CO} \approx 40$ K $\cdot$ km/s, which can only be resolved at a resolution finer than 2 pc (see histograms of $\langle n \rangle_M$ and $W_{\rm CO}$ in Figure 3.11). Therefore, we conclude that a numerical resolution of at least 2 pc is needed in order to resolve the the average $X_{\rm CO}$ in molecular clouds for solar neighborhood conditions.

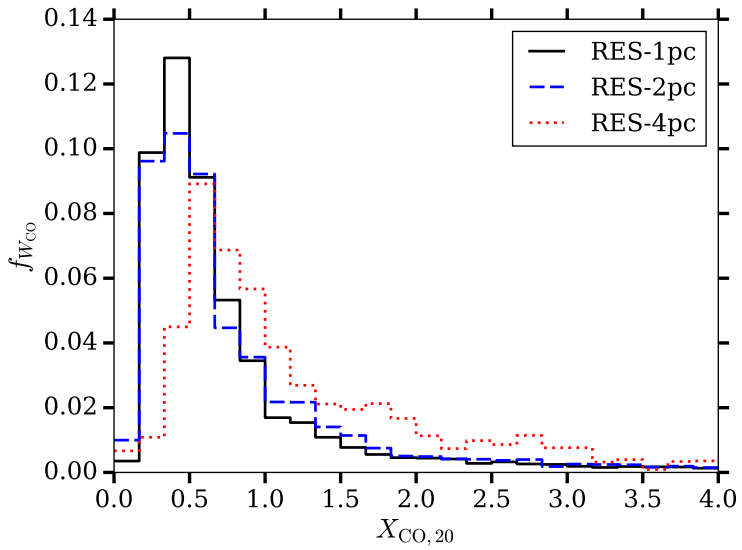


Figure 3.12: Histograms of $X_{\rm CO,20}$ weighted by $W_{\rm CO}$, in models RES-1pc (black solid), RES-2pc (blue dashed) and RES-4pc (red dotted).

Finally, we compare the distribution of $W_{\rm CO}$ versus $A_V(N_{\rm H_2})$ in model RES-1pc to observations of the Orion A and B molecular clouds by Ripple et al. (2013), as shown in Figure 3.13. Considering the noise level in the observation, we use a higher threshold of $W_{\rm CO} > 1$ K $\cdot$ km/s to compare to the CO-bright region in Orion. Because most CO emission comes from regions with $W_{\rm CO} \gg 1$ K $\cdot$ km/s, $X_{\rm CO}$ is not sensitive to the $W_{\rm CO}$ threshold. The average $X_{\rm CO}$ in RES-1pc is a factor of 1.4 lower than that in Orion, but the trend for the distribution of $W_{\rm CO}$ versus $A_V(N_{\rm H_2})$ is similar. The dispersion of $W_{\rm CO}$ at a given $A_V(N_{\rm H_2})$ is large, as much as more than an order of magnitude at low $A_V(N_{\rm H_2})$. However, despite the large dispersion of $W_{\rm CO}$, the average $X_{\rm CO}$ (which is inversely proportional to the slope) in different $A_V(N_{\rm H_2})$ bins is very similar, only varying by a factor of ~ 2. Similar features are observed in many Milky Way molecular clouds by Lee et al. (in prep), and we discuss this in more detail at the end of Section 3.2.3. There are also some differences between the

simulation and observations. Because the observation in Ripple et al. (2013) has a higher spatial resolution of ~ 0.2 pc, there are more pixels at $A_V(N_{\rm H_2}) \gtrsim 4$ in the observation. The simulation has more pixels at $W_{\rm CO} \gtrsim 60$ K $\cdot$ km/s, a result from the slightly higher velocity dispersions (see Figure 3.8 and discussions). The general good agreement between the models and observations indicates that the simulations can succesfully reproduce the basic physical properties of observed molecular clouds. We discuss the slightly lower average $X_{\rm CO}$ in our simulations compared to dust-based observations in detail at the end of Section 3.2.3.

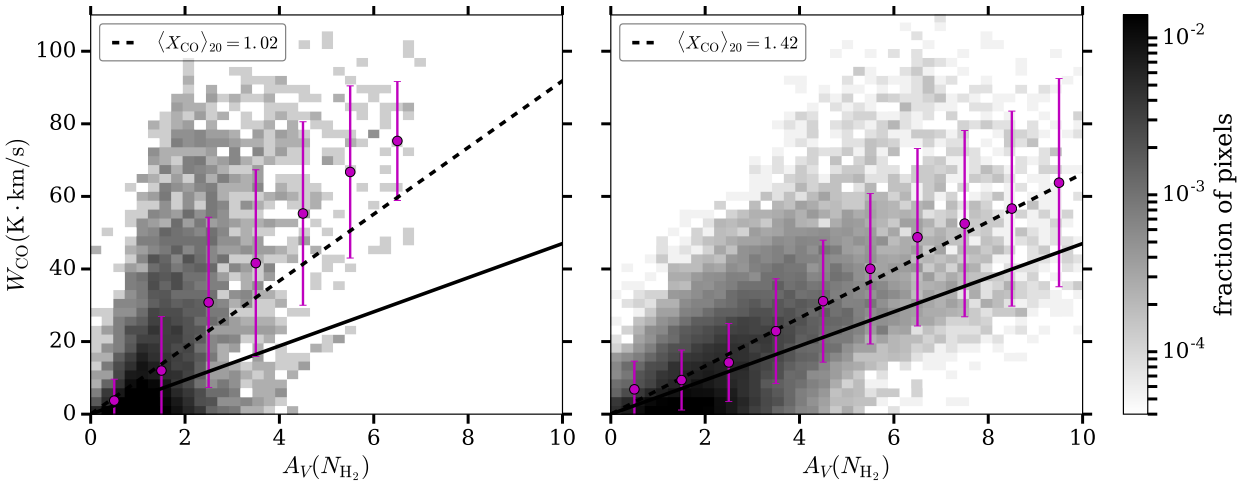


Figure 3.13: *Left*: 2D histogram of $W_{\rm CO}$ versus $A_V(N_{\rm H_2})$ in model RES-1pc. The magenta filled circles and error bars show the average value and standard deviation of $W_{\rm CO}$ in each $A_V(N_{\rm H_2})$ bin. The black solid line shows the standard Milky Way value of $X_{\rm CO,MW,20} = 2$. The black dashed line shows the average $X_{\rm CO}$ in model RES-1pc, $\langle X_{\rm CO}\rangle_{20} = 1.02$. *Right*: similar to the left panel, but for the observations of Orion A and B molecular clouds by Ripple et al. (2013). The average $X_{\rm CO}$ for the Orion A and B clouds is $\langle X_{\rm CO}\rangle_{20} = 1.42$.

3.2.2 Non-equilibrium Chemistry

The realistic ISM is highly dynamical: turbulence constantly creates and disperses molecular clouds, and moves gas to environments with different density, temperature and radiation field strength. As a result, non-equilibrium chemistry is likely to be important, especially in low density diffuse gas where the chemical timescales are long compared to the dynamical

timescales. This is especially an issue for H_2, which can form in low density gas due to its effective self-shielding, but its formation timescale, $t_{H_2} \approx 10\text{Myr}\ (n/100\ \text{cm}^{-3})^{-1}$ (Gong et al., 2017), can be longer than the dynamical timescale (Equation (3.2)). Because CO formation chemically relies on the existence of H_2, the CO abundance in molecular clouds can also be far from equilibrium. In this section, we carry out comparisons between models with different $t_{\rm chem}$ (model IDs start with TCHEM in Table 3.3) to investigate the effect of non-equilibrium chemistry on $X_{\rm CO}$.

Both H_2 and CO abundance increase over $t_{\rm chem}$, reaching equilibrium at $t_{\rm chem} \approx 50$ Myr, as shown in Figure 3.14. Over timescales relevant for clouds of size $\gtrsim 10$ pc (Equation (3.2)), there is a larger increase in the H_2 abundance than CO: From $t_{\rm chem} = 5$ Myr to 50 Myr, the H_2 abundance increases by a factor of ~ 3, while CO abundance increases only by $\sim 30\%$.

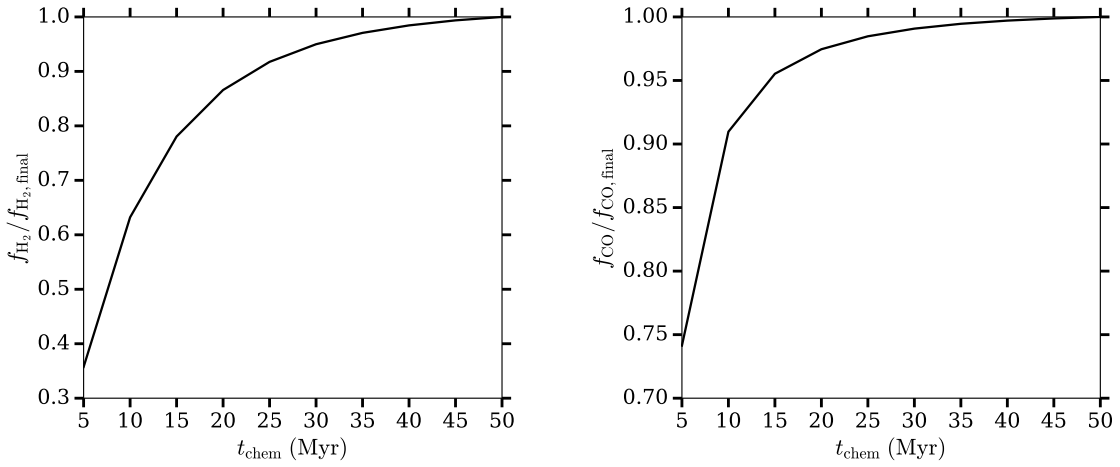


Figure 3.14: The abundance of H_2 (*left*) and CO (*right*) as a function of $t_{\rm chem}$ in TCHEM models. The y-axis is normalized by the final H_2 or CO abundance at $t_{\rm chem} = 50$ Myr.

The difference in the evolution of H_2 and CO abundance comes from their different distributions. As shown in Figure 3.15, the change of f_{H_2} and $f_{\rm CO}$ at a given density is similar. Both H_2 and CO abundances are closer to equilibrium at higher densities, as the rate of collisional reactions increases with density. However, most H_2 forms at intermediate densities $n \approx 10 - 100\ \text{cm}^{-3}$, but most CO forms at high densities $n \gtrsim 200\ \text{cm}^{-3}$ (Figure 3.3). This leads to a shorter timescale for the overall CO abundance to reach equilibrium

than H_2. Since the CO luminosity also increases much less than the H_2 mass, this leads to a lower X_{CO} value at early t_{chem} (Table 3.4).

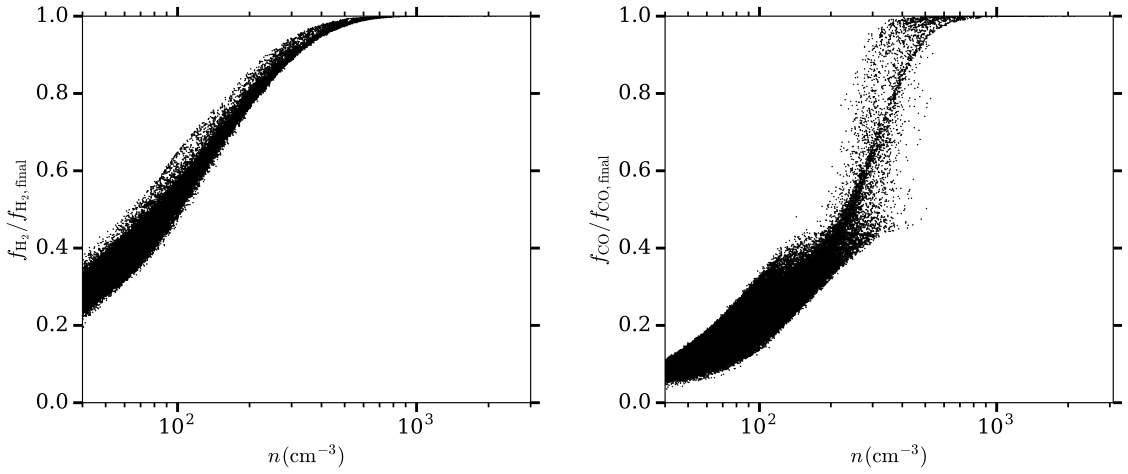


Figure 3.15: Scatter plot of f_{H_2} (*left*) and f_{CO} (*right*) versus density n for model TCHEM-5Myr. f_{H_2} and f_{CO} in each grid cell is normalized to the equilibrium abundance $f_{H_2,final}$ and $f_{CO,final}$ in that grid cell at $t_{chem} = 50$ Myr (in model TCHEM-50Myr).

Non-equilibrium chemistry also has an effect on the distribution of W_{CO} vs. $A_V(N_{H_2})$. For model TCHEM-5Myr (Figure 3.16), the distribution of the pixels are shifted to the left compared to that in TCHEM-50Myr (left panel of Figure 3.13). This is because W_{CO} is close to equilibrium, but N_{H_2} is a factor of ~ 2 smaller than the equilibrium values, for the same reasons discussed above. Moreover, the distribution of W_{CO} vs. $A_V(N_{H_2})$ in TCHEM-5Myr shows some hints of a plateau for W_{CO} at high $A_V(N_{H_2})$, especially in the binned average value of W_{CO}, which is not present in TCHEM-50Myr. This implies that younger clouds may not only have lower X_{CO} on average, but also different distributions of W_{CO} vs. $A_V(N_{H_2})$ compared to older clouds. We discuss this further at the end of Section 3.2.3 (Figure 3.20). Note that N_{H_2} includes all H_2 along the line of sight, both in high density clumps where CO forms, and in the foreground/background low density envelopes with only H_2 and no CO. Because most H_2 lies in these low density envelopes, the fractions of H_2 in CO-bright and CO-dark regions increase by similar proportions with t_{chem}, and f_{dark} stays constant from $t_{chem} = 5$ Myr to $t_{chem} = 50$ Myr (Table 3.4).

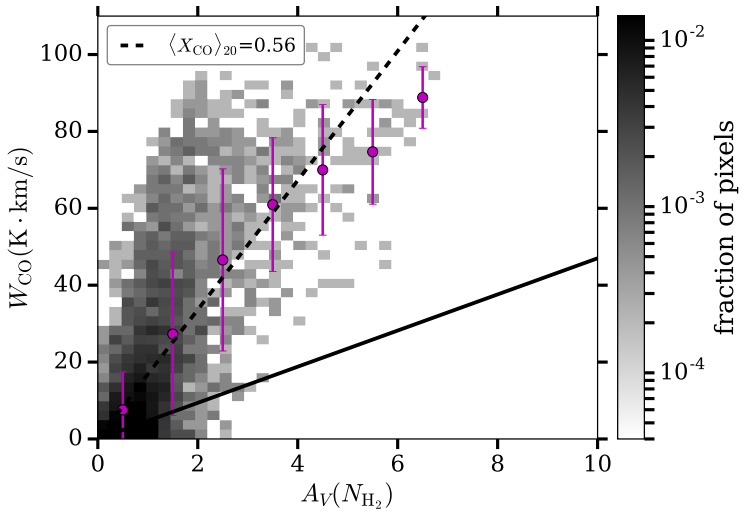


Figure 3.16: Similar to the left panel of Figure 3.13, but for model TCHEM-5Myr.

3.2.3 Variations in Galactic Environments

Galactic environment fundamentally impacts the molecular content of the ISM. Supernova feedback creates and destroys molecular clouds, shocks and turbulence shape molecular clouds in different morphologies, and the radiation field varies with the star formation activities. Some of these effects can be seen visually in Figure 3.17. The morphology of molecular clouds varies from dense concentrated structures (such as in T-356Myr), to more diffuse, smaller clouds (such as in T-406Myr). The mass and number of young clusters also changes over time, reflecting the variations in the star formation rate. To quantify the effect of time-varying galactic environment on $X_{\rm CO}$, we compare models with 2 pc resolution at different times during the galactic evolution (model IDs start with T in Table 3.3). As discussed in Section 3.2.1, the average $X_{\rm CO}$ is well resolved with a resolution of 2 pc in these simulations.

A summary of models T-356Myr – T-416Myr is listed in Table 3.5. In these models, $M_{\rm H_2}$ and $L_{\rm CO}$ vary by factor of $\sim$ 3, and the incident radiation field strength varies by a factor of $\sim$ 8. However, despite these large variations in the environment, $\langle X_{\rm CO}\rangle$ stays almost constant, changing only by $\sim$ 40%. We found no strong correlation (coefficient of determination $R^2 > 0.4$ in linear regression) between $\langle X_{\rm CO}\rangle$ and $M_{\rm H_2}$, the radiation field strength χ, or the average extinction from H_2 in CO-bright regions $\langle A_V\rangle_{\rm CO}$. Remy et al.

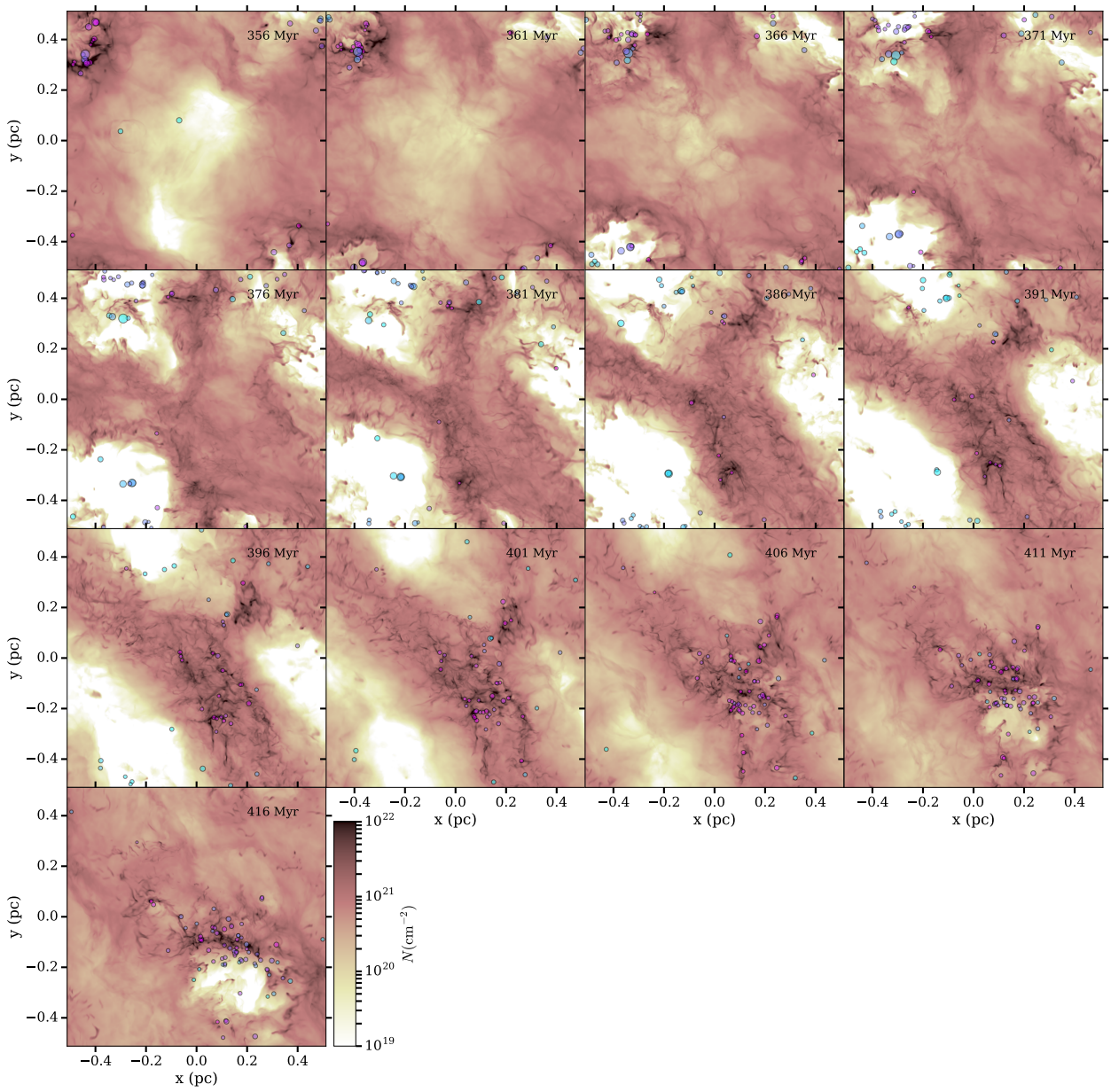


Figure 3.17: Total gas surface density N in models T-356Myr – T-416Myr. The star clusters are shown in circles, similar to Figure 3.1 top panels.

(2017) measured $\langle X_{\rm CO} \rangle$ in individual Milky Way molecular clouds using γ-ray observations, and they also found no strong correlation between $\langle X_{\rm CO} \rangle$ and $M_{\rm H_2}$ or $\langle A_V \rangle_{\rm CO}$.[8] Also similar to Remy et al. (2017), we found a correlation between $\langle X_{\rm CO} \rangle$ and $\langle W_{\rm CO} \rangle$, but with a shallower slope and higher $\langle W_{\rm CO} \rangle$ (left panel of Figure 3.18).

[8]Remy et al. (2017) shows a correlation between $\langle X_{\rm CO} \rangle$ and $\langle A_V \rangle_{\rm CO}$ with $R^2 \approx 0.6$. However, this relation is largely driven by one outlier, the Perseus cloud, which has much lower $\langle X_{\rm CO} \rangle$ and higher $\langle A_V \rangle_{\rm CO}$ than the rest of the sample. Excluding the Perseus cloud, we found no strong correlation ($R^2 \approx 0.3$) between $\langle X_{\rm CO} \rangle$ and $\langle A_V \rangle_{\rm CO}$ for the rest of their sample.

Table 3.5: Overall properties of models: variations in galactic environment

model ID	$M_{\rm tot}(M_\odot)$	$M_{\rm H_2}(M_\odot)$	$M_{\rm CO}(M_\odot)$	$L_{\rm CO}$(K km s^{-1}pc^2)	$\langle X_{\rm CO}\rangle_{20}$	$f_{\rm dark}$	f_{100}	$2\langle f_{\rm H_2}\rangle$	$\chi^{\rm a}$
T356-Myr	8.02×10^6	5.61×10^5	4.52×10^2	3.64×10^5	0.71	26%	4.5%	10%	3.0
T361-Myr	7.93×10^6	4.25×10^5	1.63×10^2	1.96×10^5	0.81	41%	2.7%	8%	1.8
T366-Myr	7.78×10^6	3.38×10^5	8.67×10^1	1.00×10^4	0.83	61%	1.5%	6%	1.1
T371-Myr	7.64×10^6	3.03×10^5	4.11×10^1	5.31×10^4	0.74	79%	0.6%	6%	0.9
T376-Myr	7.45×10^6	5.34×10^5	5.86×10^1	8.23×10^4	0.95	77%	0.7%	10%	0.4
T381-Myr	7.41×10^6	6.85×10^5	8.19×10^1	1.10×10^4	1.00	74%	0.9%	13%	0.4
T386-Myr	7.47×10^6	8.54×10^6	2.17×10^2	2.40×10^5	0.85	62%	1.8%	16%	0.4
T391-Myr	7.59×10^6	1.04×10^6	3.77×10^2	3.60×10^5	0.83	54%	2.6%	19%	0.4
T396-Myr	7.75×10^6	9.25×10^6	3.16×10^2	3.47×10^5	0.84	49%	3.5%	17%	1.0
T401-Myr	7.97×10^6	8.40×10^6	2.73×10^2	3.09×10^5	0.85	50%	3.6%	15%	1.4
T406-Myr	8.16×10^6	6.82×10^5	1.93×10^2	2.16×10^5	0.96	51%	3.1%	12%	1.9
T411-Myr	8.29×10^6	6.06×10^5	1.68×10^2	2.06×10^5	0.90	51%	2.4%	10%	1.4
T416-Myr	8.28×10^6	5.51×10^5	1.76×10^2	2.19×10^5	0.79	50%	2.2%	9%	1.0
average	7.83×10^6	6.42×10^5	2.00×10^2	2.16×10^5	0.85	56%	2.3%	12%	1.2

[a] FUV radiation field intensity in Draine (1978) units.

Unlike $\langle X_{\rm CO}\rangle$, the fraction of CO-dark H_2, $f_{\rm dark}$, does show significant variations and a strong correlation ($R^2 = 0.6$) with $\langle A_V\rangle_{\rm CO}$ (Figure 3.18 right panel). $f_{\rm dark}$ increases with decreasing $\langle A_V\rangle_{\rm CO}$. In other words, there is more CO-dark H_2 in more diffuse molecular clouds, which is not surprising as CO forms in denser gas than H_2. The same trend was identified in the simplified spherical molecular cloud model by Wolfire et al. (2010).[9] We have also performed an experiment by running the T-381Myr model only varying the radiation field strength, and found $f_{\rm dark}$ stays constant over $\chi = 0.4 - 3.5$, confirming the result from Wolfire et al. (2010) that $f_{\rm dark}$ is not sensitive to χ.

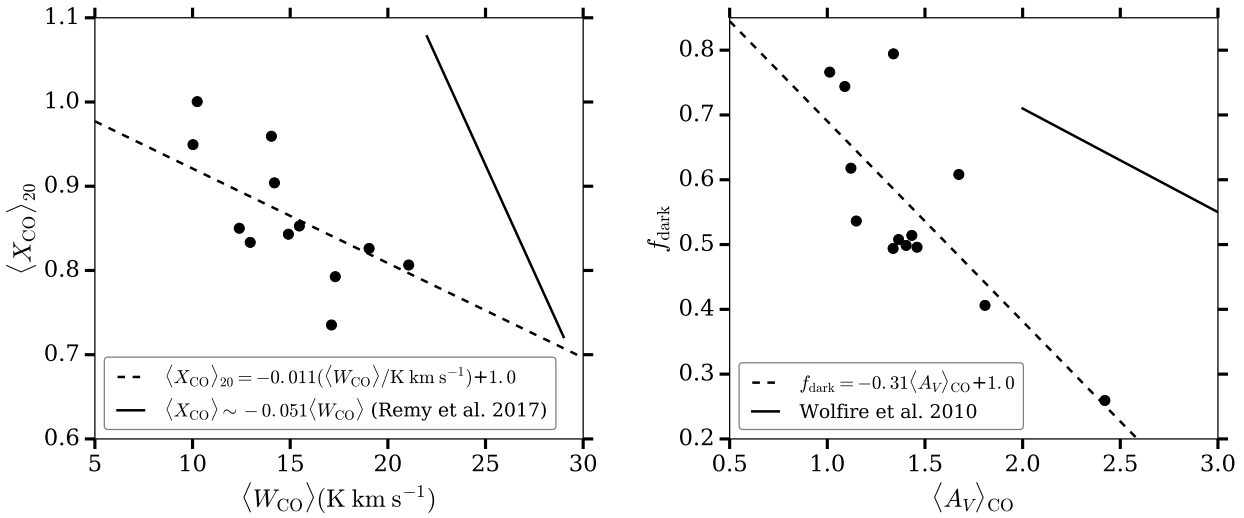


Figure 3.18: $\langle X_{\rm CO}\rangle$ vs. $\langle W_{\rm CO}\rangle$ (*left*), and $f_{\rm dark}$ vs. $\langle A_V\rangle_{\rm CO}$ (*right*) in models T-356Myr – T-416Myr. The dashed lines are the linear fits to the simulation data, and the solid lines are observations from Remy et al. (2017) (their Figure 12, note the line only shows the slope, not the absolute value) in the left panel, and the theoretical model of spherical molecular clouds in Wolfire et al. (2010) (their Figure 11) in the right panel.

Another comparison in $X_{\rm CO}$ with observations is shown in Figure 3.19, where the $X_{\rm CO}$ in each pixel is plotted against $T_{\rm line}$. Comparing to the California cloud observed by Kong et al. (2015), our simulations shows a similar slope for the relation between $X_{\rm CO}$ and $T_{\rm line}$ at $T_{\rm line} > 6$ K (the observational data are not available at lower $T_{\rm line}$). However, the value of $X_{\rm CO}$ at a given $T_{\rm line}$ is about a factor of ~ 3 lower than the observations. One reason for

[9]The result from Wolfire et al. (2010) shown in Figure 3.18 is taken from their model with metallicity $Z' = 1.9$ and incident radiation field $\chi = 10$. Wolfire et al. (2010) found that $f_{\rm dark}$ is not sensitive to Z' or χ in their studies.

this discrepancy may be that Kong et al. (2015) observed CO($J = 2 - 1$) line and assumed a fix line ratio of $W_{\rm CO}(J = 2 - 1)/W_{\rm CO}(J = 1 - 0) = 0.7$, and this ratio is very uncertain. As discussed below in more detail, generally different observations and also our simulations show similar trends for the variations in $X_{\rm CO}$, but the absolute value of $X_{\rm CO}$ can differ by a factor of a few.

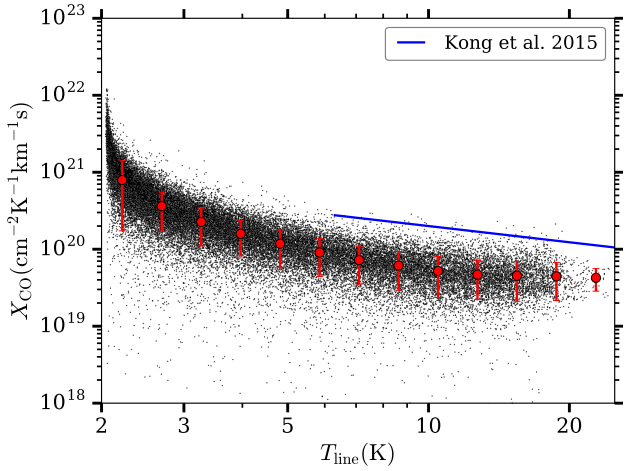


Figure 3.19: Scatter plot of $X_{\rm CO}$ vs. $T_{\rm line}$ in models T-356Myr – T-416Myr. Each point is one pixel in the simulations. The red filled circles with error bars are the binned mean values and standard deviations of $X_{\rm CO}$. The blue solid line shows the observed relation in Kong et al. (2015).

Using all of the simulation models, a summary of $X_{\rm CO}$ as a function of $A_V(N_{\rm H_2})$ and comparison with observations is shown in Figure 3.20. Because of the large uncertainties in observations of $X_{\rm CO}$ at low $A_V(N_{\rm H_2})$, we only plot the data at $A_V(N_{\rm H_2}) > 1$. Both in our simulations and the observations, there is a factor of ~ 2 variation in $X_{\rm CO}$ over $A_V(N_{\rm H_2}) = 1 - 12$. Simulations with $t_{\rm chem} = 50$ Myr (RES-1pc, RES-2pc, T-356Myr – T-416Myr) show a decrease of $X_{\rm CO}$ at $A_V(N_{\rm H_2}) \lesssim 3$, regardless of the resolution and variations in galactic environments. Similar trends can be seen in the observations of Orion molecular clouds by Lee et al. (in prep) and Ripple et al. (2013). In contrast, the TCHEM-5Myr model shows a flatter profile at $A_V(N_{\rm H_2}) \lesssim 3$ and a slight increase of $X_{\rm CO}$ at $A_V(N_{\rm H_2}) > 3$. Interestingly, the California cloud observed by Lee et al. (in prep) also shows a similar trend. Compared to Orion, the California cloud has similar mass and distance, but an order

of magnitude lower star formation rate, and therefore is believed to be much younger (Lada et al., 2009). This has interesting implications that the profile of $X_{\rm CO}$ as a function of $A_V(N_{\rm H_2})$ may be used as an indicator of the age of molecular clouds.

Although the trend for the correlation between $X_{\rm CO}$ and $A_V(N_{\rm H_2})$ is similar in our simulations and observations, there is a discrepancy in the absolute value of $X_{\rm CO}$. This may be due to systematic errors in either observations or simulations. One major uncertainty in observations of $X_{\rm CO}$ comes from the assumptions in deriving $N_{\rm H_2}$. Estimations of $\rm H_2$ based on γ-ray systematically give a factor of 2 lower $X_{\rm CO}$ than dust-based methods (Bolatto et al., 2013b), which can also be seen in Figure 3.20.[10] Even within the dust-based methods, the estimate of $X_{\rm CO}$ in Orion A based on dust emission is a factor of ~ 2 higher in observations of Lee et al. (in prep) compared to that in Ripple et al. (2013) based on dust extinction. As another example, the $X_{\rm CO}$ in Perseus measured by Lee et al. (2014b) (dust emission) is a factor of ~ 7 lower than that in Pineda et al. (2008) (dust extinction). Several possible factors can contribute to the systematics in dust-based observations: different assumptions of the dust to gas ratio, uncertainties in foreground/background subtraction, and different resolutions/beam size (although the resolution effect is relatively mild, as noted by Lee et al. (2014b) and discussed in Section 3.2.4). Lee et al. (2014b) discussed in detail for the case of Perseus molecular cloud, that all these factors can indeed lead to a different estimate of $X_{\rm CO}$. For the numerical simulations, the main uncertainties lie in the assumptions of equilibrium chemistry and the sub-grid model of micro-turbulence in calculating the CO emission. Future AMR simulations with higher numerical resolution and non-equilibrium chemistry will be able to provide more insights into these issues.

[10]The observation by Remy et al. (2017) in Figure 3.20 is averaged over the molecular clouds instead of individual pixels in a given $A_V(N_{\rm H_2})$ range. Nonetheless, it indicates the systematically lower $X_{\rm CO}$ in γ-ray observations.

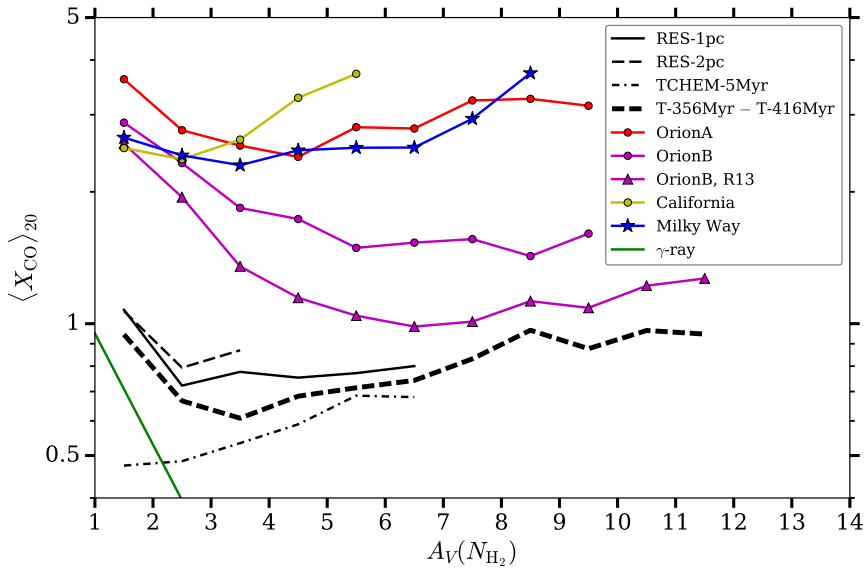


Figure 3.20: The average $X_{\rm CO}$ binned in $A_V(N_{\rm H_2})$. The black lines are the simulation models of RES-1pc (solid), RES-2pc (thin dashed), TCHEM-5Myr (dash dotted), and T-356Myr – T-416Myr (thick dashed). The filled circles show the observations of molecular clouds in Lee et al. (in prep) for California (yellow), Orion A (red), and Orion B (magenta). The blue stars show the average of all Milky Way clouds in Lee et al. (in prep). The magenta triangles show the observations of Orion A by Ripple et al. (2013). The green solid line plots the γ-ray observations averaged over individual molecular clouds in Remy et al. (2017).

3.2.4 Dependence of $X_{\rm CO}$ on the Observational Beam Size

Observation of molecular clouds often have different physical beam sizes/resolutions, which depend on the telescope as well as the distance of the object. In order to investigate the effect of observational resolution on $X_{\rm CO}$, we smooth the synthetic observations to different beam sizes as described in Section 3.1.4.

$\langle X_{\rm CO}\rangle$ increases by a factor of ~ 2 as the beam size increases from ~ 1 pc to ~ 100 pc, as shown in Figure 3.21. This is a result of the CO-dark H_2. The total CO emission remains the same as the beam size increases, because the detection limits for different beam sizes (Table 3.2) are generally sensitive enough to detect the most of the CO emission. This is not surprising as the sensitivity in observations are designed to serve the purpose of accurately measuring the CO emission. However, the CO emission is smoothed out spatially as the beam size increases, resulting in a larger area of CO-bright regions. Although the total mass

of H_2 remains the same, because X_{CO} is calculated only within CO-bright regions, a larger area of CO-bright regions leads to a larger fraction of H_2 mass accounted for, and therefore an increase of X_{CO}. This is clearly illustrated in Figure 3.22, showing the correlation between f_{dark} and $\langle X_{CO} \rangle$. From beam sizes of $\sim$ 100 pc to $\sim$ 1 kpc, some simulations show a continued increase of X_{CO} (e.g. T-401Myr), but some simulations with more diffuse molecular clouds (e.g. T-381Myr) start to have part or all of their CO emission falling below the detection limits, leading to a non-detection of W_{CO} or reduction of X_{CO}. This suggests that some diffuse molecular clouds may not be detected with a beam size coarser than $\sim$ 100 pc in extragalactic observations.

In Figure 3.21, we plot the observations of $\langle X_{CO} \rangle$ in the Milky Way molecular clouds and nearby galaxies (Table 3.1). Because of the large uncertainties in the observations (as discussed above, and also seen directly in the different $\langle X_{CO} \rangle$ from two Perseus observations) and dispersions of $\langle X_{CO} \rangle$ in different molecular clouds, we cannot identify any obvious trend for the X_{CO} variation with beam size. The general range of X_{CO} in the simulations is similar to the observations.

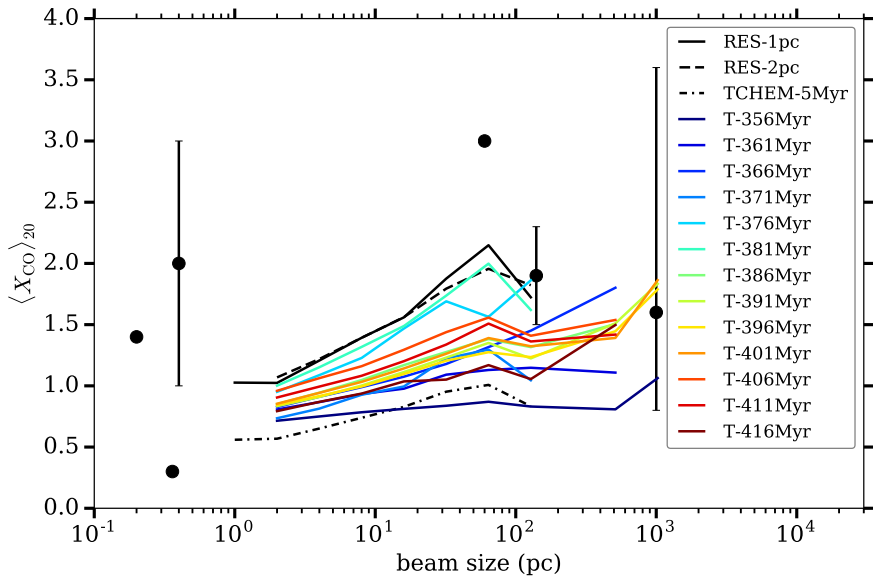


Figure 3.21: $\langle X_{CO} \rangle_{20}$ as a function of beam size in different models (see label). The black circles (with error bars) are observations from Table 3.1.

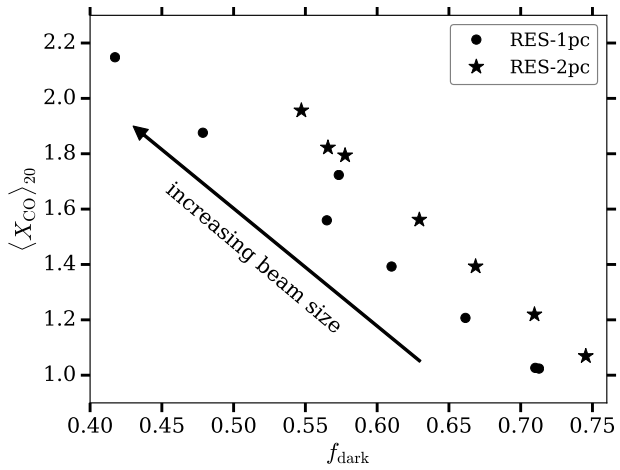


Figure 3.22: $\langle X_{\rm CO}\rangle_{20}$ vs. $f_{\rm dark}$ in models RES-1pc and RES-2pc. Each point is for a different beam size in Figure 3.21.

3.3 Summary

In this chapter, we theoretically model the $X_{\rm CO}$ conversion factor by post-processing MHD galactic disk ISM simulations with chemistry and radiation transfer to produce synthetic observations of molecular clouds. We conduct detailed analyses of the dependence of molecular abundances and observed line strengths on ISM conditions, and also consider numerical and observational effects on calculated and measured $X_{\rm CO}$. Our main findings are as follows:

1. CO is only a very approximate tracer of H_2. In our simulations, most H_2 forms at intermediate densities $n \approx 10 - 100$ cm^{-3}, but most CO forms at higher densities $n \gtrsim 200$ cm^{-3} (Figure 3.3). The H_2 abundance is determined mostly by density, while the CO abundance by dust shielding (Figures 3.4, 3.5). With a 2 pc numerical resolution, H_2 abundance is converged, but CO is not. Although there is considerable scatter, the mean relation between the CO and H_2 column densities in the simulations are in agreement with observations of UV absorption spectra (Figure 3.7).

2. For CO emission, the high optical depth of the line further complicates the observable relation to H_2. On parsec scales, $W_{\rm CO}$ is largely determined by the mean excitation temperature of CO (Figure 3.8), which is in turn determined by the mean gas density.

Thus, $W_{\rm CO}$ most directly probes the mean gas density along the line of sight. However, for the turbulent clouds in our simulations, the mass-weighted mean volume density along a line of sight tends to be correlated with column density. This leads to a correlation between $W_{\rm CO}$ and $N_{\rm H_2}$ (Figure 3.11).

3. A numerical resolution of at least 2 pc is needed in order to resolve the average $X_{\rm CO}$ in molecular clouds for solar neighborhood conditions (Figure 3.12). In our simulations with environmental conditions similar to the solar neighborhood, we found $\langle X_{\rm CO} \rangle = 0.7 - 1.0 \times 10^{20}$ cm^{-2}K^{-1}km^{-1}s. The value of $\langle X_{\rm CO} \rangle$ is not sensitive to the variations in molecular cloud mass, extinction, or the strength of the FUV radiation field (Table 3.5).

4. We found the CO-dark H_2 fraction $f_{\rm dark} = 26 - 79\%$, which has an anti-correlation with the average extinction of molecular clouds (Figure 3.18 right panel).

5. The chemical timescale for H_2 abundance to reach equilibrium is longer than that for CO (Figure 3.14), because of differences in characteristic densities. As a result, younger molecular clouds are expected to have lower $\langle X_{\rm CO} \rangle$ values and flatter profiles of $X_{\rm CO}$ versus extinction compared to older molecular clouds (Figures 3.16, 3.20).

6. As the observational beam size increases from ~ 1 pc to ~ 100 pc, $\langle X_{\rm CO} \rangle$ increases by a factor of ~ 2, due to the decrease of the CO-dark H_2 fraction (Figures 3.21, 3.22).

7. Our numerical simulations successfully reproduce the observed variations of $W_{\rm CO}$ on parsec scales, as well as the dependence of $X_{\rm CO}$ on extinction and the CO excitation temperature (Figures 3.13, 3.19, 3.20).

Chapter 4

Conclusions

In this thesis, we study different aspects of integrating chemistry in numerical simulations of the star forming ISM. Chemistry allows more accurate calculations of the gas thermodynamics and enables direct comparisons between simulations and observations. Due to the rapidly increasing computational power, we expect the inclusion of chemistry in ISM simulations to be commonplace in the near future.

To reduce the computational cost of simulating chemistry, we developed a new simplified chemical network for the atomic and molecular ISM in chapter 2. Our network focuses on the carbon and oxygen species, especially the formation of CO, and includes the main heating and cooling processes that regulate the gas temperature. By comparing our results with those from a much more complex PDR code, we show that our simplified network produces accurate abundances of all chemical species.

We use our chemical network to study the $X_{\rm CO}$ conversion factor in galactic disk ISM simulations in Chapter 3. We investigate how $X_{\rm CO}$ depends on numerical resolution, non-equilibrium chemistry, ISM conditions and observational beam size. We show that our simulations not only reproduce the average observed $X_{\rm CO}$ in molecular clouds, but also the variation of $X_{\rm CO}$ on smaller-than-cloud scales and its dependence on extinction and CO excitation temperature. Our work demonstrates that the combination of accurate chemistry and

realistic ISM structures in numerical simulations is essential to understanding the complex observational phenomena of the molecular clouds.

Finally, we offer some closing remarks on our planned future work. As a direct continuation of the work in Chapter 3, we plan to study the properties of individual molecular clouds, such as their virial parameter, lifetime, and relation to the star formation activities. The agreement between our numerical simulations and observations of Milky Way molecular clouds gives us confidence that similar simulations can be used to probe the $X_{\rm CO}$ conversion factors in different environments, such as the Galactic center, low metallicity dwarfs, and extreme star-forming systems (ultra luminous infrared galaxies and high redshift galaxies). We also plan to integrate full non-equilibrium chemistry with the MHD simulations.

Appendix A

Description of the Chemical Network

A summary of the chemical network is listed in Tables A.1 and A.2.

A.1 Extension of the NL99 Network

We have added or modified the following reactions to the NL99 network:

1. H_3^+ destruction channel

$$H_3^+ + e \rightarrow 3H$$

in addition to

$$H_3^+ + e \rightarrow H_2 + H$$

in the original NL99 network, to be more consistent with the hydrogen network adopted in Glover et al. (2010) and Indriolo et al. (2007).

2. Grain-assisted recombination of C^+ and He^+:

$$C^+ + e + gr \rightarrow C + gr$$

$$He^+ + e + gr \rightarrow He + gr$$

These two grain surface reactions are the main channels for C^+ and He^+ recombination at solar metallicity. Glover & Clark (2012a) considered these two reactions, and concluded that they made very little difference in determining where CO would form. However, we found that using the updated cosmic-ray ionization rate $\xi_H = 2\times10^{-16}s^{-1}H^{-1}$, instead of their rate $\xi_H = 10^{-17}s^{-1}H^{-1}$, these reactions, especially the recombination of C^+ on dust grains, are essential for CO formation at moderate densities $n \lesssim 1000\ cm^{-3}$. This is because electrons from cosmic-ray ionization of H and C inhibit CO formation, while He^+ formed by cosmic rays destroys CO.

3. Cosmic-ray ionization of H and H_2 by secondary electrons. The measurement of cosmic-ray ionization rate $\xi_H = 2.0 \times 10^{-16}s^{-1}H^{-1}$ in Indriolo et al. (2007) (ξ_p in their paper) only accounts for the initial (primary) cosmic-ray ionization. The secondary electrons created by the first ionization event can again ionize H and H_2. The secondary ionization rate depends on factors such as electron abundance (Dalgarno et al., 1999). Here we apply a simple approach motivated by Glassgold & Langer (1974), which has the total ionization rate of H 1.5 times the primary rate in atomic regions and 1.15 times in molecular regions. In regions mixed with atomic and molecular gas, we simply scale the total rate with H and H_2 abundance as shown in reactions 6 and 7 in Table A.2. The cosmic-ray ionization rate of H_2 is simply twice that of H.

4. Removed photodissociation of HCO^+. We find that the destruction of HCO^+ is dominated by the reaction $HCO^+ + e \rightarrow CO + H$, and the photodissociation of HCO^+ has very little effect on the whole chemistry network.

5. He^+ destruction in the H_2 region:

$$He^+ + H_2 \rightarrow H_2^+ + He$$
$$He^+ + H_2 \rightarrow H^+ + He + H$$

The rates of these two reactions are similar to the rate of direct recombination of He^+ with electrons, and can be higher than the grain surface recombination of He^+ abundance at low metallicities.

6. CH destruction:

$$CH + H \rightarrow H_2 + C$$

This is one of the main destruction channels of CH in shielded regions.

7. Cosmic-ray ionization, and cosmic-ray induced photodissociation of C and CO:

$$cr + C \rightarrow C^+ + e$$

$$cr + CO \rightarrow CO^+ + e$$

$$\gamma_{cr} + C \rightarrow C^+ + e$$

$$\gamma_{cr} + CO \rightarrow C + O$$

For $cr + CO \rightarrow CO^+ + e$, we assume that CO^+ reacts quickly with H/H_2 to form HCO^+, and implement the reaction as $cr + CO + H \rightarrow HCO^+ + e$ with the same rate. Similar to Clark & Glover (2015), the rates for these reactions are assumed to be proportional to the cosmic-ray ionization rate of atomic hydrogen ξ_H. The scaling factors for cosmic-ray ionization $\xi_{C,CO}/\xi_H$ are calculated with the rates in McElroy et al. (2013), and the scaling factors for cosmic-ray induced photo-ionization are adopted from Gredel et al. (1987). We also scale the cosmic-ray induced photo-ionization to the H_2 fraction $2n(H_2)/(2n(H_2) + 2n(H))$, because the ionizing photons come from the UV light induced by the primary ionization and excitation of H_2, and would not be present in regions with only atomic hydrogen. We have also tested the inclusion of cosmic-ray induced photo-reactions of CH and OH using the rates in Gredel et al. (1989), but found they made very little difference for CO formation.

8. $OH_x + O \rightarrow 2O + H$. This reaction can be important for OH_x destruction in dense and shielded regions, where photodissociation of OH_x is less efficient. See OH_x pseudo-reactions in Appendix A.3.

9. $He^+ + OH_x \rightarrow O^+ + He + H$: This can be the major channel for He^+ destruction in shielded regions. See Appendix A.3.

10. $C^+ + H_2 + e \rightarrow C + 2H$. See the $C^+ + H_2$ reaction in Appendix A.2. Note that this is not a three-body reaction but a pseudo-reaction representing a two-body reaction followed by a recombination.

11. H_2O^+ destruction by reacting with electrons:

$$H_2O^+ + e \rightarrow 2H + O$$

In regions where electron abundance is relatively high, this can be limiting for the abundance of OH_x species. This is applied implicitly as the branching ratio for OH_x formation in reactions 2-5 in Table A.1. See Appendix A.3 for details.

12. O^+ species and reactions:

$$H^+ + O \rightarrow O^+ + H$$
$$O^+ + H \rightarrow H^+ + O$$

In high temperature regions, the first reaction has a higher rate than the second one (its reverse reaction). O^+ formed by change exchange with H^+ can react with H_2, and subsequently from OH^+. See Appendix A.3.

13. Si, Si^+ species and reactions:

$$Si^+ + e \rightarrow Si$$

$$Si^+ + e + gr \rightarrow Si + gr$$

$$\gamma_{cr} + Si \rightarrow Si^+ + e$$

$$\gamma + Si \rightarrow Si^+ + e$$

The NL99 network include species M to represent the metals besides C and O. However, the metal abundance they are using, $x_{M,tot} = 2 \times 10^{-7}$, is much lower than the observed abundances in the solar neighborhood: the most abundant gas-phase metals are S and Si, with $x_{S,tot} = 3.5 \times 10^{-6}$ (Jenkins, 2009), and $x_{Si,tot} = 1.7 \times 10^{-6}$ (Cardelli et al., 1994). Because the dust-shielding factor $\gamma_{Si} < \gamma_C$ (see Equation (2.2) and Table A.2), at $A_V \sim 1$, Si^+ can be the main agent for providing electrons where C is already shielded from photo-ionization (see e.g., Figure C.3). Although the total abundance of S is higher than Si, we find that including S and S^+ has very little effect on the electron or CO abundances, since $\gamma_S \approx \gamma_C$. Therefore, we only include Si and Si^+ for the metals.

A.2 CH_x Pseudo-reactions

The pseudo-species CH_x includes CH, CH_2, CH^+, CH_2^+, and CH_3^+. The creation of CH_x is from two reactions. The first one is

$$H_3^+ + C \rightarrow CH_x + H_2.$$

This represents the sum of two reactions: $H_3^+ + C \rightarrow CH^+ + H_2$, and $H_3^+ + C \rightarrow CH_2^+ + H$. We use the sum of both rates for this pseudo-reaction. CH^+ reacts with H_2 to form CH_2^+

and H, and CH_2^+ again reacts with H_2 to form CH_3^+ and H. The second one,

$$C^+ + H_2 \rightarrow CH_x + H,$$

represents the reaction of $C^+ + H_2 \rightarrow CH_2^+$. CH_2^+ quickly reacts with H_2 and turns into CH_3^+ and H, which then reacts with an electron. 70% of the reaction $CH_3^+ + e$ gives CH or CH_2, and 30% turns back into C. Therefore, we use the rate in Wakelam et al. (2010) multiplied by 0.7 for $C^+ + H_2 \rightarrow CH_x + H$, and by 0.3 for $C^+ + H_2 + e \rightarrow C + 2H$.

The recombinations of CH^+, CH_2^+, and CH_3^+ with electrons form CH and CH_2, which can be destroyed in three pathways:

$$CH_x + O \rightarrow CO + H$$

$$CH_x + H \rightarrow C + H_2$$

$$\gamma + CH_x \rightarrow C + H$$

For the reaction $CH_x + O \rightarrow CO + H$, CH and CH_2 have similar rates. Here we use the rate of CH. For the reactions $CH_x + H \rightarrow C + H_2$ and $\gamma + CH_x \rightarrow C + H$, CH_2 will react with H to form CH and with a photon to form CH and CH_2^+. Therefore, we again use the rate assuming CH_x are all in CH.

A.3 OH_x Pseudo-reactions

The pseudo-species OH_x represents OH, H_2O, OH^+, H_2O^+, H_3O^+. The formation of OH_x is mainly through

$$H_3^+ + O \rightarrow OH_x + H_2 \tag{A.1}$$

This represents two reactions, the formation of OH^+ and H_2O^+. The sum of both rates gives the rate of this pseudo-reaction. Another channel for OH_x formation is

$$O^+ + H_2 \rightarrow OH_x + H, \tag{A.2}$$

and this represents the reaction $O^+ + H_2 \rightarrow OH^+ + H$. O^+ mainly comes from the charge exchange $O + H^+ \rightarrow O^+ + H$.

OH^+ formed by the two channels above reacts with H_2 to form H_2O^+. The H_2O^+ molecule has two fates: it can again react with H_2 to form H_3O^+:

$$H_2O^+ + H2 \rightarrow H_3O^+ + H,\ k_{H_2O^+,H_2} = 6.0 \times 10^{-10} \mathrm{cm^3 s^{-1}},$$

and then H_3O^+ combines with electrons, eventually forming more stable OH and H_2O. Or, the H_2O^+ molecule can be destroyed by electrons:

$$H_2O^+ + e \rightarrow 2H + O,\ k_{H_2O^+,e} = 5.3 \times 10^{-6} T^{-0.5} \mathrm{cm^3 s^{-1}}. \tag{A.3}$$

At low density and low A_V regions where H_2 abundance is low and electron abundance is high, H_2O^+ destruction by Equation (A.3) can limit the formation of OH_x by Equations (A.1) and (A.2). Therefore, we multiply the reaction rates of Equations (A.1) and (A.2) by a branching factor $r = k_{H_2O^+,H_2} x_{H_2} / (k_{H_2O^+,H_2} x_{H_2} + k_{H_2O^+,e} x_e)$, and also add the reactions 3 and 5 in Table A.1, which is equivalent to the combined reactions of Equations (A.1) and (A.2) with Equation (A.3).

We assume most OH_x are in OH, and use the rate of OH reactions for the following pseudo-reactions of OH_x destruction:

$$C^+ + OH_x \rightarrow HCO^+$$

$$OH_x + C \rightarrow CO + H$$

$$\gamma + OH_x \rightarrow O + H$$

$$OH_x + O \rightarrow 2O + H$$

$$He^+ + OH_x \rightarrow O^+ + He + H$$

For the reaction $C^+ + OH_x \rightarrow HCO^+$, we use the rate of $C^+ + OH \rightarrow CO^+ + H$, because CO^+ will quickly react with H_2 to form HCO^+. We use the rate of reaction $OH + O \rightarrow O_2 + H$ for $OH_x + O \rightarrow 2O + H$, assuming most oxygen will be in the form of atomic O.

Table A.1: List of Collisional Chemical Reactions

No.	Reaction	Rate Coefficient[a]	Notes	Reference[b]
1	$H_3^+ + C \rightarrow CH_x + H_2$	$1.04 \times 10^{-9}(300/T)^{0.00231}+$	$H_3^+ + C \rightarrow CH^+ + H_2$	1
		$T^{3/2}\Sigma_{i=1}^{4} c_i \exp(-T_i/T)$	and $H_3^+ + C \rightarrow CH_2^+ + H$	
		$c_i = [3.40 \times 10^{-8}, 6.97 \times 10^{-9}, 1.31 \times 10^{-7}, 1.51 \times 10^{-4}]$		
		$T_i = [7.62, 1.38, 2.66 \times 10^{1}, 8.11 \times 10^{3}]$		
2	$H_3^+ + O \rightarrow OH_x + H_2$	$1.99 \times 10^{-9} T^{-0.190} \times r$		20
3	$H_3^+ + O + e \rightarrow H2 + O + H$	$1.99 \times 10^{-9} T^{-0.190} \times (1 - r)$	$H_2O^+ + e \rightarrow 2H + O$	20
4	$O^+ + H_2 \rightarrow OH_x + H$	$1.6 \times 10^{-9} \times r$		22
5	$O^+ + H_2 + e \rightarrow O + H + H$	$1.6 \times 10^{-9} \times (1 - r)$		22
		$r = k_{H_2O^+,H_2} x_{H_2} / (k_{H_2O^+,H_2} x_{H_2} + k_{H_2O^+,e} x_e)$	see Appendix A.3	
		$k_{H_2O^+,H_2} = 6.0 \times 10^{-10}$		22
		$k_{H_2O^+,e} = 5.3 \times 10^{-6} T^{-0.5}$		22
6	$H_3^+ + CO \rightarrow HCO^+ + H_2$	1.7×10^{-9}		2
7	$He^+ + H_2 \rightarrow H^+ + He + H$	$1.26 \times 10^{-13} \exp\left(-\frac{22.5}{T}\right)$		26
8	$He^+ + CO \rightarrow C^+ + O + He$	1.6×10^{-9}		4, 5
9	$C^+ + H_2 \rightarrow CH_x + H$	$2.31 \times 10^{-13} T^{-1.3} \exp(-\frac{23}{T})$	$C^+ + H_2 \rightarrow CH_2^+$	22
10	$C^+ + H_2 + e \rightarrow C + H + H$	$0.99 \times 10^{-13} T^{-1.3} \exp(-\frac{23}{T})$	$C^+ + H_2 \rightarrow CH_2^+$	22
11	$C^+ + OH_x \rightarrow HCO^+$	$9.15 \times 10^{-10}(0.62 + 45.41 T^{-1/2})$	$C^+ + OH \rightarrow CO^+ + H$	22

List of Collisional Chemical Reactions (continued)

No.	Reaction	Rate Coefficient[a]	Notes	Reference[b]
12	$CH_x + O \rightarrow CO + H$	7.7×10^{-11}	$CH + O \rightarrow CO + H$	22
13	$OH_x + C \rightarrow CO + H$	$7.95 \times 10^{-10} T^{-0.339} \exp(\frac{0.108}{T})$	$OH + C \rightarrow CO + H$	21, 22
14	$He^+ + e \rightarrow He$	$10^{-11} T^{-0.5} \times [11.19$	Case B	6, 7
		$- 1.676 \log T - 0.2852 (\log T)^2 + 0.04433 (\log T)^3]$		
15	$H_3^+ + e \rightarrow H_2 + H$	$4.54 \times 10^{-7} T^{-0.52}$		8
16	$H_3^+ + e \rightarrow 3H$	$8.46 \times 10^{-7} T^{-0.52}$		8
17	$C^+ + e \rightarrow C$	$k_{rr} = \frac{2.995 \times 10^{-9}}{\alpha (1.0+\alpha)^{1.0-\gamma} (1.0+\beta)^{1.0+\gamma}}$	Radiative and	9, 23, 27
		$k_{dr} = T^{-3/2} \times [6.346 \times 10^{-9} \exp(\frac{-12.17}{T})$	dielectronic recombination	
		$+ 9.793 \times 10^{-9} \exp(\frac{-73.8}{T}) + 1.634 \times 10^{-6} \exp(\frac{-15230}{T})]$		
		$k = k_{rr} + k_{dr},\ \alpha \equiv \sqrt{\frac{T}{6.670 \times 10^{-3}}},\ \beta \equiv \sqrt{\frac{T}{1.943 \times 10^{6}}},$		
		$\gamma \equiv 0.7849 + 0.1597 \exp(\frac{-49550}{T})$		
18	$HCO^+ + e \rightarrow CO + H$	$1.06 \times 10^{-5} T^{-0.64}$		10
19	$H_2^+ + H_2 \rightarrow H_3^+ + H$	$2.84 \times 10^{-9} T^{0.042} \exp\left(-\frac{T}{46600}\right)$		7, 11
20	$H_2^+ + H \rightarrow H^+ + H_2$	6.4×10^{-10}		22
21	$H^+ + e \rightarrow H$	$2.753 \times 10^{-14} \left(\frac{315614}{T}\right)^{1.500} \left[1.0 + \left(\frac{115188}{T}\right)^{0.407}\right]^{-2.242}$	Case B	7, 12
22	$H_2 + H \rightarrow 3H$	$k_{16,l} = 6.67 \times 10^{-12} \sqrt{T} \exp\left[-\left(1.0 + \frac{63590}{T}\right)\right]$	Density dependent, see	13, 14
		$k_{16,h} = 3.52 \times 10^{-9} \exp\left(-\frac{43900}{T}\right)$	Glover & Mac Low (2007)	13, 15

List of Collisional Chemical Reactions (continued)

No.	Reaction	Rate Coefficient[a]	Notes	Reference[b]
		$n_{\rm cr,H} = {\rm dex}[3.0 - 0.416 \log T_4 - 0.327 (\log T_4)^2]$		13, 15, 16
		$n_{\rm cr,H_2} = {\rm dex}[4.845 - 1.3 \log T_4 + 1.62 (\log T_4)^2]$		13, 17
23	$H_2 + H_2 \rightarrow H_2 + 2H$	$k_{17,l} = \frac{5.996 \times 10^{-30} T^{4.1881}}{(1.0 + 6.761 \times 10^{-6} T)^{5.6881}} \exp\left(\frac{-54657.4}{T}\right)$	Density dependent, see	13, 18
		$k_{17,h} = 1.3 \times 10^{-9} \exp\left(-\frac{53300}{T}\right)$	Glover & Mac Low (2007)	13, 17
24	$H + e \rightarrow H^+ + 2e$	$\exp[-3.271396786 \times 10^1 + 1.35365560 \times 10^1 \ln T_e$		19
		$- 5.73932875 (\ln T_e)^2 + 1.56315498 (\ln T_e)^3$		
		$- 2.877056 \times 10^{-1} (\ln T_e)^4$		
		$+ 3.48255977 \times 10^{-2} (\ln T_e)^5$		
		$- 2.63197617 \times 10^{-3} (\ln T_e)^6$		
		$+ 1.11954395 \times 10^{-4} (\ln T_e)^7$		
		$- 2.03914985 \times 10^{-6} (\ln T_e)^8]$		
25	$He^+ + H_2 \rightarrow H_2^+ + He$	7.20×10^{-15}		3, 4
26	$CH_x + H \rightarrow H_2 + C$	$2.81 \times 10^{-11} T^{0.26}$		22
27	$OH_x + O \rightarrow 2O + H$	3.5×10^{-11}	$OH + O \rightarrow O_2 + H$	24
28	$Si^+ + e \rightarrow Si$	$1.46 \times 10^{-10} T^{-0.62}$		4
29	$He^+ + OH_x \rightarrow O^+ + He + H$	$1.35 \times 10^{-9} (0.62 + 45.41 T^{-1/2})$		22
30	$H^+ + O \rightarrow O^+ + H$	$(1.1 \times 10^{-11} T^{0.517} + 4.0 \times 10^{-10} T^{0.00669}) \exp\left(\frac{-227}{T}\right)$		25

List of Collisional Chemical Reactions (continued)

No.	Reaction	Rate Coefficient[a]	Notes	Reference[b]
31	$O^+ + H \rightarrow H^+ + O$	$4.99 \times 10^{-11} T^{0.405} + 7.5 \times 10^{-10} T^{-0.458}$		25

[a] Rate coefficients are in units of $cm^3 s^{-1}$. The temperature T is in Kelvin, and $T_4 = T/(10^4 K)$. T_e is temperature in the unit of eV/k where k is the Boltzmann constant, i.e., $T_e = 8.6173 \times 10^{-5} T$. $x_i = n_i/n$ is the abundance of species i. χ is the flux of the incident radiation field in $6 - 13.6$eV relative to the standard radiation field ($\chi = 1$, $J_{FUV} = 2.7 \times 10^{-3}$erg $cm^{-2} s^{-1}$) in Draine (1978) units. This field has a strength of $G_0 = 1.7$ in Habing (1968) units. A_V is the visual extinction.

[b] References: (1)Vissapragada et al. (2016), (2)Kim et al. (1975), (3)Barlow (1984), (4)McElroy et al. (2013), (5)Anicich & Huntress (1986), (6)Hummer & Storey (1998), (7)Glover et al. (2010), (8)Fit by Woodall et al. (2007) to data from McCall et al. (2004), (9)Badnell et al. (2003) (Fitting coefficients are taken for $T \lesssim 10^4$ K from their website http://amdpp.phys.strath.ac.uk/tamoc/DR/), (10)Geppert et al. (2005), (11)Linder et al. (1995) (12)Ferland et al. (1992), (13)Glover & Mac Low (2007), (14)Mac Low & Shull (1986), (15)Lepp & Shull (1983), (16)Martin et al. (1996), (17)Shapiro & Kang (1987), (18)Martin et al. (1998), (19)Janev et al. (1987), (20)Fit to de Ruette et al. (2016), accurate to $\sim 10\%$ at $T = 10 - 1000$K, (21)Zanchet et al. (2009), (22)Wakelam et al. (2010), (23)Badnell (2006), (24)Carty et al. (2006), (25)Stancil et al. (1999), (26)Fit to Schauer et al. (1989), (27)Bryans et al. (2009).

Table A.2: List of Grain-assisted Reactions, Cosmic-ray Reactions, and Photodissociation Reactions

No.	Reaction	Rate coefficient[a]	Notes	Reference[b]
Grain-assisted reactions:				
1	$H + H + gr \rightarrow H_2 + gr$	3.0×10^{-17}		1, 2
2	$H^+ + e + gr \rightarrow H + gr$	$12.25 \times 10^{-14}[1 + 8.074 \times 10^{-6}\psi^{1.378}\times$ $(1 + 508.7T^{0.01586}\psi^{-0.4723-1.102\times10^{-5}\ln T})]^{-1}$		3, 4
3	$C^+ + e + gr \rightarrow C + gr$	$45.58 \times 10^{-14}[1 + 6.089 \times 10^{-3}\psi^{1.128}\times$ $(1 + 433.1T^{0.04845}\psi^{-0.8120-1.333\times10^{-4}\ln T})]^{-1}$		3
4	$He^+ + e + gr \rightarrow He + gr$	$5.572 \times 10^{-14}[1 + 3.185 \times 10^{-7}\psi^{1.512}\times$ $(1 + 5115T^{3.903\times10^{-7}}\psi^{-0.4956-5.494\times10^{-7}\ln T})]^{-1}$		3
5	$Si^+ + e + gr \rightarrow Si + gr$	$2.166 \times 10^{-14}[1 + 5.678 \times 10^{-8}\psi^{1.874}\times$ $(1 + 43750T^{1.635\times10^{-6}}\psi^{-0.8964-7.538\times10^{-5}\ln T})]^{-1}$ $\psi \equiv \frac{1.7\chi\exp(-1.87A_V)\sqrt{T}}{n_e/\mathrm{cm}^{-3}}$		3

List of Grain-assisted Reactions, Cosmic-ray Reactions, and Photodissociation Reactions (continued)

No.	Reaction	Rate Coefficient[a]	Notes	Reference[b]
Cosmic-ray ionization or cosmic-ray induced photodissociation:				
6	$\mathrm{cr} + \mathrm{H} \rightarrow \mathrm{H}^+ + \mathrm{e}$	$2.3x_{\mathrm{H_2}} + 1.5x_{\mathrm{H}}$	primary and	8
7	$\mathrm{cr} + \mathrm{H_2} \rightarrow \mathrm{H_2^+} + \mathrm{e}$	$2 \times (2.3x_{\mathrm{H_2}} + 1.5x_{\mathrm{H}})$	secondary ionization	8
8	$\mathrm{cr} + \mathrm{He} \rightarrow \mathrm{He}^+ + \mathrm{e}$	1.1		5, 6
9	$\mathrm{cr} + \mathrm{C} \rightarrow \mathrm{C}^+ + \mathrm{e}$	3.85		5, 6
10	$\mathrm{cr} + \mathrm{CO} + \mathrm{H} \rightarrow \mathrm{HCO}^+ + \mathrm{e}$	6.52	$\mathrm{cr} + \mathrm{CO} \rightarrow \mathrm{CO}^+ + \mathrm{e}$	5, 6
11	$\gamma_{\mathrm{cr}} + \mathrm{C} \rightarrow \mathrm{C}^+ + \mathrm{e}$	560		7
12	$\gamma_{\mathrm{cr}} + \mathrm{CO} \rightarrow \mathrm{C} + \mathrm{O}$	90		7
13	$\gamma_{\mathrm{cr}} + \mathrm{Si} \rightarrow \mathrm{Si}^+ + \mathrm{e}$	8400		7
Photoionization and photodissociation reactions[c]				
14	$\gamma + \mathrm{C} \rightarrow \mathrm{C}^+ + \mathrm{e}$	$3.5 \times 10^{-10}\chi \exp(-3.76A_V) f_{s,\mathrm{C}}(N_{\mathrm{C}}, N_{\mathrm{H_2}})$		7, 9
15	$\gamma + \mathrm{CH_x} \rightarrow \mathrm{C} + \mathrm{H}$	$9.1 \times 10^{-10}\chi \exp(-2.12A_V)$	$\gamma + \mathrm{CH} \rightarrow \mathrm{C} + \mathrm{H}$	7
16	$\gamma + \mathrm{CO} \rightarrow \mathrm{C} + \mathrm{O}$	$2.4 \times 10^{-10}\chi \exp(-3.88A_V) f_{s,\mathrm{CO}}(N_{\mathrm{CO}}, N_{\mathrm{H_2}})$		7, 10
17	$\gamma + \mathrm{OH_x} \rightarrow \mathrm{O} + \mathrm{H}$	$3.8 \times 10^{-10}\chi \exp(-2.66A_V)$	$\gamma + \mathrm{OH} \rightarrow \mathrm{O} + \mathrm{H}$	7
18	$\gamma + \mathrm{Si} \rightarrow \mathrm{Si}^+ + \mathrm{e}$	$4.5 \times 10^{-9}\chi \exp(-2.61A_V)$		7
19	$\gamma + \mathrm{H_2} \rightarrow \mathrm{H} + \mathrm{H}$	$5.7 \times 10^{-11}\chi \exp(-4.18A_V) f_{s,\mathrm{H_2}}(N_{\mathrm{H_2}})$		7, 11

List of Grain-assisted Reactions, Cosmic-ray Reactions, and Photodissociation Reactions (continued)

No.	Reaction	Rate Coefficient[a]	Notes	Reference[b]

[a] Rate coefficients are in units of $\mathrm{cm^3 s^{-1}} Z_d^{-1}$ for grain-assisted reactions, where Z_d is the dust abundance relative to the solar neighbourhood (the reaction rates for grain-assisted reactions are $x_i n k_{\mathrm{gr}}$, where k_{gr} is the listed rate coefficient, and $x_i = x_{\mathrm{H_2}}$ for reaction 1 and $x_i = x_{\mathrm{ion}}$ for reactions 2-5); ξ_{H} for cosmic-ray ionization where $\xi_{\mathrm{H}} = 2.0 \times 10^{-16} \mathrm{s^{-1} H^{-1}}$ is the local primary cosmic-ray ionization rate for atomic H per H atom (Indriolo et al., 2007); and $\mathrm{s^{-1}}$ for photoreactions. n_{e} is the number density of electrons. $x_i = n_i/n$ is the abundance of species i. χ is the flux of the incident radiation field in $6 - 13.6$eV relative to the standard radiation field ($\chi = 1$, $J_{\mathrm{FUV}} = 2.7 \times 10^{-3}$erg $\mathrm{cm^{-2} s^{-1}}$) in Draine (1978). This field has a strength of $G_0 = 1.7$ in Habing (1968) units. A_V is the visual extinction.

[b] References: (1) Wolfire et al. (2008), (2)Hollenbach et al. (2012), (3)Weingartner & Draine (2001a), (4)Draine (2003), (5)Glover et al. (2010), (6)Le Teuff et al. (2000), (7)Heays et al. (2017), (8)Glassgold & Langer (1974), (9)Tielens & Hollenbach (1985), (10)Visser et al. (2009), (11)Draine & Bertoldi (1996).

[c] The self-shielding of $\mathrm{H_2}$ and self-shielding plus shielding from $\mathrm{H_2}$ of CO and C are included in the factors $f_{s,\mathrm{H_2}}(N_{\mathrm{H_2}})$, $f_{s,\mathrm{CO}}(N_{\mathrm{CO}}, N_{\mathrm{H_2}})$, and $f_{s,\mathrm{C}}(N_{\mathrm{C}}, N_{\mathrm{H_2}})$. This is described in detail in Section 2.1.1.

Appendix B

Heating and Cooling Processes

A summary of all the heating and cooling processes is listed in Table B.1.

B.1 Heating

B.1.1 Cosmic-Ray Ionization

When the gas is ionized by cosmic rays, the primary and secondary electrons thermalize with and heat up the gas. The heating rate per H,

$$\Gamma_{\rm cr} = \xi q_{\rm cr}, \tag{B.1}$$

where $\xi = \xi_{\rm H} x({\rm H}) + \xi_{\rm H_2} x({\rm H_2}) + \xi_{\rm He} x({\rm He})$, and $q_{\rm cr}$ is the energy added to the gas per primary ionization. We use the result fitted by Draine (2011) to the data of Dalgarno & McCray (1972) in atomic regions:

$$q_{\rm cr,H} = 6.5 + 26.4 \left(\frac{x({\rm e})}{x(e) + 0.07} \right)^{0.5} \ {\rm eV}, \tag{B.2}$$

and the fit by Krumholz (2014) to the data of Glassgold et al. (2012) in molecular regions:

$$\frac{q_{\rm cr,H_2}}{\rm eV} = \begin{cases} 10, & \log n < 2 \\ 10 + \frac{3(\log n - 2)}{2}, & 2 \leq \log n < 4 \\ 13 + \frac{4(\log n - 4)}{3}, & 4 \leq \log n < 7 \\ 17 + \frac{\log n - 7}{3}, & 7 \leq \log n < 10 \\ 18, & \log n \geq 10 \end{cases} . \tag{B.3}$$

Similar to Krumholz (2014), we simply assume that the total heating rate can be calculated by summing the heating rates in the atomic and molecular regions weighted by their number fraction:

$$q_{\rm cr} = x({\rm H}) q_{\rm cr,H} + 2x({\rm H_2}) q_{\rm cr,H_2}. \tag{B.4}$$

B.1.2 Photoelectric Effect on Dust Grains

One main heating source in the ISM comes from the photoelectric effect on dust grains, where electrons ejected from dust grains by FUV radiation thermalize with the gas. We use the results in Weingartner & Draine (2001a) Equation (44) to calculate the heating from the photoelectric effect on dust grains. The rates are extracted from their Table 2, using the values for $R_v = 3.1$, $b_c = 4.0$, and radiation field with ISRF spectrum.

B.1.3 H_2 Formation on Dust Grains, and UV Pumping of H_2

We follow Hollenbach & McKee (1979), using their Equation (6.43) for heating from H_2 formation on dust grains and their Equation (6.46) for UV pumping of H_2. Both processes are more efficient at higher densities. The rate of H_2 formation on grains increases with density. For UV pumping, the energy is initially in the excited rotational/vibrational levels of H_2, and subsequently turns into heat by collisional de-excitation.

B.1.4 H_2 Photodissociation

The photodissociation of H_2 releases ~ 0.4eV heat per reaction (Black & Dalgarno, 1977; Hollenbach & McKee, 1979).

B.2 Cooling

B.2.1 Atomic lines: C^+, C, and O Fine Structure lines, and the Lyα line

To calculate atomic line cooling, C^+ and H (Lyα) are considered as two-level systems, and C and O as three-level systems. The calculation of level populations follows the standard procedure, including collisional excitation and de-excitation, photoabsorption, and spontaneous and stimulated emission (e.g. Draine, 2011). The species considered for collisional excitation and de-excitation are listed in Table B.1.

B.2.2 CO Rotational Lines

The CO rotational lines are often optically thick in regions where CO cooling is important. To calculate the cooling rate by CO rotational lines, we use the cooling functions in Omukai et al. (2010) (their Appendix C and Table B2). They use the large velocity gradient (LVG) approximation, similar to the approach by Neufeld & Kaufman (1993). The cooling rate per H is given by

$$\Gamma_{\rm CO} = L_{\rm CO} x({\rm CO}) n_{\rm H_2} \tag{B.5}$$

where $L_{\rm CO}$ is given in terms of $n_{\rm H_2}$, $\tilde{N}({\rm CO})$, and T by Equation (B1) in Omukai et al. (2010). In Neufeld & Kaufman (1993) and Omukai et al. (2010), they assume H_2 is the only species responsible for the collisional excitation of the CO rotational levels, which is appropriate in fully molecular regions. To take into account of the collisional excitation by atomic hydrogen and electrons, we replace $n_{\rm H_2}$ in Equation (B.5) with an effective number density, following

Yan (1997), Meijerink & Spaans (2005) and Glover et al. (2010):

$$n_{\rm eff,CO} = n_{\rm H_2} + \sqrt{2}\left(\frac{\sigma_{\rm H}}{\sigma_{\rm H_2}}\right) n + \left(\frac{1.3\times10^{-8}\ {\rm cm^3 s^{-1}}}{\sigma_{\rm H_2} v_{\rm e}}\right) n_{\rm e}, \tag{B.6}$$

where $\sigma_{\rm H} = 2.3\times10^{-15}$ cm^2, $\sigma_{\rm H_2} = 3.3\times10^{-16}(T/1000{\rm K})^{-1/4}$ cm^2 and $v_{\rm e} = 1.03\times10^4(T/1{\rm K})^{1/2}$ cm s^{-1}.

In LVG approximation , the escape probability of a photon emitted by CO is related to the effective column density parameter

$$\tilde{N}({\rm CO}) = \frac{n({\rm CO})}{|\nabla v|}, \tag{B.7}$$

where n(CO) is the local CO number density and ∇v is the local gas velocity gradient. In Omukai et al. (2010), they used the approximation $\tilde{N}({\rm CO}) = N({\rm CO})/\sqrt{2kT/m({\rm CO})}$, where T is the gas temperature, N(CO) the total CO column density, and m(CO) the mass of a single CO molecule. This assumes thermal motions dominate the velocity of CO molecules. However, in realistic molecular clouds, the gas velocity will be largely determined by the supersonic turbulence. For Milky Way molecular clouds, the observed turbulence spectrum obeys the line-width size relation (Larson, 1981; Solomon et al., 1987; Heyer & Brunt, 2004):

$$v(L) \sim 1\ {\rm km/s}\ \left(\frac{L}{\rm pc}\right)^{1/2}. \tag{B.8}$$

In our slab models, we use the velocity determined using Equation (B.8) to calculate the effective CO column density parameter $\tilde{N}({\rm CO}) = N({\rm CO})/v(L)$, where N(CO) is the column density of CO from the local position to the edge of the one-sided slab. This assumes that for thicker clouds, the global turbulent velocity will be larger as implied by Equation (B.8). We have also tried using a constant velocity $v = 1$km/s to calculate $\tilde{N}$, and the results for the equilibrium temperature in CO-dominated regions are very similar.

Care needs to be taken when the temperature $T < 10$K. Omukai et al. (2010) only gives fitting parameters down to $T = 10$K, and naive extrapolation may give a finite cooling rate even when the temperature is close to zero. Moreover, CO can freeze-out onto dust grains in regions with high density and $T \lesssim 10$K, leading to depleted CO abundance (Bergin et al., 1995; Acharyya et al., 2007). For simplicity, we artificially turn off CO cooling at temperatures below 10K. Omukai et al. (2010) also only gives fitting parameters up to $T = 2000$K. For $T > 2000$K, we simply use the CO cooling rate at $T = 2000$K. In reality, CO will likely be destroyed by collisional dissociation and ionization at such high temperatures.

B.2.3 H_2 Rotational and Vibrational Lines

We use the results in Glover & Abel (2008) to calculate cooling by H_2 rotational and vibrational lines. The cooling rate per H_2 molecule Λ_{H_2} is approximated by

$$\Lambda_{H_2} = \frac{\Lambda_{H_2,\mathrm{LTE}}}{1 + \Lambda_{H_2,\mathrm{LTE}}/\Lambda_{H_2,\mathrm{n}\to 0}}, \tag{B.9}$$

where $\Lambda_{H_2,\mathrm{LTE}}$ is the cooling rate at high densities when H_2 level populations are in local thermal equilibrium, and $\Lambda_{H_2,\mathrm{n}\to 0}$ is the cooling rate in the low density limit. We use Equations (6.37) and (6.38) in Hollenbach & McKee (1979) to calculate $\Lambda_{H_2,\mathrm{LTE}} = \Lambda_{H_2,\mathrm{LTE,rot}} + \Lambda_{H_2,\mathrm{LTE,vib}}$ for H_2 rotational and vibrational lines. $\Lambda_{H_2,\mathrm{n}\to 0}$ is obtained by the fitting functions provided in Glover & Abel (2008), including collisional species H, H_2, He, H^+, and e. We use the fitting parameters in their Table 8, assuming a fixed ortho-to-para ratio of H_2 of 3:1. Glover & Abel (2008) only gives the fit for H_2 cooling in the temperature range $20\mathrm{K} < T < 6000\mathrm{K}$. Similar to the treatment in CO rotational line cooling, we artificially cut off H_2 cooling below 10K, and use the H_2 cooling rate at $T = 6000$K for $T > 6000$K. In reality, H_2 cooling rate is likely to be negligible at $T < 10$K.

B.2.4 Dust Thermal Emission

By exchanging energy with dust via collision, gas can either heat or cool. The rate of gas–dust energy exchange is given by (Krumholz, 2014):

$$\Psi_{\rm gd} = \alpha_{\rm gd} n Z_{\rm d} T_{\rm g}^{1/2} (T_{\rm d} - T_{\rm g}), \tag{B.10}$$

where Z_d is the dust abundance relative to the Milky Way, and $\alpha_{\rm gd}$ the dust–gas coupling coefficient. Positive $\Psi_{\rm gd}$ means heating of the gas, and negative means cooling of the gas. In the realistic ISM, dust almost always acts to cool the ISM with $T_{\rm d} < T_{\rm g}$. We use $\alpha_{\rm gd} = 3.2 \times 10^{-34}$erg s^{-1}cm^{3}K$^{-3/2}$ for H_2-dominated regions (Goldsmith, 2001). $\alpha_{\rm gd}$ is expected to be a factor ~ 3 higher in H-dominated regions (Krumholz et al., 2011), but dust cooling is likely to be only important in dense regions dominated by H_2.

The dust temperature $T_{\rm d}$ necessary for evaluating $\Psi_{\rm gd}$ is determined by the total rate of change of dust specific energy per H nucleus (Krumholz, 2014):

$$\frac{{\rm d}e_{\rm d,sp}}{{\rm d}t} = \Gamma_{\rm ISRF} + \Gamma_{\rm d,line} + \Gamma_{\rm d,CMB} + \Gamma_{\rm d,IR} - \Lambda_{\rm d} - \Psi_{\rm gd} \tag{B.11}$$

Because the dust specific heat is very small compared to the gas, we can always assume the dust temperature is in equilibrium, ${\rm d}e_{\rm d,sp}/{\rm d}t = 0$. Note that for very small dust with size $a \lesssim 10$Å, they are not in thermal equilibrium, and can have temperature spikes (Draine, 2011). Here we mainly consider bigger grains. In principle, given all the terms in Equation (B.11), one can solve for $T_{\rm d}$. However, because Equation (B.11) is a non-linear function of $T_{\rm d}$, this procedure will involve a costly root-finding algorithm. For the purposes of this work, we assume a fixed dust temperature $T_{\rm d} = 10$ K. In the density range $n < 10^4$ cm^{-3} that we consider, dust cooling is never important and contributes to less than $\sim 5\%$ of the total cooling rate.

B.2.5 Recombination of e on PAHs

At high temperatures $T \sim 10^3 - 10^4$K, cooling by electron recombination on PAHs can be important relative to the photoelectric heating on dust. Following Weingartner & Draine (2001a) Equation (45), we use the parameters in their Table 3 ($R_v = 3.1$, $b_c = 4.0$, ISRF) to calculate the cooling rate from electron recombination on PAHs.

B.2.6 Collisional Dissociation of H_2 and Collisional Ionization of H

The collisional dissociation of H_2 and ionization of H takes 4.48eV and 13.6eV energy per reaction (Grassi et al., 2014).

Table B.1: List of Heating and Cooling Processes

Process	Reference
Heating:	
Cosmic-ray ionization of H, H_2 and He	Cosmic-ray ionization rate – See Table A.2
	Heating rate per primary ionization in atomic region – Dalgarno & McCray (1972)
	Heating rate per primary ionization in molecular region – Glassgold et al. (2012)
Photoelectric effect on dust grains	Weingartner & Draine (2001b)
H_2 formation on dust grains	Hollenbach & McKee (1979)
UV pumping of H_2	Hollenbach & McKee (1979)
H_2 photodissociation	Black & Dalgarno (1977); Hollenbach & McKee (1979)
Cooling:	
C^+ fine structure line	Atomic data – Silva & Viegas (2002)
	Collisional rates with H – Barinovs et al. (2005)
	Collisional rates with H_2 – Wiesenfeld & Goldsmith (2014) ($T < 500$K), and Glover & Jappsen (2007) ($T > 500$K)
	Collisional rates with e – Keenan et al. (1986)
C fine structure line	Atomic data – Silva & Viegas (2002)
	Collisional rates with H – fit to Abrahamsson et al. (2007) by Draine (2011)

List of Heating and Cooling Processes (continued)

Process	Reference
	Collisional rates with H_2 – fit to Schroder et al. (1991) by Draine (2011)
	Collisional rates with e – Johnson et al. (1987)
O fine structure line	Atomic data – Silva & Viegas (2002)
	Collisional rates with H – fit to Abrahamsson et al. (2007) by Draine (2011)
	Collisional rates with H_2 – fit to Jaquet et al. (1992) by Draine (2011)
	Collisional rates with e – fit to Bell et al. (1998)
Lyα line	Atomic data – Draine (2011)
	Collisional rates with e – fit to Vrinceanu et al. (2014)
CO rotational lines	Omukai et al. (2010)
H_2 rotational and vibrational lines	Glover & Abel (2008); Hollenbach & McKee (1979)
Dust thermal emission	Krumholz (2014)
Recombination of e on PAHs	Weingartner & Draine (2001b)
Collisional dissociation of H_2	Grassi et al. (2014)
Collisional ionization of H	Grassi et al. (2014)

Appendix C

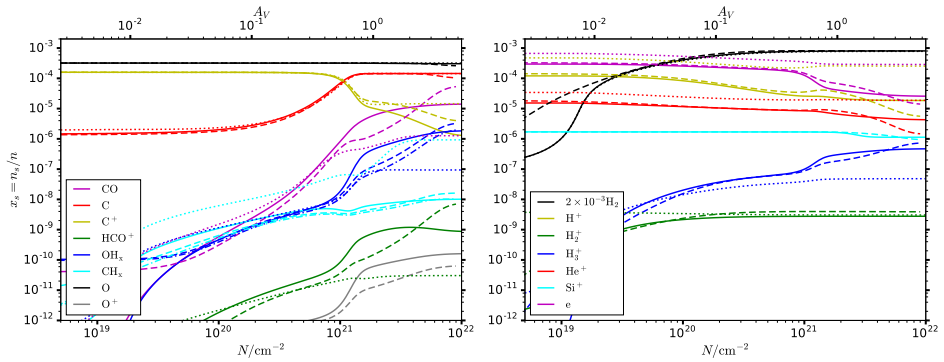
Additional Plots and Discussions for Code Test and Comparison

C.1 Chemistry with Constant Temperature

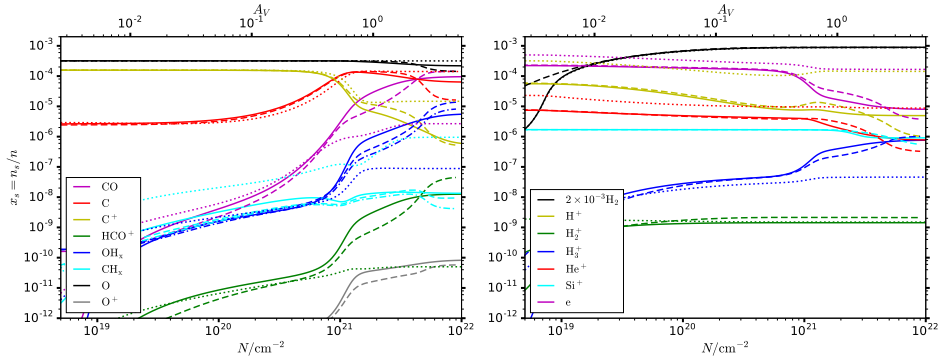
Here we show the comparison with the PDR code, our chemical network, and the NL99 network. The chemistry is evolved until it reaches equilibrium, and we fix the temperature at $T = 20$K. All independent species are shown between densities $n = 50$ cm^{-3} and $n = 1000$ cm^{-3}, supplementing Figures 2.2 and 2.4. Figures C.1 and C.3 plot the abundances, and Figures C.2 and C.4 plot the integrated column densities of different species.

C.2 Chemistry and Temperature

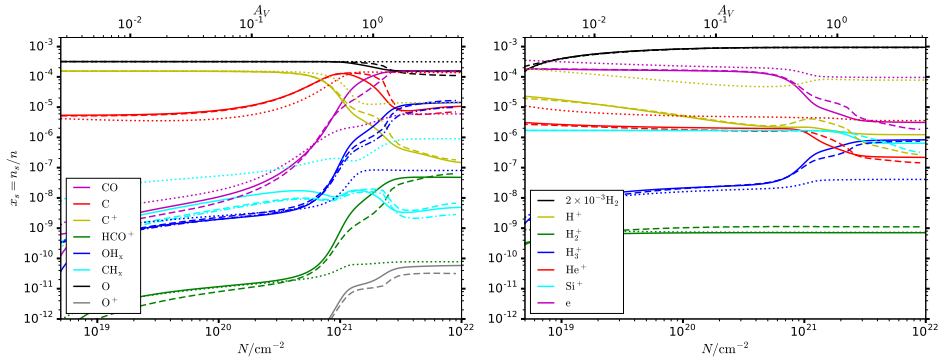
We carry out comparisons similar to Appendix C.1, but here we solve the chemistry and temperature simultaneously, until they both reach equilibrium. The results are shown in Figures C.5 and C.6. Again, our network agrees well with the PDR code, whereas the NL99 network shows significant disagreement. However, the equilibrium temperature in the NL99 network is very similar to that in our network. For example, at $n = 100$ cm^{-3} and $A_V > 1$, although there is much less CO in the NL99 network, C provides most cooling, resulting in similar



(a) $n = 50$ cm^{-3}

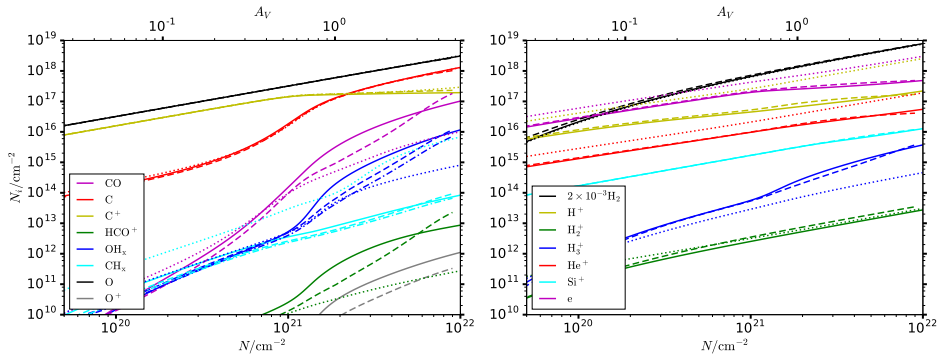


(b) $n = 100$ cm^{-3}

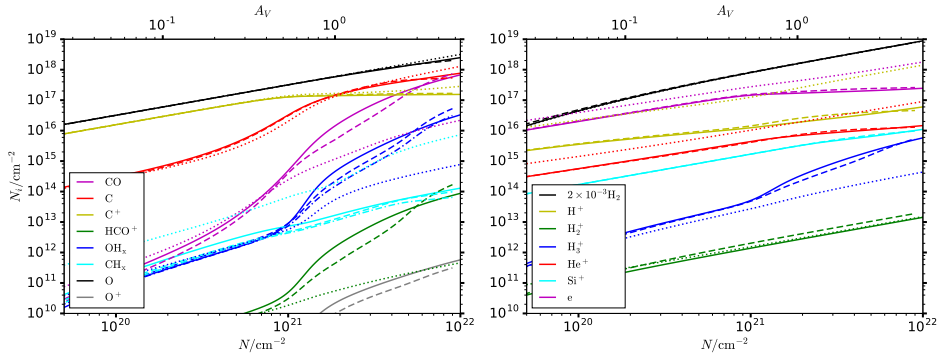


(c) $n = 200$ cm^{-3}

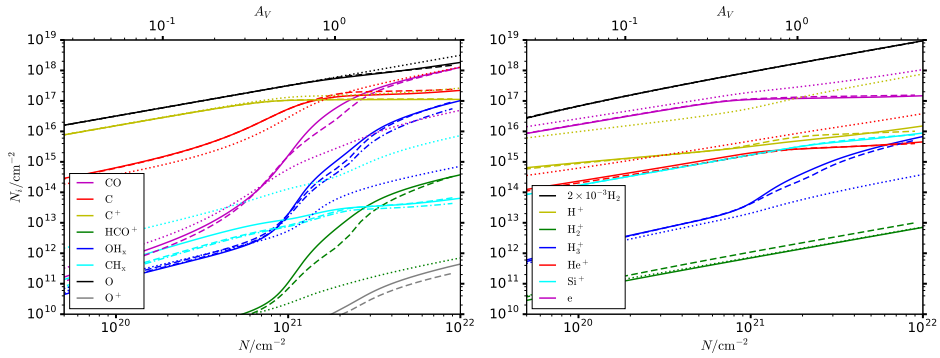
Figure C.1: Abundances of all independent species at densities $n = 50 - 200$ cm^{-3} in our network (solid), the PDR code (dashed), and the NL99 network (dotted), as a function of A_V/N. These figures are similar to Figure 2.2. Different species are represented by different colors as indicated in the legends. The abundance of H_2 is multiplied by a factor of 2×10^{-3}, i.e., if all hydrogen is in H_2, the black line will be at 10^{-3}. We have also plotted the abundances of CH and OH species from PDR code (cyan and blue dash-dotted lines), in addition to the sum of all CH_x and OH_x species. The cosmic-ray ionization rate $\xi_H = 2 \times 10^{-16}$ s^{-1}H^{-1}, and gas temperature is fixed at $T = 20$ K.



(a) $n = 50$ cm^{-3}

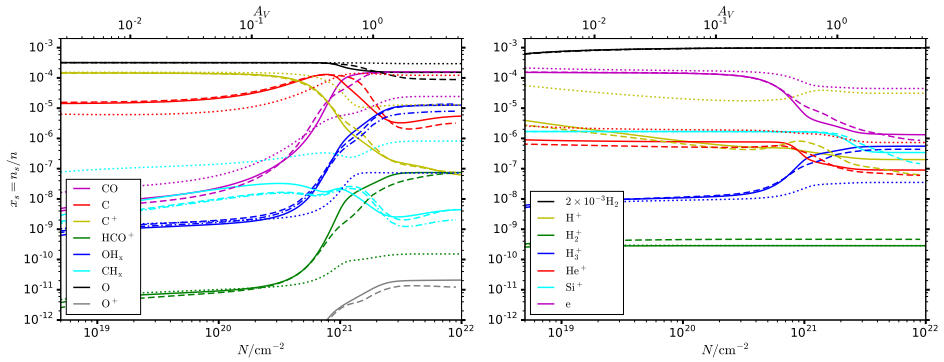


(b) $n = 100$ cm^{-3}

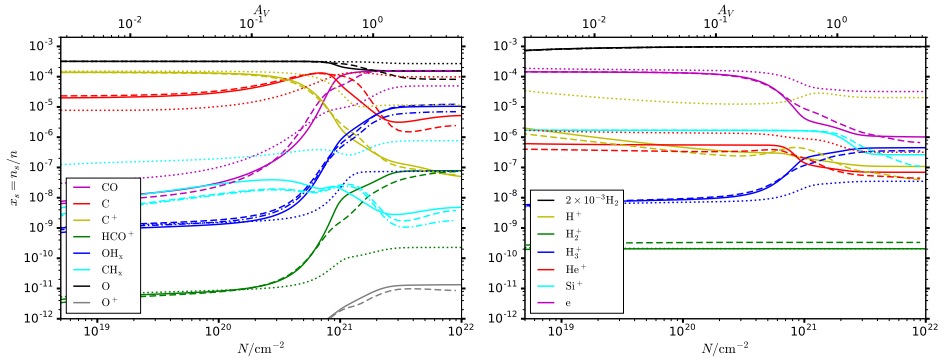


(c) $n = 200$ cm^{-3}

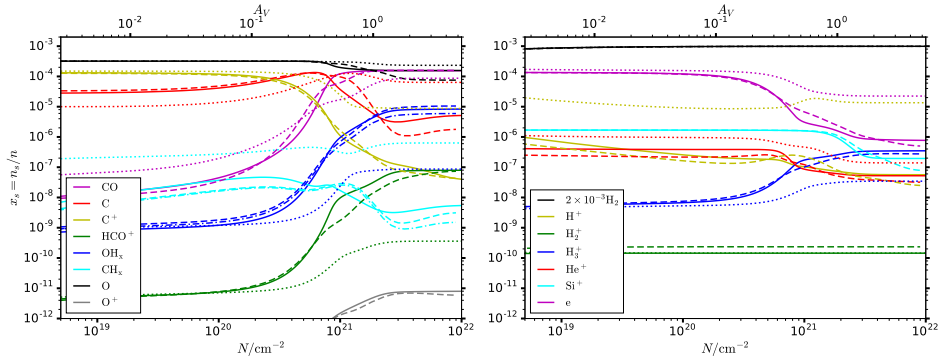
Figure C.2: Integrated column densities of all independent species at densities $n = 50 - 200$ cm^{-3} as a function of A_V/N, similar to Figure 2.4. Line colors and styles are the same as in Figure C.1.



(a) $n = 500$ cm^{-3}

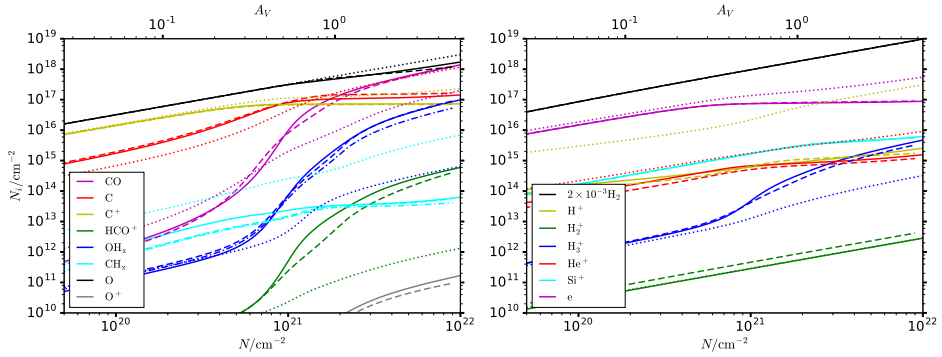


(b) $n = 700$ cm^{-3}

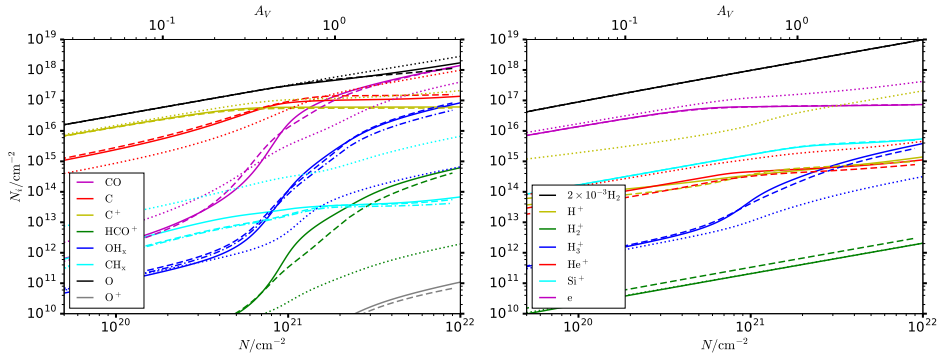


(c) $n = 1000$ cm^{-3}

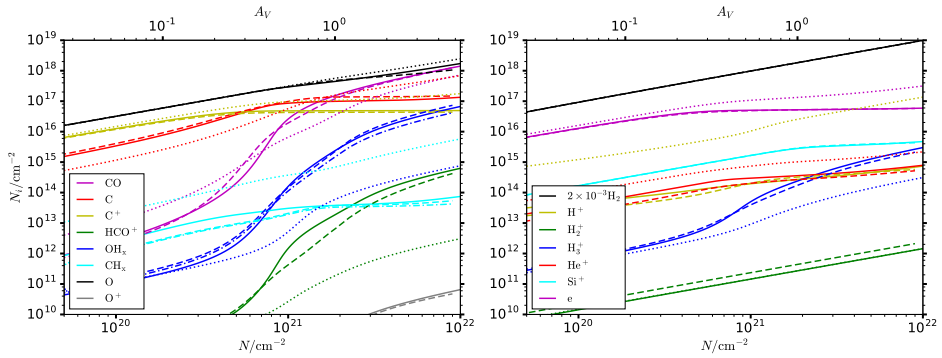
Figure C.3: Abundances of all independent species at densities $n = 500 - 1000$ cm^{-3}, similar to Figure C.1.



(a) $n = 500$ cm^{-3}



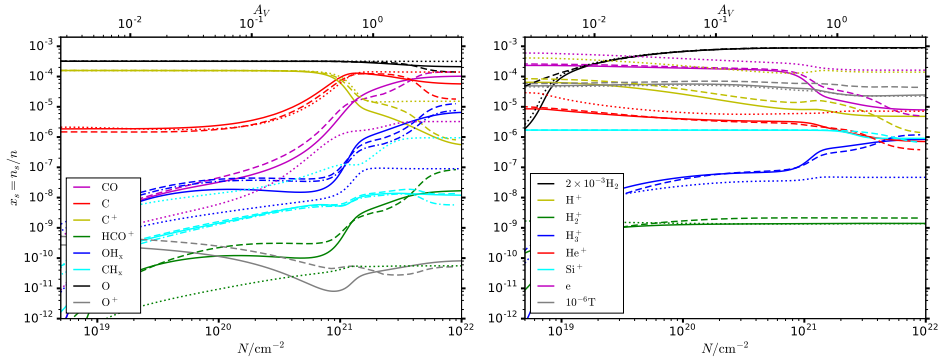
(b) $n = 700$ cm^{-3}



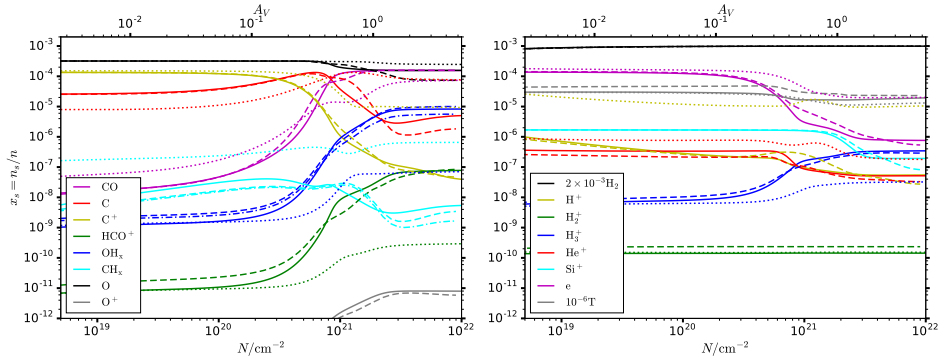
(c) $n = 1000$ cm^{-3}

Figure C.4: Integrated column densities of all independent species at densities $n = 500 - 1000$ cm^{-3}, similar to Figure C.2.

equilibrium temperatures. As noted by Glover & Clark (2012a), temperature is insensitive to detailed chemistry, although shielding is important because it sets the photoelectric heating rate.



(a) $n = 100$ cm^{-3}

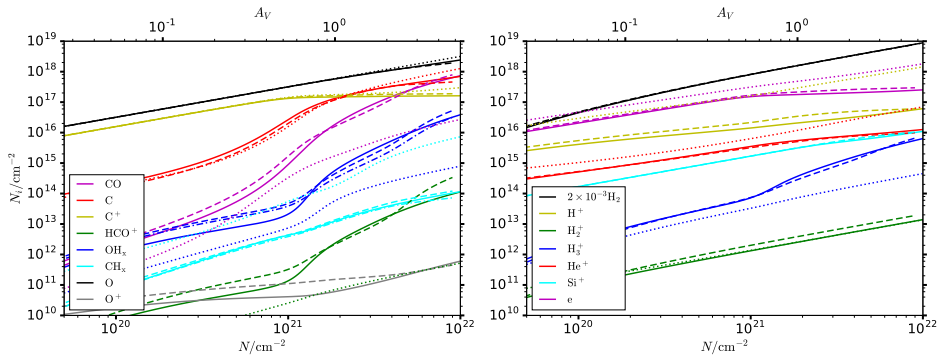


(b) $n = 1000$ cm^{-3}

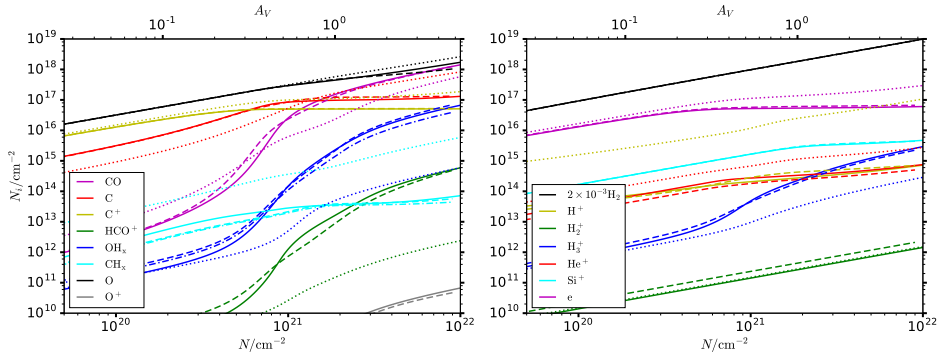
Figure C.5: Abundances of species, similar to Figure C.1 and C.3, but for temperature in thermal equilibrium.

C.3 Comparison at Low Metallicity

Figures C.7 and C.8 plot comparisons at $Z = 0.1$ between our network and the PDR code. Overall, there is a good agreement. Comparing to $Z = 1$ cases, CO forms at a much higher density $n \gtrsim 1000$ cm^{-3}. We note that at $n = 1000$ cm^{-3}, our network overproduces CO in



(a) $n = 100$ cm^{-3}



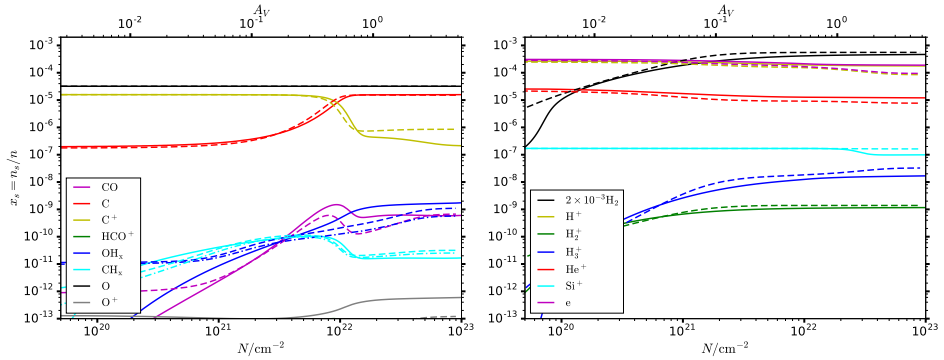
(b) $n = 1000$ cm^{-3}

Figure C.6: Integrated column densities of species in Figure C.5.

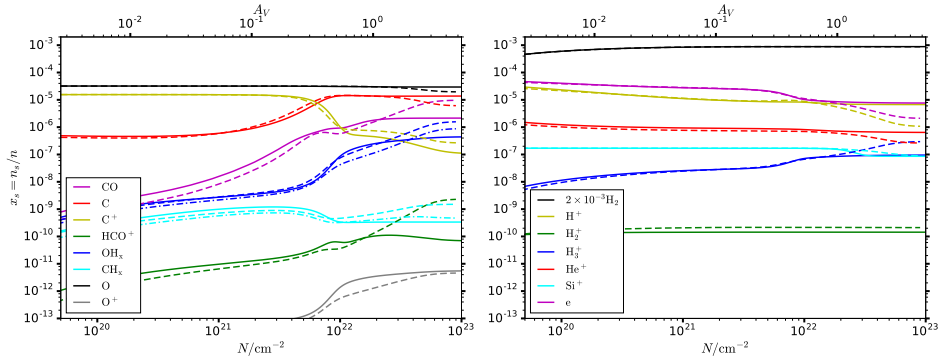
shielded regions. This is partly due to the difference in grain-assisted recombination rates, which is discussed in Appendix C.4.

C.4 Grain-assisted Recombination Rates

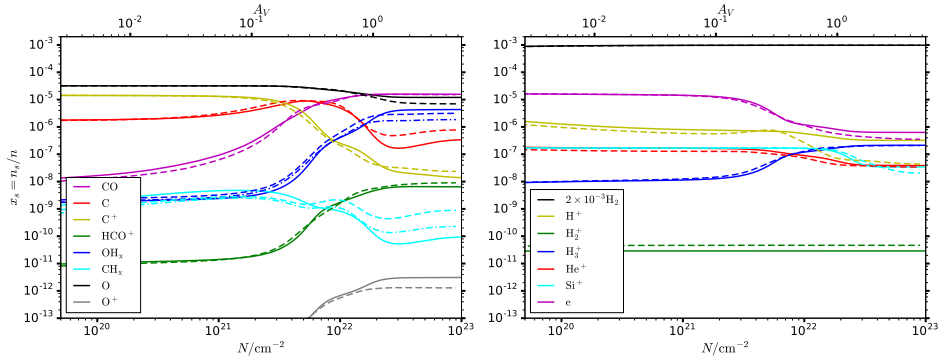
Ions such H^+, C^+, He^+, and Si^+ can recombine when they collide with PAHs. The recombination rate on dust grains is often higher than direct recombination with electrons, and therefore can have a major effect on chemistry. We use the results of Weingartner & Draine (2001a) for grain-assisted recombination rates in our network (see Table A.2). In Weingartner & Draine (2001a), they assume a certain size distribution of PAHs and calculate the charge distribution on PAHs. The final grain-assisted recombination rates are obtain by



(a) $n = 100$ cm^{-3}

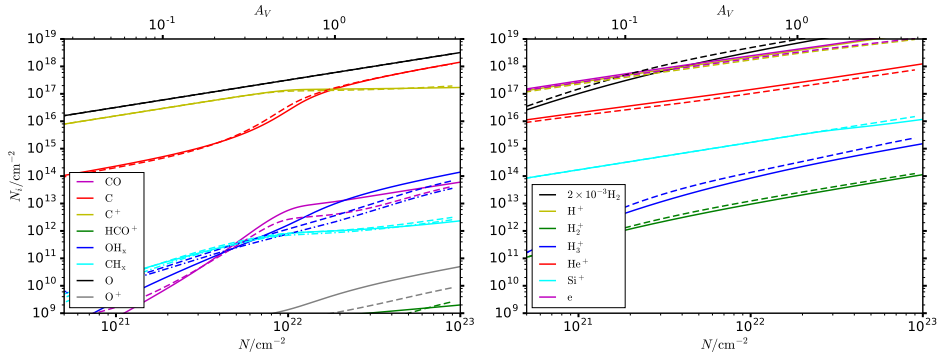


(b) $n = 1000$ cm^{-3}

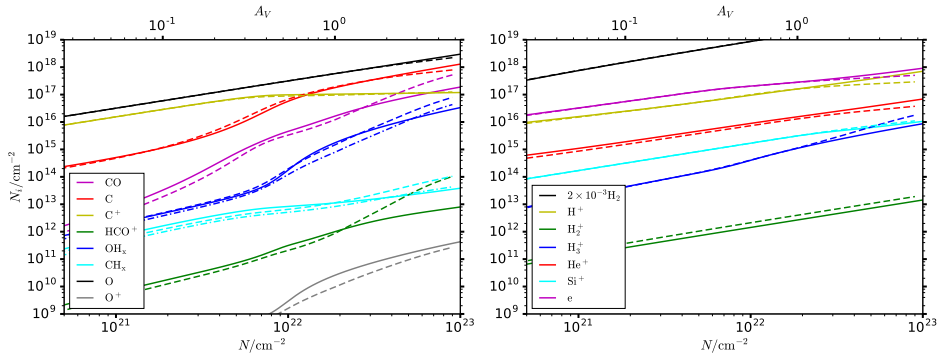


(c) $n = 5000$ cm^{-3}

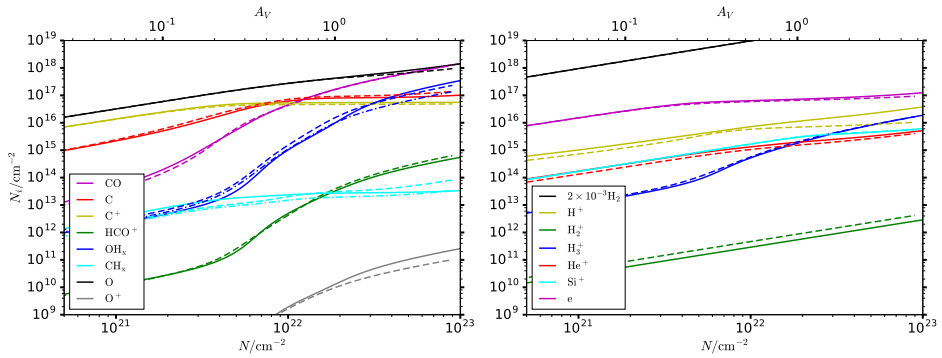
Figure C.7: Abundances of species, similar to Figures C.1 and C.3, but for $Z = 0.1$. Note that the NL99 network is not shown here.



(a) $n = 100$ cm^{-3}



(b) $n = 1000$ cm^{-3}



(c) $n = 5000$ cm^{-3}

Figure C.8: Integrated column densities of species in Figure C.7.

averaging over the PAH population. The PDR code uses a slightly different approach in Wolfire et al. (2008). The PAHs are assumed to have a single size, and three charge states, PAH^+, PAH^-, and PAH^0. By comparing with observations, Wolfire et al. (2008) calibrate their grain-assisted recombination rate of C^+ with the parameter $\phi_{\rm PAH} = 0.4$.

Figure C.9 shows the comparison of the grain-assisted recombination rate of C^+ between Wolfire et al. (2008) and Weingartner & Draine (2001a). The PAH populations in Wolfire et al. (2008) are assumed to be in charge equilibrium states with reactions described in Appendix C2 of Wolfire et al. (2003), and the total PAH abundance is $n_{\rm PAH}/n = 2 \times 10^{-7}$. The reaction rate depends mainly on the parameter $\psi = 1.7\chi\sqrt{T}/n_e$, and only has a very weak dependence on temperature. As can be seen in Figure C.9, the Wolfire et al. (2008) and Weingartner & Draine (2001a) rates can differ by a factor of ~ 2. In the main part of this work, we use 0.6 times the Weingartner & Draine (2001a) rates to match with Wolfire et al. (2008) at $\psi \sim 10^4$. Figure C.10 and C.11 show comparisons with the original Weingartner & Draine (2001a) rates. At $n = 100$ cm^{-3}, The abundances of CO, OH_x, HCO^+, and He^+ can change by a factor of ~ 5 around $A_V \sim 1$, but the chemical abundances at higher density $n = 1000$ cm^{-3} are largely unaffected.

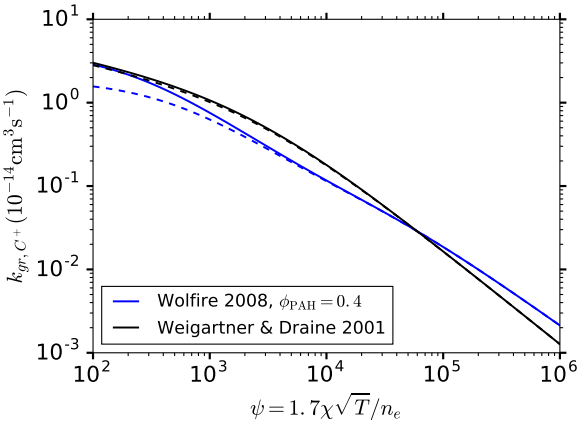
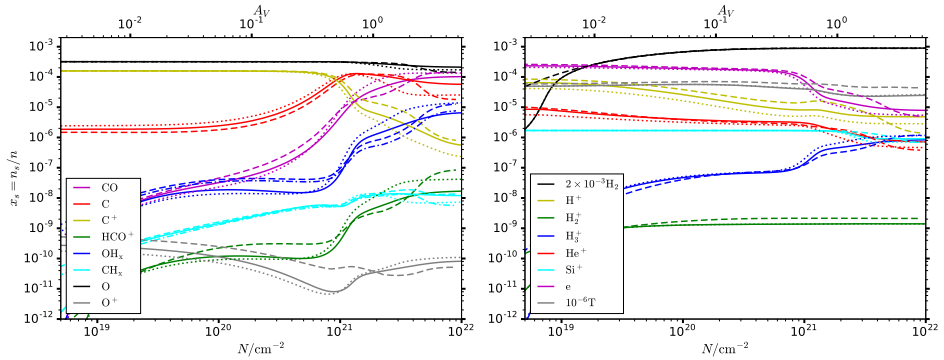
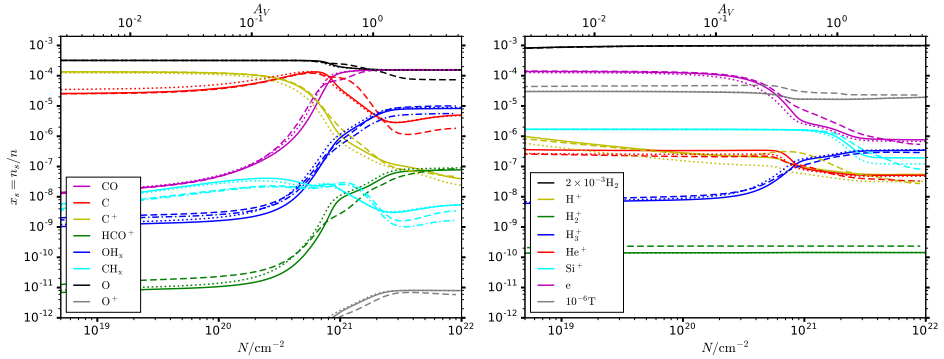


Figure C.9: Comparison of the grain-assisted recombination rate of C^+ between Wolfire et al. (2008) (blue) and Weingartner & Draine (2001a) (black). The solid and dashed lines are results with $T = 20$ K and $T = 100$ K. The temperature T is in Kelvin, and the electron density $n_{\rm e}$ is in cm^{-3} in ψ.



(a) $n = 100$ cm^{-3}

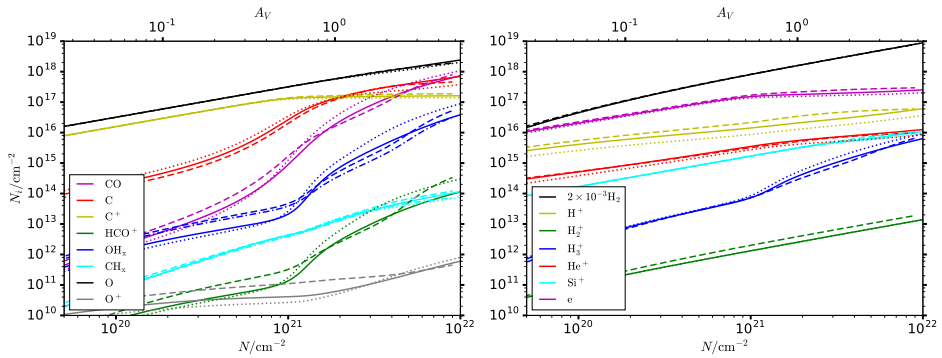


(b) $n = 1000$ cm^{-3}

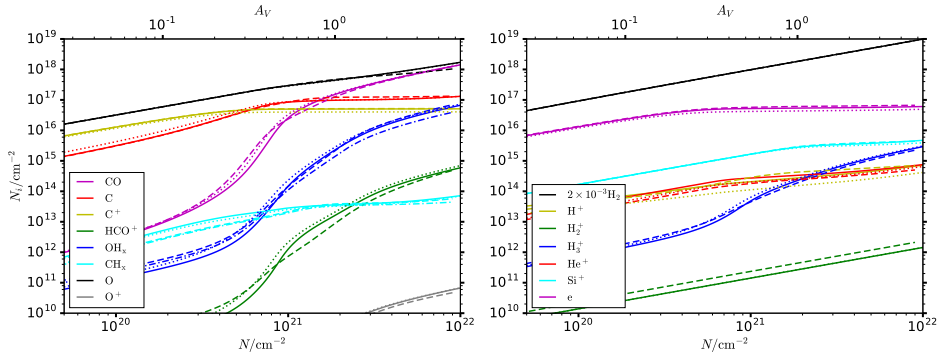
Figure C.10: Comparison of chemical abundances in our network with 0.6 times the grain-assisted recombination rates in Weingartner & Draine (2001a) (solid), the original Weingartner & Draine (2001a) rates (dotted), and the PDR code (dashed). The temperature is in thermal equilibrium.

C.5 Grain Surface Reactions

In addition to the grain-assisted recombinations, dust grains can also affect the gas-phase chemistry by grain surface reactions (Hollenbach et al., 2009). This includes the formation of OH and H_2O on the surface of dust grains, and the freeze-out of molecules such as CO and H_2O on dust grains in cold and shielded regions. Figures C.12 and C.13 show the comparisons of the chemical abundances with and without the grain surface reactions. The formation of OH and H_2O on grains results in a higher OH_x and CO abundances at $n = 1000$ cm^{-3}



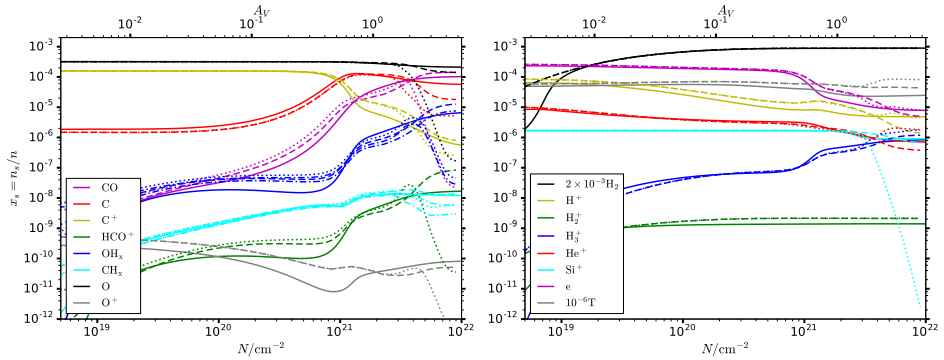
(a) $n = 100$ cm^{-3}



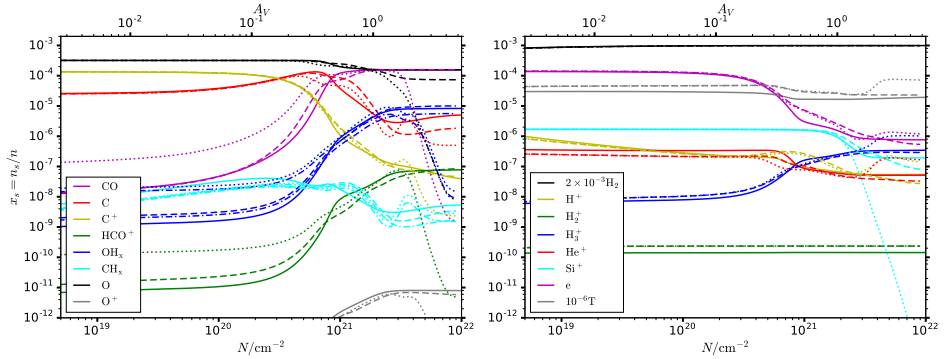
(b) $n = 1000$ cm^{-3}

Figure C.11: Integrated column densities of species in Figure C.10.

and $A_V < 1$. The freeze-out can greatly reduce the abundances of CO and other species at $A_V \gtrsim 2$. Since the CO abundance is still low in regions that are affected by the formation of OH and H_2O on grains, and the freeze-out depends on the grain size distribution, which is very uncertain in dense and shielded clouds, we do not include grain surface reaction in our network. Ideally, the effect of freeze-out on carbon bearing species should be calibrated with observations of diffuse and dense clouds as was done with oxygen-bearing species in Hollenbach et al. (2009, 2012) and Sonnentrucker et al. (2015).



(a) $n = 100$ cm^{-3}

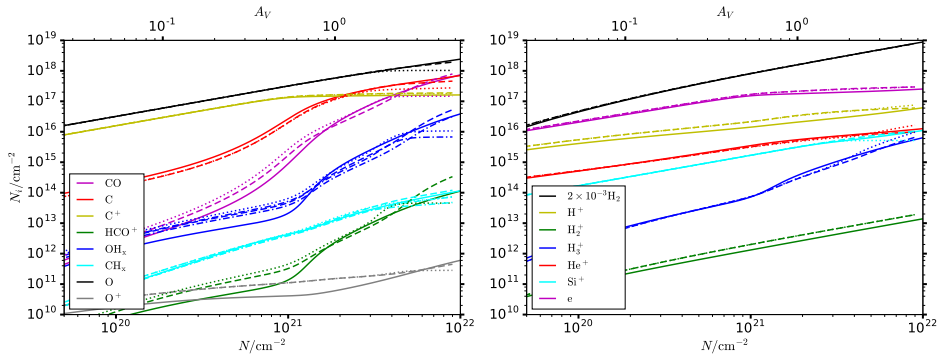


(b) $n = 1000$ cm^{-3}

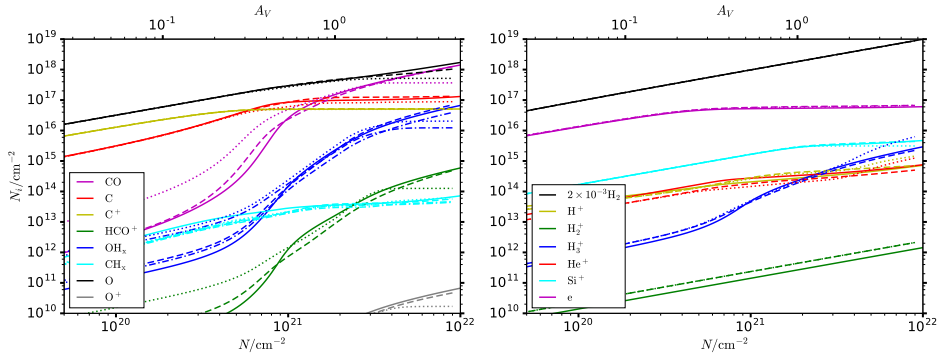
Figure C.12: Comparison of chemical abundances in our network (solid), the PDR code (dashed), and the PDR code with grain surface reactions in Hollenbach et al. (2009) (dotted). The temperature is in thermal equilibrium.

C.6 Comparison with the *PyPDR* code

Figure C.14 shows a comparison between our chemical network and the *PyPDR* code. We disabled the grain-assisted recombination of ions in our network to make a direct comparison with *PyPDR*, which does not have these reactions. We also updated the reaction rates in the *PyPDR* code, to be consistent with the reaction rates in this work (Tables A.1 and A.2). Note that *PyPDR* does not include metals such as Si, which is in our network. Figure C.14 shows that our chemical network (without grain-assisted recombination) agrees very well with the results from the *PyPDR* code.

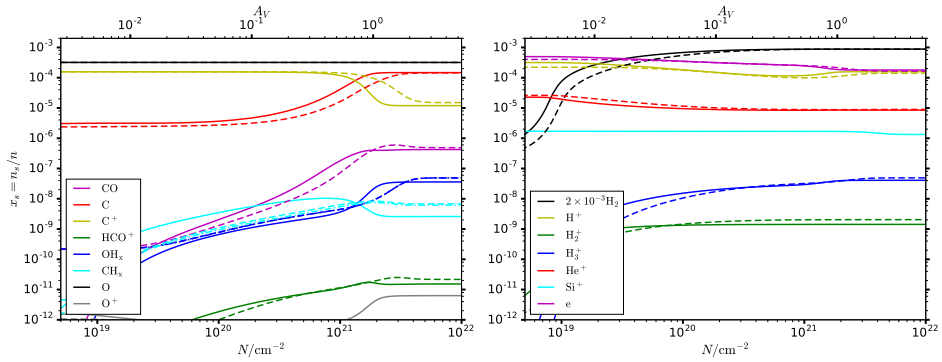


(a) $n = 100$ cm^{-3}

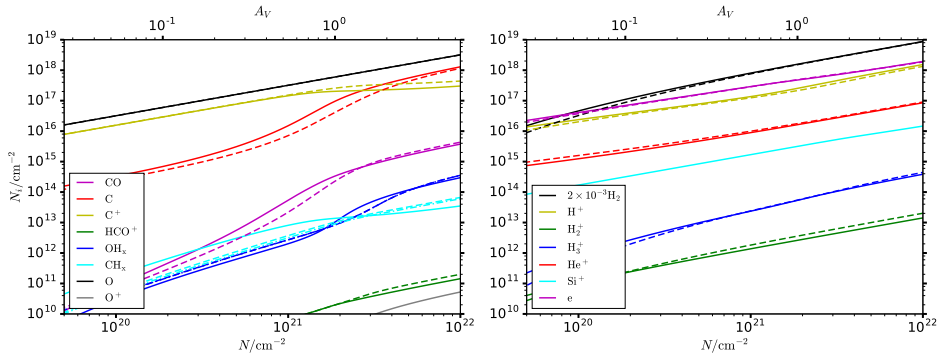


(b) $n = 1000$ cm^{-3}

Figure C.13: Integrated column densities of species in Figure C.12.



(a) Abundances



(b) Column densities

Figure C.14: Abundances and column densities of species at density $n = 100$ cm^{-3} in our network (solid), and the *PyPDR* code (dashed), as a function of A_V/N. This is similar to Figures C.1 and C.2, but with the dashed lines showing the *PyPDR* code instead of the Wolfire PDR code. We have also plotted the abundances of CH and OH species from the *PyPDR* code (cyan and blue dash-dotted lines), in addition to the sum of all CH_x and OH_x species. The cosmic-ray ionization rate $\xi_H = 2 \times 10^{-16}$ s^{-1}H^{-1}, and gas temperature is fixed at $T = 20$ K. The reactions of grain-assisted recombination of ions are excluded in our network to be consistent with *PyPDR*.

Appendix D

Characteristic Density in Slab and Spherical Turbulent Clouds

Define $s \equiv \ln(\rho/\rho_0)$, where $\rho_0 = M/V = \langle\rho\rangle_V$ is the volume-weighted density. Both the volume- and the mass-weighted density obey the log-normal distribution

$$f_{V,M}(s)\mathrm{d}s = \frac{1}{\sigma_s\sqrt{2\pi}} \exp\left[-\frac{(s-\mu_{V,M})^2}{2\sigma_s^2}\right] \mathrm{d}s, \tag{D.1}$$

where $\mu_V = -\sigma_s^2/2$ and $\mu_M = \sigma_s^2/2$ are the volume- and mass- weighted means of the parameter s. Both observations of molecular clouds and numerical simulations show that the variance σ_s is related to the turbulence Mach number $\mathcal{M}$ (e.g., Padoan et al., 1997; Lemaster & Stone, 2008; Brunt, 2010; Kainulainen & Tan, 2013)

$$\sigma_s \approx \ln(1 + b^2\mathcal{M}^2), \tag{D.2}$$

with $b \approx 1/2 - 1/3$. Thus, the mass-weighted mean density is

$$\left\langle \frac{\rho}{\rho_0} \right\rangle_M = \int \frac{\rho}{\rho_0} f_M(s)\mathrm{d}s = \int e^s f(s)\mathrm{d}s = e^{\sigma_s^2} \approx 1 + b^2\mathcal{M}^2. \tag{D.3}$$

For slab clouds, the balance of the gas self-gravity with the mid-plane pressure P (assumed to be primarily from turbulence) gives

$$P = \frac{\pi G \Sigma^2}{2}, \tag{D.4}$$

where Σ is the gas surface density. The average volume-weighted density is then $\rho_0 \equiv P/\sigma_{\rm 1D}^2 = \pi G \Sigma^2/(2\sigma_{\rm 1D}^2)$, where $\sigma_{\rm 1D}$ is the one-dimensional velocity dispersion of the cloud-scale turbulence. The Mach number squared

$$\mathcal{M}^2 = \frac{\sigma_{\rm 3D}^2}{c_s^2} = \frac{3\pi G \Sigma^2}{2\rho_0 c_s^2}, \tag{D.5}$$

where c_s is the sound speed. Therefore, according to Equation (D.3), the mass-weighted mean density of the slab cloud can be written as

$$\langle \rho \rangle_{M,\rm slab} = \rho_0 + b^2 \mathcal{M}^2 \rho_0 = \rho_0 + 3b^2 \left(\frac{\pi G \Sigma^2}{2c_s^2} \right). \tag{D.6}$$

For uniform spherical clouds, the virial parameter

$$\alpha_{\rm vir} \equiv \frac{2E_k}{|E_G|} = \frac{5\sigma_{\rm 1D}^2 R}{GM}, \tag{D.7}$$

where E_k is the kinetic energy of the cloud from turbulence and E_G is the gravitational energy. A virialized cloud has $\alpha_{\rm vir} = 1$, and marginally gravitationally bound cloud has $\alpha_{\rm vir} = 2$. The Mach number squared can be written as

$$\mathcal{M}^2 = \frac{\sigma_{\rm 3D}^2}{c_s^2} = \frac{3\sigma_{\rm 1D}^2}{c_s^2} = \frac{3\alpha_{\rm vir} GM}{5Rc_s^2} = \frac{1}{\rho_0} \alpha_{\rm vir} \frac{9}{10} \left(\frac{\pi G \Sigma^2}{2c_s^2} \right). \tag{D.8}$$

Here we define the average cloud density $\rho_0 \equiv M/(\frac{4\pi}{3} R^3)$, and the average cloud surface density $\Sigma \equiv M/(\pi R^2)$. Similar to Equation (D.6), the mass-weighted mean density of the

spherical cloud is given by

$$\langle \rho \rangle_{M,\mathrm{sphere}} = \rho_0 + b^2 \mathcal{M}^2 \rho_0 = \rho_0 + \left(\frac{9}{10} \alpha_{\mathrm{vir}} \right) b^2 \left(\frac{\pi G \Sigma^2}{2 c_s^2} \right). \tag{D.9}$$

Equations (D.6) and (D.9) can be written together as

$$\langle \rho \rangle_M = \rho_0 + a b^2 \left(\frac{\pi G \Sigma^2}{2 c_s^2} \right), \tag{D.10}$$

where $a = 3$ for slab clouds and $a = 9\alpha_{\mathrm{vir}}/10$ for spherical clouds. Using the relations $\rho = 1.4 m_{\mathrm{H}} n$ and $\Sigma = 1.4 m_{\mathrm{H}} N$, where $m_{\mathrm{H}} = 1.67 \times 10^{-24}$ g is the mass of a hydrogen atom, and the factor 1.4 comes from helium, Equation (D.10) gives

$$\langle n \rangle_M = \langle n \rangle_V + 1.4 m_{\mathrm{H}} a b^2 \left(\frac{\pi G N^2}{2 c_s^2} \right). \tag{D.11}$$

Appendix E

Additional Plots for Comparison with Observations of Diffuse and Translucent Clouds

Figure E.1 shows a detailed comparison between observations and our slab model with no grain-assisted recombination, and depletion of carbon abundance.

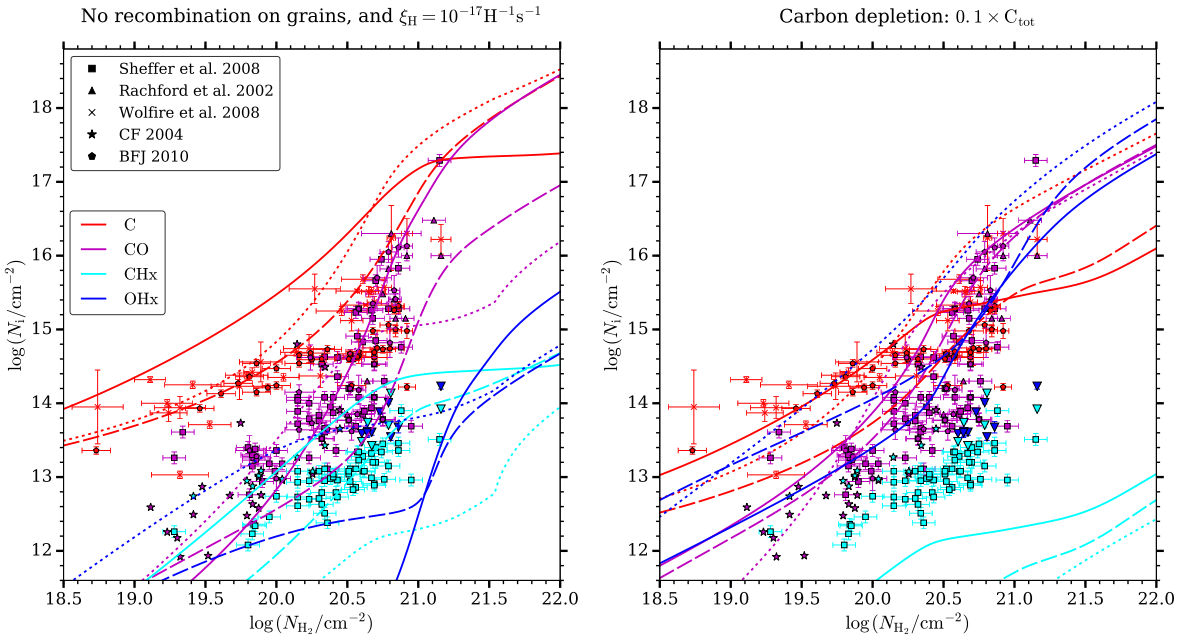


Figure E.1: Similar to the right panel of Figure 2.10, but with no grain-assisted recombination of ions (*left*), or depletion of gas-phase carbon abundance by a factor of 10 (*right*).

Bibliography

Abrahamsson, E., Krems, R. V., & Dalgarno, A. 2007, ApJ, 654, 1171

Acharyya, K., Fuchs, G. W., Fraser, H. J., van Dishoeck, E. F., & Linnartz, H. 2007, A&A, 466, 1005

Ackermann, M., Ajello, M., Atwood, W. B., et al. 2012, ApJ, 750, 3

Anicich, V. G., & Huntress, Jr., W. T. 1986, ApJS, 62, 553

Ao, Y., Henkel, C., Menten, K. M., et al. 2013, A&A, 550, A135

Badnell, N. R. 2006, ApJS, 167, 334

Badnell, N. R., O'Mullane, M. G., Summers, H. P., et al. 2003, A&A, 406, 1151

Bally, J., & Hi-GAL Team. 2014, in IAU Symposium, Vol. 303, The Galactic Center: Feeding and Feedback in a Normal Galactic Nucleus, ed. L. O. Sjouwerman, C. C. Lang, & J. Ott, 1–14

Barinovs, Ğ., van Hemert, M. C., Krems, R., & Dalgarno, A. 2005, ApJ, 620, 537

Barlow, S. E. 1984, PhD thesis, UNIVERSITY OF COLORADO AT BOULDER.

Bell, K. L., Berrington, K. A., & Thomas, M. R. J. 1998, MNRAS, 293, L83

Bensch, F., Leuenhagen, U., Stutzki, J., & Schieder, R. 2003, ApJ, 591, 1013

Bergin, E. A., Langer, W. D., & Goldsmith, P. F. 1995, ApJ, 441, 222

Bialy, S., Bihr, S., Beuther, H., Henning, T., & Sternberg, A. 2017, ApJ, 835, 126

Bialy, S., & Sternberg, A. 2016, ApJ, 822, 83

Bialy, S., Sternberg, A., Lee, M.-Y., Le Petit, F., & Roueff, E. 2015, ApJ, 809, 122

Bigiel, F., Leroy, A., Walter, F., et al. 2008, AJ, 136, 2846

Bigiel, F., Leroy, A. K., Walter, F., et al. 2011, ApJ, 730, L13

Bisbas, T. G., Papadopoulos, P. P., & Viti, S. 2015, ApJ, 803, 37

Black, J. H., & Dalgarno, A. 1977, ApJS, 34, 405

Blitz, L., Bloemen, J. B. G. M., Hermsen, W., & Bania, T. M. 1985, A&A, 143, 267

Bohlin, R. C., Savage, B. D., & Drake, J. F. 1978, ApJ, 224, 132

Bolatto, A. D., Leroy, A. K., Rosolowsky, E., Walter, F., & Blitz, L. 2008, ApJ, 686, 948

Bolatto, A. D., Wolfire, M., & Leroy, A. K. 2013a, ARA&A, 51, 207

—. 2013b, ARA&A, 51, 207

Bonnor, W. B. 1956, MNRAS, 116, 351

Brunt, C. M. 2010, A&A, 513, A67

Bryans, P., Kreckel, H., Roueff, E., Wakelam, V., & Savin, D. W. 2009, ApJ, 694, 286

Burgh, E. B., France, K., & Jenkins, E. B. 2010, ApJ, 708, 334

Burgh, E. B., France, K., & McCandliss, S. R. 2007, ApJ, 658, 446

Burton, M. G., Ashley, M. C. B., Braiding, C., et al. 2015, ApJ, 811, 13

Cardelli, J. A., Sofia, U. J., Savage, B. D., Keenan, F. P., & Dufton, P. L. 1994, ApJ, 420, L29

Carty, D., Goddard, A., Köhler, S. P. K., Sims, I. R., & Smith, I. W. M. 2006, The Journal of Physical Chemistry A, 110, 3101, pMID: 16509632

Clark, P. C., & Glover, S. C. O. 2015, MNRAS, 452, 2057

Cohen, S. D., Hindmarsh, A. C., & Dubois, P. F. 1996, Computers in Physics, 10, 138

Crenny, T., & Federman, S. R. 2004, ApJ, 605, 278

Dalgarno, A., & McCray, R. A. 1972, ARA&A, 10, 375

Dalgarno, A., Yan, M., & Liu, W. 1999, ApJS, 125, 237

Dame, T. M., Hartmann, D., & Thaddeus, P. 2001, ApJ, 547, 792

de Ruette, N., Miller, K. A., O'Connor, A. P., et al. 2016, ApJ, 816, 31

Dobbs, C. L., Krumholz, M. R., Ballesteros-Paredes, J., et al. 2014, Protostars and Planets VI, 3

Downes, D., & Solomon, P. M. 1998, ApJ, 507, 615

Draine, B. T. 1978, ApJS, 36, 595

—. 2003, ApJ, 598, 1017

—. 2011, Physics of the Interstellar and Intergalactic Medium

Draine, B. T., & Bertoldi, F. 1996, ApJ, 468, 269

Duarte-Cabral, A., Acreman, D. M., Dobbs, C. L., et al. 2015, MNRAS, 447, 2144

Dullemond, C. P., Juhasz, A., Pohl, A., et al. 2012, RADMC-3D: A multi-purpose radiative transfer tool, Astrophysics Source Code Library, ascl:1202.015

Ebert, R. 1955, ZAp, 37, 217

Elmegreen, B. G. 1993, ApJ, 411, 170

Feldmann, R., Gnedin, N. Y., & Kravtsov, A. V. 2012, ApJ, 758, 127

Ferland, G. J., Peterson, B. M., Horne, K., Welsh, W. F., & Nahar, S. N. 1992, ApJ, 387, 95

Flower, D. R. 2001, Journal of Physics B: Atomic, Molecular and Optical Physics, 34, 2731

Flower, D. R., & Launay, J. M. 1985, MNRAS, 214, 271

Genzel, R., Tacconi, L. J., Gracia-Carpio, J., et al. 2010, MNRAS, 407, 2091

Geppert, W. D., Thomas, R. D., Ehlerding, A., et al. 2005, Journal of Physics Conference Series, 4, 26

Girichidis, P., Walch, S., Naab, T., et al. 2016, MNRAS, 456, 3432

Glassgold, A. E., Galli, D., & Padovani, M. 2012, ApJ, 756, 157

Glassgold, A. E., & Langer, W. D. 1974, ApJ, 193, 73

Glover, S. C. O., & Abel, T. 2008, MNRAS, 388, 1627

Glover, S. C. O., & Clark, P. C. 2012a, MNRAS, 421, 116

—. 2012b, MNRAS, 421, 9

—. 2012c, MNRAS, 426, 377

—. 2016, MNRAS, 456, 3596

Glover, S. C. O., Federrath, C., Mac Low, M.-M., & Klessen, R. S. 2010, MNRAS, 404, 2

Glover, S. C. O., & Jappsen, A.-K. 2007, ApJ, 666, 1

Glover, S. C. O., & Mac Low, M.-M. 2007, ApJS, 169, 239

—. 2011, MNRAS, 412, 337

Godard, B., Falgarone, E., & Pineau des Forêts, G. 2014, A&A, 570, A27

Goldsmith, P. F. 2001, ApJ, 557, 736

—. 2013, ApJ, 774, 134

Goldsmith, P. F., & Langer, W. D. 1978, ApJ, 222, 881

Gong, M., Ostriker, E. C., & Wolfire, M. G. 2017, ApJ, 843, 38

Grassi, T., Bovino, S., Schleicher, D. R. G., et al. 2014, MNRAS, 439, 2386

Gredel, R., Lepp, S., & Dalgarno, A. 1987, ApJ, 323, L137

Gredel, R., Lepp, S., Dalgarno, A., & Herbst, E. 1989, ApJ, 347, 289

Güsten, R., & Philipp, S. D. 2004, in The Dense Interstellar Medium in Galaxies, ed. S. Pfalzner, C. Kramer, C. Staubmeier, & A. Heithausen, Vol. 91, 253

Habing, H. J. 1968, Bull. Astron. Inst. Netherlands, 19, 421

Heays, A. N., Bosman, A. D., & van Dishoeck, E. F. 2017, ArXiv e-prints, arXiv:1701.04459

Heiles, C., & Troland, T. H. 2003, ApJ, 586, 1067

Heyer, M., & Dame, T. M. 2015, ARA&A, 53, 583

Heyer, M. H., & Brunt, C. M. 2004, ApJ, 615, L45

Hollenbach, D., Kaufman, M. J., Bergin, E. A., & Melnick, G. J. 2009, ApJ, 690, 1497

Hollenbach, D., Kaufman, M. J., Neufeld, D., Wolfire, M., & Goicoechea, J. R. 2012, ApJ, 754, 105

Hollenbach, D., & McKee, C. F. 1979, ApJS, 41, 555

Hummer, D. G., & Storey, P. J. 1998, MNRAS, 297, 1073

Hunt, L. K., García-Burillo, S., Casasola, V., et al. 2015, A&A, 583, A114

Imara, N. 2015, ApJ, 803, 38

Indriolo, N., Geballe, T. R., Oka, T., & McCall, B. J. 2007, ApJ, 671, 1736

Indriolo, N., Neufeld, D. A., Gerin, M., et al. 2015, ApJ, 800, 40

Israel, F. P. 1997, A&A, 328, 471

Jameson, K. E., Bolatto, A. D., Leroy, A. K., et al. 2016, ApJ, 825, 12

Janev, R. K., Langer, W. D., & Evans, K. 1987, Elementary processes in Hydrogen-Helium plasmas - Cross sections and reaction rate coefficients

Jaquet, R., Staemmler, V., Smith, M. D., & Flower, D. R. 1992, Journal of Physics B Atomic Molecular Physics, 25, 285

Jenkins, E. B. 2009, ApJ, 700, 1299

Jenkins, E. B., & Tripp, T. M. 2011, ApJ, 734, 65

Johnson, C. T., Burke, P. G., & Kingston, A. E. 1987, Journal of Physics B Atomic Molecular Physics, 20, 2553

Kainulainen, J., & Tan, J. C. 2013, A&A, 549, A53

Kaufman, M. J., Wolfire, M. G., & Hollenbach, D. J. 2006, ApJ, 644, 283

Kaufman, M. J., Wolfire, M. G., Hollenbach, D. J., & Luhman, M. L. 1999, ApJ, 527, 795

Keenan, F. P., Lennon, D. J., Johnson, C. T., & Kingston, A. E. 1986, MNRAS, 220, 571

Kennicutt, R. C., & Evans, N. J. 2012, ARA&A, 50, 531

Keto, E., & Caselli, P. 2008, ApJ, 683, 238

Kim, C.-G., Kim, W.-T., & Ostriker, E. C. 2011, ApJ, 743, 25

Kim, C.-G., & Ostriker, E. C. 2016, ArXiv e-prints, arXiv:1612.03918

Kim, C.-G., Ostriker, E. C., & Kim, W.-T. 2013, ApJ, 776, 1

Kim, J. K., Theard, L. P., & Huntress, Jr., W. T. 1975, Chemical Physics Letters, 32, 610

Kong, S., Lada, C. J., Lada, E. A., et al. 2015, ApJ, 805, 58

Koyama, H., & Inutsuka, S.-i. 2002, ApJ, 564, L97

Krumholz, M. R. 2014, MNRAS, 437, 1662

Krumholz, M. R., Leroy, A. K., & McKee, C. F. 2011, ApJ, 731, 25

Krumholz, M. R., McKee, C. F., & Tumlinson, J. 2009, ApJ, 693, 216

Lada, C. J., Lombardi, M., & Alves, J. F. 2009, ApJ, 703, 52

Larson, R. B. 1981, MNRAS, 194, 809

Le Petit, F., Nehmé, C., Le Bourlot, J., & Roueff, E. 2006, ApJS, 164, 506

Le Teuff, Y. H., Millar, T. J., & Markwick, A. J. 2000, A&AS, 146, 157

Lee, E. J., Chang, P., & Murray, N. 2014a, ArXiv e-prints, arXiv:1406.4148

Lee, M.-Y., Stanimirović, S., Wolfire, M. G., et al. 2014b, ApJ, 784, 80

—. 2014c, ApJ, 784, 80

Leitherer, C., Schaerer, D., Goldader, J. D., et al. 1999, ApJS, 123, 3

Lemaster, M. N., & Stone, J. M. 2008, ApJ, 682, L97

Lepp, S., & Shull, J. M. 1983, ApJ, 270, 578

Leroy, A., Cannon, J., Walter, F., Bolatto, A., & Weiss, A. 2007, ApJ, 663, 990

Leroy, A. K., Walter, F., Brinks, E., et al. 2008, AJ, 136, 2782

Leroy, A. K., Bolatto, A., Gordon, K., et al. 2011, ApJ, 737, 12

Leroy, A. K., Hughes, A., Schruba, A., et al. 2016, ApJ, 831, 16

Leung, C. M., Herbst, E., & Huebner, W. F. 1984, ApJS, 56, 231

Linder, F., Janev, R. K., & Botero, J. 1995, in Atomic and Molecular Processes in Fusion Edge Plasmas, ed. R. K. Janev, 397

Liszt, H. S. 2011, A&A, 527, A45

Lombardi, M., Alves, J., & Lada, C. J. 2006, A&A, 454, 781

Mac Low, M.-M., & Klessen, R. S. 2004, Reviews of Modern Physics, 76, 125

Mac Low, M.-M., & Shull, J. M. 1986, ApJ, 302, 585

Magnani, L., Blitz, L., & Mundy, L. 1985, ApJ, 295, 402

Martin, P. G., Keogh, W. J., & Mandy, M. E. 1998, ApJ, 499, 793

Martin, P. G., Schwarz, D. H., & Mandy, M. E. 1996, ApJ, 461, 265

McCall, B. J., Huneycutt, A. J., Saykally, R. J., et al. 2004, Phys. Rev. A, 70, 052716

McElroy, D., Walsh, C., Markwick, A. J., et al. 2013, A&A, 550, A36

Meijerink, R., & Spaans, M. 2005, A&A, 436, 397

Narayanan, D., Krumholz, M., Ostriker, E. C., & Hernquist, L. 2011, MNRAS, 418, 664

Narayanan, D., Krumholz, M. R., Ostriker, E. C., & Hernquist, L. 2012, MNRAS, 421, 3127

Nelson, R. P., & Langer, W. D. 1997, ApJ, 482, 796

—. 1999, ApJ, 524, 923

Neufeld, D. A., & Kaufman, M. J. 1993, ApJ, 418, 263

Neufeld, D. A., Lepp, S., & Melnick, G. J. 1995, ApJS, 100, 132

Neufeld, D. A., & Wolfire, M. G. 2009, ApJ, 706, 1594

—. 2016, ApJ, 826, 183

Omukai, K., Hosokawa, T., & Yoshida, N. 2010, ApJ, 722, 1793

Ostriker, E. C., McKee, C. F., & Leroy, A. K. 2010, ApJ, 721, 975

Ostriker, E. C., & Shetty, R. 2011, ApJ, 731, 41

Padoan, P., Jones, B. J. T., & Nordlund, Å. P. 1997, ApJ, 474, 730

Papadopoulos, P. P., Thi, W.-F., & Viti, S. 2004, MNRAS, 351, 147

Papadopoulos, P. P., van der Werf, P. P., Xilouris, E. M., et al. 2012, MNRAS, 426, 2601

Parvathi, V. S., Sofia, U. J., Murthy, J., & Babu, B. R. S. 2012, ApJ, 760, 36

Pineda, J. E., Caselli, P., & Goodman, A. A. 2008, ApJ, 679, 481

Pineda, J. L., Goldsmith, P. F., Chapman, N., et al. 2010, ApJ, 721, 686

Rachford, B. L., Snow, T. P., Tumlinson, J., et al. 2002, ApJ, 577, 221

Rachford, B. L., Snow, T. P., Destree, J. D., et al. 2009, ApJS, 180, 125

Remy, Q., Grenier, I. A., Marshall, D. J., & Casandjian, J. M. 2017, A&A, 601, A78

Richings, A. J., & Schaye, J. 2016a, MNRAS, 460, 2297

—. 2016b, MNRAS, 458, 270

Richings, A. J., Schaye, J., & Oppenheimer, B. D. 2014, MNRAS, 440, 3349

Ridge, N. A., Di Francesco, J., Kirk, H., et al. 2006, AJ, 131, 2921

Ripple, F., Heyer, M. H., Gutermuth, R., Snell, R. L., & Brunt, C. M. 2013, MNRAS, 431, 1296

Röllig, M., Abel, N. P., Bell, T., et al. 2007, A&A, 467, 187

Roman-Duval, J., Jackson, J. M., Heyer, M., Rathborne, J., & Simon, R. 2010, ApJ, 723, 492

Safranek-Shrader, C., Krumholz, M. R., Kim, C.-G., et al. 2017, MNRAS, 465, 885

Saintonge, A., Kauffmann, G., Kramer, C., et al. 2011a, MNRAS, 415, 32

Saintonge, A., Kauffmann, G., Wang, J., et al. 2011b, MNRAS, 415, 61

Sandstrom, K. M., Leroy, A. K., Walter, F., et al. 2013, ApJ, 777, 5

Savage, B. D., & Sembach, K. R. 1996, ARA&A, 34, 279

Schauer, M. M., Jefferts, S. R., Barlow, S. E., & Dunn, G. H. 1989, The Journal of Chemical Physics, 91

Schlafly, E. F., Green, G., Finkbeiner, D. P., et al. 2014, ApJ, 786, 29

Schroder, K., Staemmler, V., Smith, M. D., Flower, D. R., & Jaquet, R. 1991, Journal of Physics B Atomic Molecular Physics, 24, 2487

Schruba, A., Leroy, A. K., Walter, F., et al. 2011, AJ, 142, 37

—. 2012, AJ, 143, 138

Seifried, D., Walch, S., Girichidis, P., et al. 2017, ArXiv e-prints, arXiv:1704.06487

Shapiro, P. R., & Kang, H. 1987, ApJ, 318, 32

Sheffer, Y., Rogers, M., Federman, S. R., et al. 2008, ApJ, 687, 1075

Sheffer, Y., Wolfire, M. G., Hollenbach, D. J., Kaufman, M. J., & Cordier, M. 2011, ApJ, 741, 45

Shetty, R., Glover, S. C., Dullemond, C. P., & Klessen, R. S. 2011a, MNRAS, 412, 1686

Shetty, R., Glover, S. C., Dullemond, C. P., et al. 2011b, MNRAS, 415, 3253

Silva, A. I., & Viegas, S. M. 2002, MNRAS, 329, 135

Smith, M. W. L., Eales, S. A., Gomez, H. L., et al. 2012, ApJ, 756, 40

Sofia, U. J., Lauroesch, J. T., Meyer, D. M., & Cartledge, S. I. B. 2004, ApJ, 605, 272

Sofia, U. J., Parvathi, V. S., Babu, B. R. S., & Murthy, J. 2011, AJ, 141, 22

Solomon, P. M., Rivolo, A. R., Barrett, J., & Yahil, A. 1987, ApJ, 319, 730

Sonnentrucker, P., Wolfire, M., Neufeld, D. A., et al. 2015, ApJ, 806, 49

Stacey, G. J., Hailey-Dunsheath, S., Ferkinhoff, C., et al. 2010, ApJ, 724, 957

Stancil, P. C., Schultz, D. R., Kimura, M., et al. 1999, A&AS, 140, 225

Sternberg, A., Le Petit, F., Roueff, E., & Le Bourlot, J. 2014, ApJ, 790, 10

Stoerzer, H., Stutzki, J., & Sternberg, A. 1996, A&A, 310, 592

Stone, J. M., & Gardiner, T. A. 2010, ApJS, 189, 142

Stone, J. M., Gardiner, T. A., Teuben, P., Hawley, J. F., & Simon, J. B. 2008, ApJS, 178, 137

Strong, A. W., & Mattox, J. R. 1996, A&A, 308, L21

Sutherland, R. S., & Dopita, M. A. 1993, ApJS, 88, 253

Tacconi, L. J., Neri, R., Genzel, R., et al. 2013, ApJ, 768, 74

Taylor, C. L., Kobulnicky, H. A., & Skillman, E. D. 1998, AJ, 116, 2746

Tielens, A. G. G. M., & Hollenbach, D. 1985, ApJ, 291, 722

Tomida, K., Tomisaka, K., Matsumoto, T., et al. 2013, ApJ, 763, 6

van Dishoeck, E. F., & Black, J. H. 1988, ApJ, 334, 771

Vissapragada, S., Buzard, C. F., Miller, K. A., et al. 2016, ApJ, 832, 31

Visser, R., van Dishoeck, E. F., & Black, J. H. 2009, A&A, 503, 323

Vrinceanu, D., Onofrio, R., & Sadeghpour, H. R. 2014, ApJ, 780, 2

Wakelam, V., Smith, I. W. M., Herbst, E., et al. 2010, Space Sci. Rev., 156, 13

Walch, S., Girichidis, P., Naab, T., et al. 2015, MNRAS, 454, 238

Weingartner, J. C., & Draine, B. T. 2001a, ApJ, 563, 842

—. 2001b, ApJS, 134, 263

Weselak, T., Galazutdinov, G., Beletsky, Y., & Krełowski, J. 2009, A&A, 499, 783

Weselak, T., Galazutdinov, G. A., Beletsky, Y., & Krełowski, J. 2010, MNRAS, 402, 1991

White, C. J., Stone, J. M., & Gammie, C. F. 2016, ApJS, 225, 22

Wiesenfeld, L., & Goldsmith, P. F. 2014, ApJ, 780, 183

Wolfire, M. G., Hollenbach, D., & McKee, C. F. 2010, ApJ, 716, 1191

Wolfire, M. G., Hollenbach, D., McKee, C. F., Tielens, A. G. G. M., & Bakes, E. L. O. 1995, ApJ, 443, 152

Wolfire, M. G., Hollenbach, D., & Tielens, A. G. G. M. 1993a, ApJ, 402, 195

—. 1993b, ApJ, 402, 195

Wolfire, M. G., McKee, C. F., Hollenbach, D., & Tielens, A. G. G. M. 2003, ApJ, 587, 278

Wolfire, M. G., Tielens, A. G. G. M., Hollenbach, D., & Kaufman, M. J. 2008, ApJ, 680, 384

Woodall, J., Agúndez, M., Markwick-Kemper, A. J., & Millar, T. J. 2007, A&A, 466, 1197

Yan, M. 1997, PhD thesis, HARVARD UNIVERSITY

Zanchet, A., Bussery-Honvault, B., Jorfi, M., & Honvault, P. 2009, Physical Chemistry Chemical Physics, 11, 61826191